Institut für Biophysik
Fachrichtung Physik
Fakultät für Mathematik und Naturwissenschaften
Technische Universität Dresden

TECHNISCHE UNIVERSITÄT DRESDEN

In Vitro and *In Vivo* Applications of Fluorescence Cross-Correlation Spectroscopy

Dissertation

zur Erlangung des akademischen Grades

Doctor rerum naturalium (Dr. rer. nat.)

vorgelegt von

Wolfgang Staroske

geboren in Erfurt am 28. Februar 1978

Juni 2010

First Referee:	Prof. Dr. Petra Schwille
Second Referee:	Prof. Dr. Jörg Enderlein

Abstract

Fluorescence correlation spectroscopy (FCS) analyzes the fluctuations in the fluorescence intensity, which is emitted from a tiny excition volume, to obtain information about the concentration, the mobility, and the molecular interactions of labeled molecules. The more advanced fluorescence cross-correlation spectroscopy (FCCS) increases the precision in the determination of flow velocities and binding constants compared to standard FCS.

The miniaturization in biomedical and chemical engineering has been developing rapidly, propelled by the vision of a fully functional laboratory on a single chip and its use in human therapeutics, for example, as implanted drug delivery system. A key requirement to fulfill this vision is the ability to handle small fluid volumes. Handling liquids using the electrohydrodynamical principle circumvents many of the disadvantages of other systems. The complex flow pattern in the active region of such a pump could not be resolved by common tracking techniques. In this thesis, two-focus FCCS (2f-FCCS) was used to map the flow profile inside a micropump. The high precision of 2f-FCCS in the determination of flow measurements even with small fluorescent particles allowed the measurement of the flow velocities induced by electrohydrodynamic forces acting on the solvent, while excluding the effects of dielectrophoretic forces acting on larger particles. Analysis of the flow data indicates a flow pattern that consists of two vortices of different size and opposite direction of rotation. The flow pattern derived by 2f-FCCS explains the observed complex particle trajectories in the force field and the accumulation of particles in well-defined regions above the microelectrode array.

In the second part of this thesis, the mechanism of RNA interference (RNAi) was studied by dual-color FCCS *in vivo*. RNAi is an evolutionary conserved gene silencing mechanism, which uses short double-stranded RNA molecules, called short interfering RNAs (siRNAs), as effector molecules. Due to its specificity and simplicity, RNAi yields a great potential for a widespread therapeutic use. To broaden the therapeutic applications, the *in vivo* stability of siRNAs has to be improved by chemical modifications, but some of these modifications inhibit the gene silencing mechanism. The presented FCCS assays are very well suited to investigate the individual assembly steps of RNAi machinery with very high specificity and sensitivity in real time and to study the cleavage activity of the activated RNAi machinery. A direct correlation between activity of the RNAi machinery and the results from the FCCS measurements could be shown. The influence of several chemical modifications on the assembly and activity of the RNAi machinery was investigated with these assays.

Kurzfassung

In vitro und *in vivo* Anwendungen der Fluoreszenz-Kreuzkorrelation-Spektroskopie

Fluoreszenz-Korrelations-Spektroskopie (FCS) analysiert die Fluktuationen im Fluoreszenzsignal eines kleinen angeregten Volumens, um Informationen über die Konzentration, die Bewegung und die Interaktionen der markierten Moleküle zu erhalten. Die Fluoreszenz-Kreuzkorrelations-Spektroskopie (FCCS) erhöht die Genauigkeit bei der Messung von Fließgeschwindigkeiten und Bindungskonstanten im Vergleich zur Standard-FCS.

Die Miniaturisierung der Biomedizin und Chemie hat sich rapide entwickelt, angetrieben von der Vision eines kompletten Labors auf einem Chip und dem Einsatz dieses in der medizinischen Therapie, zum Beispiel als implantierter Medikamentenspender. Ein Schlüsselelement zur Erfüllung dieser Vision ist der Transport von kleinsten Flüssigkeitsmengen in diesen miniaturisierten Systemen. Der Transport von Flüssigkeiten mittels des elektrohydrodynamischen Prinzips umgeht viele Nachteile von anderen Systemen, allerdings zeigt eine solche Pumpe ein kompliziertes Strömungsbild in der aktiven Region, welches sich mit herkömmlichen Methoden wie Teilchenverfolgung nicht vermessen ließ. Hier wurde Zwei-Fokus-FCCS (2f-FCCS) genutzt, um das Strömungsbild in der Pumpe zu vermessen. Die hohe Genauigkeit der 2f-FCCS bei der Bestimmung von Fließgeschwindigkeiten auch mit kleinen fluoreszierenden Teilchen ermöglichte die Messung der Fließgeschwindigkeiten, aufgrund der auf das Lösungsmittel wirkenden elektrohydrodynamischen Kräfte, unter Ausschluss der auf größere Teilchen wirkenden dielektrophoretischen Kräfte. Die Analyse der Daten ergab, dass das Strömungsbild aus zwei entgegengesetzt rotierenden unterschiedlich großen Wirbeln besteht. Dieses Strömungsbild erklärt die komplizierten Teilchenbewegungsbahnen und die Anreicherung der Teilchen in klar abgegrenzten Bereichen über den Mikroelektroden.

Im zweiten Teil dieser Arbeit wurde der RNAi-Mechanismus in lebenden Zellen mittels Zwei-Farben-FCCS untersucht. RNA Interferenz (RNAi) ist ein evolutionär erhaltener Geninaktivierungsmechanismus, der kurze doppelsträngige RNA Moleküle, so genannte kurze interferierende RNAs (siRNAs), als Effektormoleküle nutzt. Die Spezifität und Einfachheit der RNAi hat ihr ein weites Feld in der medikamentösen Therapie geöffnet. Zur Erweiterung dieses Feldes ist es nötig die Stabilität der siRNAs im Körper mittels chemischer Modifikationen zu erhöhen. Einige dieser Modifikationen hemmen aber den RNAi-Mechanismus. Die hier vorgestellten FCCS Experimente sind sehr gut geeignet, um die einzelnen Schritte des Zusammenbaus der RNAi Maschinerie mit hoher Empfindlichkeit und Spezifität in Echtzeit zu untersuchen und die Aktivität der RNAi Maschinerie zu studieren. Es konnte ein Zusammenhang zwischen der Aktivität der RNAi Maschinerie und den Ergebnissen der FCCS Messungen hergestellt werden. Der Einfluss von verschiedenen chemischen Modifikationen auf den Zusammenbau und die Aktivität der RNAi Maschinerie wurde mit diesen neuartigen Methoden untersucht.

List of Publications

Articles related to this thesis

Maika Felten, **Wolfgang Staroske**, Magnus S. Jaeger, Petra Schwille, and Claus Duschl. *Accumulation and filtering of nanonparticles in microchannels using electrohydrodynamically induced vortical flows.* Electrophoresis **29**(14), 2987-2996 (2008)

Thomas Ohrt*, Jörg Mütze*, **Wolfgang Staroske**, Lasse Weinmann, Julia Höck, Karin Crell, Gunter Meister, and Petra Schwille. *Fluorescence correlation spectroscopy and fluorescence cross-correlation spectroscopy reveal the cytoplasmic origination of loaded nuclear RISC* in vivo *in human cells.* Nucleic Acids Res. **36**(20), 6439-6449 (2008).

Thomas Ohrt*, **Wolfgang Staroske***, Jörg Mütze, Karin Crell, Markus Landthaler, and Petra Schwille. *Mechanistic insights into position-specific gene silencing inhibition within siRNAs caused by 2'-O-methyl modifications analyzed by fluorescence cross-correlation spectroscopy* in vivo. Nucleic Acids Research (submitted).

Other Publications

Wolfgang Staroske, Martin Pfeiffer, Karl Leo, and Michael Hoffmann. *Single-Step Triplet-Triplet Annihilation: An Intrinsic Limit for the High Brightness Efficiency of Phosphorescent Organic Light Emitting Diodes.* Phys. Rev. Lett. **98**(19), 197402 (2007).

Nicholas Luzzietti, Hergen Brutzer, Daniel Klaue, Friedrich Schwarz, **Wolfgang Staroske**, Sylvia Clausing, and Ralf Seidel. *Effective preparation of internally modified single-molecule constructs using nicking enzymes.* (in preparation).

*authors contributed equally to this work

Contents

1 Introduction and Outline

To determine mobility parameters such as diffusion coefficients and flow velocities, several techniques like nuclear magnetic resonance spectroscopy (NMR) and dynamic light scattering (DLS) have been developed. Compared to these techniques, fluorescence correlation spectroscopy (FCS) has several advantages. FCS is a single molecule sensitive technique, which analyzes the fluctuations of a fluorescence intensity trace. Additionally to the measurement of the mobility parameters, FCS measures the concentration and can be used to study molecular interactions. The use of fluorescence allows highly specific labeling of the molecules of interest, thereby simplifying the complexity of the studied system.

Since the introduction of FCS, many advancements of FCS have been developed. One of the most important one, the development of fluorescence cross-correlation spectroscopy (FCCS) analyzes the signal from two excitation volumes. The most prominent examples are two-focus FCCS (2f-FCCS) and dual-color FCCS. In 2f-FCCS, the use of two spatially separated excitation volumes increases the measurement accuracy of diffusion constants and flow velocities dramatically. In contrast, dual-color FCCS uses two spectrally separated detection volumes. This makes the measurement of molecular interactions independent from the precise determination of mobility constants. Here both cross-correlation techniques are applied to answer technical and biological questions.

The field of semiconductor electronics was the first discipline that profited from the miniaturization of its devices. Inspired from the huge advancements achieved in this discipline, miniaturization was implemented in many other engineering disciplines, and today the technological development goes hand in hand with miniaturization. In chemistry and biology one of the aims of miniaturization is the creation of a fully functional laboratory on a single chip. This includes the ability to handle small liquid volumes, which has turned out to be a complex problem. A very recent attempt uses the electrohydrodynamical principle to pump liquids through microchannels. The use of this principle avoids many of the disadvantages from other pumping techniques, but such a pump displays a complex flow pattern which was unresolveable by common techniques. Therefore, 2f-FCCS was applied to map the flow profile of such a pumping device.

The discovery that double stranded RNA (dsRNA) is able to inhibit the production of a protein encoded in the complementary gene, has revolutionized loss-of-function studies in many organisms. Short dsRNA molecules have emerged as the key regulators in these evolutionary conserved gene silencing mechanisms. In one of these mechanisms, called RNA interference (RNAi), 21 nucleotide long dsRNA

molecules, called short interfering RNAs (siRNAs), trigger the degradation of the complementary messenger RNA (mRNA). The RNAi machinery uses one of the siRNA strands to scan for mRNAs with a matching sequence. In case of perfect complementarity the mRNA is cleaved and the expression of the encoded protein inhibited. Therapeutics based on RNAi to cure genetic diseases entered already first clinical trials. Yet for widespread therapeutic use, the properties of siRNAs have to be improved, for example by the introduction of chemical modifications. These modifications can improve the lifetime of the silencing triggers, but some of these modifications display a reduced silencing activity. The mechanism behind this reduction was unknown, because standard biochemical assays measure only the silencing activity. Therefore, dual-color FCCS was employed to study inhibition of the RNAi machinery *in vivo*.

The thesis is structured in four main chapters. Chapter 2 provides the theoretical background of FCS. It outlines the physical principle of fluorescence and diffusion and presents the theory of FCS and FCCS. The application of 2f-FCCS to resolve the flow pattern of a micropump is dicussed in chapter 3. Chapter 4 gives an overview over the current knowledge of RNA-induced gene silencing mechanisms, describing the biogenesis of the effector molecules, the gene regulating mechanisms, and the influence of different chemical modifications. The mechanism of inhibition of RNAi by chemically modified siRNAs is investigated in chapter 5. Two novel *in vivo* FCCS assays are presented and their use to study the influence of various chemically modified siRNAs is depicted.

2 Fluorescence Correlation Spectroscopy

2.1 Introduction

Fluorescence correlation spectroscopy (FCS) is a single molecule technique, which uses the fluctuations in the fluorescence intensity emitted from a tiny excitation volume, to obtain information about the concentration and the mobility of the labeled molecules. The development of FCS took place in the early eighties of the last century by D. Magde, E. Elson, and W. W. Webb, who described a first application, the theory, and the experimental realization [1–3]. Although there was some progress in the field of FCS, the breakthrough did not come until single molecule sensitivity was achieved by R. Rigler and coworkers in 1993 by employing confocal detection [4]. Ever since, FCS is an exponentially growing technique (from the number of FCS related publications per year), with many advancements and applications [5–7].

One of the most important advancements was the development of dual-color fluorescence cross-correlation spectroscopy (FCCS), which offers the possibility to study the interaction of similar sized molecules. Dual-color FCCS was proposed and the theory was outlined in 1989 [8], but it was not recognized until the visionary publication of M. Eigen and R. Rigler in 1994 [9]. The first experimental realization was done by Schwille et al. in 1997 [10]. Since that time, dual-color FCCS is more and more used to study molecular interactions *in vivo*. Very recent developments extended FCCS to more than two colors, amongst others using grating and prism based separation of the fluorescent light [11–13].

Additionally to the spectral separation of light, also spatially separated light can be cross-correlated. This technique, called spatial FCCS or two-focus FCCS (2f-FCCS), was developed by Brinkmeier et al. for better resolved measurements of flow [14]. The distance between the two foci is an additional ruler, which is independent from the size and the shape of the confocal volume. Recent developments use 2f-FCCS for absolute and calibration free measurements of diffusion coefficients [15–17].

Many improvements concern the type of excitation. In 1995 excitation with infrared light was introduced to FCS, where the fluorescent molecule absorbs two photons to reach the excited state [18]. The so called two-photon excitation was studied for *in vivo* use by Schwille et al. [19] and first employed in dual-color FCCS by Heinze et al. [20]. It is applied mainly *in vivo*, because of the higher penetration depth of infrared light compared to visible light in living tissue.

Scanning FCS was introduced to overcome the problems of immobilized and

slowly diffusing molecules, especially the bleaching of the fluorophore [21]. With the recent combinations of laser scanning microscopes and FCS, in principle every kind of scanning pattern is possible, but mostly lines [22–24] and circles [25–28] are used.

Several techniques to reduce the size of the confocal volume in FCS are known. The oldest and mostly used one is the combination of FCS with an excitation by total internal reflection [29, 30]. The strong exponential decay of the evanescent field lead to a strong reduction of the confocal volume in the axial direction. The combination was first introduced by N. L. Thompson and coworkers [31, 32]. In earlier times the evanescent field was created by reflecting a laser inside a prism, which was placed on the objective opposing side of the sample [33–35]. In 2005 the technique to create the evanescent field by reflecting the laser in the objective [36] was applied by Hassler et al. to FCS [37, 38] and extended to dual-color FCCS with objective based total internal reflection excitation [39].

For a long time the electronic signals of the detectors were directly fed into hardware correlators. With the development of pulsed lasers and better data registration electronics, the technique of time-correlated single photon counting (TCSPC) was introduced and used together with FCS [40–44]. Thereby the arrival time of the fluorescence photon relative to the lab time and to the excitation pulse is saved and evaluated. With increasing time resolution of detectors and electronics into the nanosecond range, the effect of fluorescence lifetime can be seen as anti-bunching in so called full-correlation functions [45, 46]. The fluorescence lifetime can also be used to discriminate between different fluorescent dyes [47].

Techniques, which are similar to FCS and use the same data, are photon counting histogram (PCH) [48, 49] and fluorescence intensity distribution analysis (FIDA) [50–53]. Both techniques analyze the brightness of the fluorescent molecules.

Another technique, which is similar to FCS, is image correlation spectroscopy (ICS) [54–56]. ICS uses correlation techniques to analyze spatial information from laser scanning microscope images. Recently, ICS was extended to the time domain, as spatial-temporal ICS [57, 58] and as raster image correlation spectroscopy (RICS) [59].

2.2 Physical Basics

2.2.1 Fluorescence

Principles of Fluorescence

The relaxation of a molecule from the first excited singlet state under the emission of a photon is called fluorescence. The main path of excitation is the absorption of light, but molecules can also be excited by thermal or chemical energy. If the

excited state is a triplet state and the molecule relaxes to the ground state under emission of a photon, the process is called phosphorescence.

Typically in organic molecules the electronic states which participate in the absorption and emission of visible light are formed by a conjugated π-electron system. A simple example of a conjugated π-electron system, benzene, can be seen in Fig. 2.1. The atomic orbitals of carbon hybridize into the sp_2 and p_z orbitals in benzene. While the sp_2 orbitals form σ bonds, the p_z orbitals form the conjugated π-electron system. Due to the four valence electrons of carbon all binding states of the molecule are filled, and all anti-binding states are empty. The weakness of the π-bonds compared to the σ-bonds leads to a smaller energy difference between the π-binding and π^*-anti-binding states compared to the energy difference of the σ states. The energy difference between the π-states lies in the ultraviolet and visible range of light.

Under the assumption that the Born-Oppenheimer separation conditions are fulfilled, the molecular wave function can be written as a product of the electronic, vibrational, and rotational wave functions. Then the energy of a molecular state is the sum of the occupied electronic, vibrational, and rotational states. Transitions between electronic states have typically wavelengths in the ultraviolet and visible part of the optical spectrum. The wavelengths of photons from vibrational state transitions are in the near infrared, and those from rotational state transitions are in the far infrared. In optical spectra at room temperature, transitions between rotational states cause typically only a broadening of the spectral lines.

For fluorophores other than organic molecules the energy difference between the first excited state and the ground state is defined by other intrinsic properties of these fluorophores, but the rest of the discussion above applies as well.

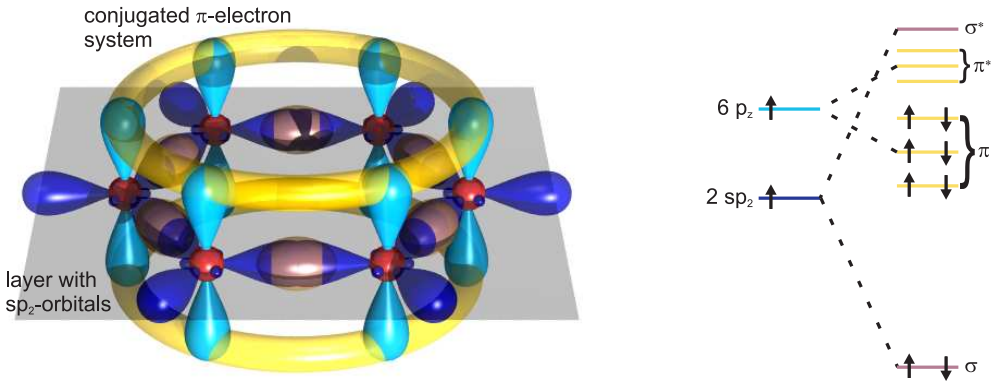

Figure 2.1: Bonds and electronic states of benzene. Chemical bonds inside benzene, with the conjugated π-electron system (left). Electronic states in benzene with the binding π and σ states and the anti-binding π^* and σ^* states (right) [60].

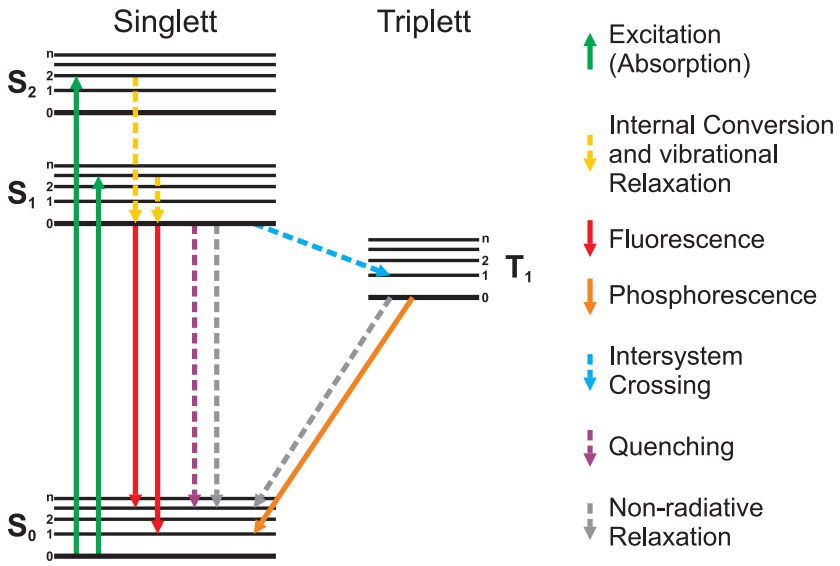

Figure 2.2: Jablonski diagramm: Under Absorption of light, the fluorophore is excited in 10^{-15} s to the first or higher excited state. There it returns to the vibrational ground state of the first excited state S_1 in 10^{-13} s by vibrational relaxation and internal conversion. From here it goes back to the ground state under emission of a photon (fluorescene) in 10^{-8} s or without a photon by quenching or non-radiative decay. From the first excited state the fluorophore can also jump into the triplet state by intersystem crossing (ISC). From there it relaxes to the ground state by phosphorescence in more than 10^{-4} s or by non-radiative decay. Adapted from [61].

The processes which are involved in fluorescence and phosphorescence are often depicted in a Jablonski-diagram (Fig. 2.2). The fluorophore is exited by the absorption of one or more photons in 10^{-15} s. After fast electronic transitions, like emission and absorption, the atomic nuclei are not in the equilibrium position, due to the much slower relaxation (10^{-13} s) of the nuclear distances. Therefore, electronic transitions often end up in higher vibrational states (Franck-Condon-principle). By vibrational relaxation and internal conversion the fluorophore relaxes into the vibrational ground state of the first excited state S_1 in around 10^{-13} s. From there the fluorophore returns to the ground state under emission of a photon (fluorescence) in 10^{-8} s. This time is called the fluorescence lifetime. The fluorophore can also return to the ground state via quenching or non-radiative decay. From the first excited state a quantum-mechanically forbidden transition, called intersystem crossing (ISC), into the first triplet state can occur with a much lower probability than fluorescence. From the triplet state the fluorophore returns into the ground state under emission of a photon (phosphorescence) in more than 10^{-4} s or via non-radiative decay and quenching.

A fluorophore is characterized by several physical properties. First, there are the absorption and emission spectra, which characterize the typical wavelength of the fluorescent processes. The difference between emission and absorption wavelength, due to the Franck-Condon-Principle, is called Stokes-Shift and allows the separation of the fluorescent light from the excitation light by dichroic mirrors. The second characteristic is the molecular brightness, which is defined by the extinction coefficient σ_{ex} and the quantum yield φ. The extinction coefficient σ_{ex} describes the cross-section of the interaction between the fluorophore and the excitation light. It is a measure for the probability of the fluorophore to become excited. The quantum yield φ is the probability that an excited fluorophore returns to the ground state under emission of a photon and can be calculated from the rates k of the different processes shown in Fig. 2.2

$$\varphi = \frac{k_{\text{Fluor.}}}{k_{\text{Fluor.}} + k_{\text{ISC}} + k_{\text{non-rad. Relax.}} + k_{\text{Quenching}}(Q)} = \frac{\text{emitted photons}}{\text{absorbed photons}}. \quad (2.1)$$

The third characteristic is the bleaching probability. It defines the amount of photons a fluorophore can emit before its fluorescent activity is destroyed by a photochemical reaction.

Fluorescent Markers

Although many cells show some autofluorescence in the green part of the visible spectra, many interesting biological molecules and proteins are non-fluorescent. To study these molecules they have to be labeled with a fluorophore. The labeling is performed either chemically, by organic dyes and quantum dots, or genetically with fluorescent proteins. For all labeling techniques the functionality of the labeled molecule or protein has to be verified afterwards, because the fluorescent label can hinder the molecule/protein in its correct function. The three most used groups of fluorophores are shown in Fig. 2.3.

Small organic dyes (Fig. 2.3(a)) are typically improved derivatives of fluorescein, rhodamines, and cyanines, like the Alexa and Atto dye families (Invitrogen, ATTO-Tec). These families cover a wide range of wavelengths and are functionalized by a reactive group for labeling. Due to their small molecular mass of less than 1 kDa they induce a lower steric hindering compared to fluorescent proteins.

Autofluorescent proteins are widely used for cellular studies. Interesting proteins can be easily labeled by cloning the genetic information of the fluorescent protein to the genetic information of the protein of interest. Then the cells express a fusion protein, consisting of the fluorescent protein and the protein of interest. The best studied and mostly used fluorescent protein is the green fluorescent protein (GFP) (Fig. 2.3(b)). From its discovery in the jellyfish *Aequorea victoria* in 1962 [65], it took more than 30 years until its genetic sequence and crystal structure was resolved [66–69]. GFP has a barrel like structure formed from

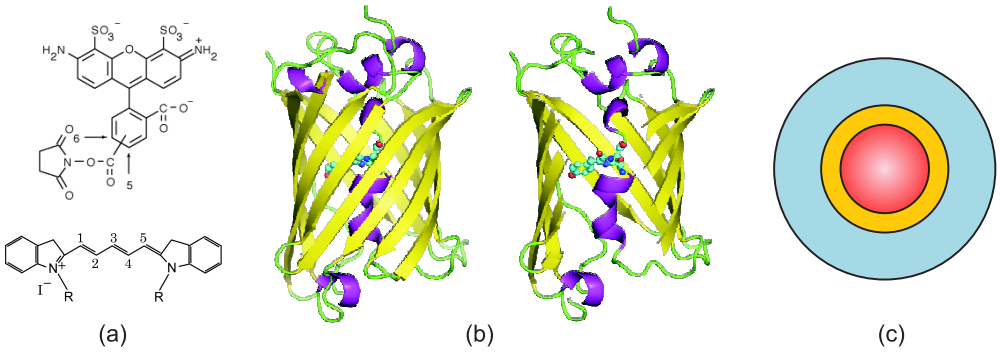

Figure 2.3: Different types of Fluorophores: (a) Two common examples for small organic fluorophores: Alexa488 (top) [62] emits green light, and Cy5 (bottom) [63] emits far red light. (b) Crystal structure of the most prevalent fluorescent protein GFP. (On the right side opened, to show the fluorophore.) [64]. (c) Schematic drawing of a quantum dot, consisting of core, shell, and coating (from the inner to the outer). Pictures are not drawn to scale.

β-sheets, with an inside positioned fluorophore. The fluorophore forms automatically after translation from three amino acids. Many mutants of GFP were created and used [70]. The first red fluorescent protein DsRed was extracted [71] from a coral, but due to its strong tendency to form oligomers [72] it was not widely used until its monomeric form mRFP was found [73]. Also from DsRed/mRFP many mutants were created with shifted absorption and emission wavelengths, like mOrange and mCherry [74]. The properties of these fluorescent proteins, especially for fluorescent imaging, were reviewed in [75]. A brighter red fluorescent protein was generated from a red protein of a sea anemone and called TagRFP [76]. These proteins are still under development, so more photostable versions of these proteins called mOrange2 and TagRFP-T were developed recently [77]. Proteins with special features like a strong Stokes-shift or the possibility of photo-switching, called mKeima [78], Kaede [79, 80] and Dronpa [81, 82], are also available. Many of these fluorescent proteins exhibit strong photo-physical behavior, like blinking on the microsecond scale [83–88]. For this reason the usability of these proteins for the given application in FCS has to be checked carefully.

The third group of fluorophores are anorganic semiconductor nanocrystals, called quantum dots (Fig. 2.3(c)) [89–91]. They typically consist of a semiconductor core with a size of 2 nm to 10 nm, a shell, and a coating, which provides the bio-compatibility, like water-solubility, of these anorganic crystals. The complete diameter is in the range of 20 nm. Quantum dots have broad absorption spectra, a narrow, nearly symmetrical emission spectra and a superior photo-stability. The emission wavelength is easily tuneable, by the size of the core, and due to the narrow emission spectra and their superior photo-stability, they are well suited

for multi-color applications. Quantum dots would be perfect fluorescent labels for multicolor FCCS, if they would not have a complicated photophysics, with blinking times following a power law distribution [92, 93]. In a recent publication a fit model consisting of 1 bright and 5 dark states, following the power law, was developed, which seems to be able to describe the blinking of quantum dots in FCS even at higher excitation powers [94]. Another model using subdiffusion was presented in [95], based on comparisons of FCS, ICS and simulations. Next to the studies which use FCS to investigate the blinking behavior of quantum dots, there exist only a small number of publications dealing with FCS and quantum dots [96–98]. They are reviewed in [99], and a comparison of the photophysical properties of quantum dots and some organic dyes can be found in [100].

2.2.2 Diffusion

The movement of tracer particles due to elastic interactions with solvent molecules is called Brownian motion. Although it was described before, even in the Antique by Lucretius in his book "Of the Nature of Things" [101] and by other scientists, Robert Brown is traditionally regarded as the discoverer of this motion [102]. The tracer particles moves due to collisions with solvent molecules, which diffuse around. Free diffusion is described by the diffusion equation also known as Fick's second law

$$\frac{\partial C(\vec{r},t))}{\partial t} = D\nabla^2 C(\vec{r},t) \tag{2.2}$$

with $C(\overrightarrow{r},t))$ as concentration. The diffusion coefficient D can be calculated from the Einstein-Stokes-equation

$$D = \frac{k_B T}{6\pi\eta_m R_0}, \tag{2.3}$$

with k_B as Boltzmann constant and T as temperature. η_m is the viscosity of the medium and R_0 the hydrodynamic radius of the diffusing particle. The diffusion coefficient depends directly and indirectly via the viscosity η_m on the temperature. Equation (2.3) assumes a homogenous, interaction-free and isotropic environment.

2.3 Theory of Fluorescence Correlation Spectroscopy

2.3.1 Principle of Autocorrelation

In a confocal FCS setup (Fig. 2.4(a)) a laser beam is focussed to a diffraction limited spot by the objective. The emitted fluorescence from molecules diffusing through this spot is collected by the same objective. The fluorescent light is spectrally separated from the excitation light by dichroic mirrors and emission filters and focussed through a pinhole. The pinhole confines the detection volume predominantly in axial direction. An avalanche photodiode (APD) detects the

fluorescence signal F (Fig. 2.4(c)). This fluorescence intensity can be written as the sum of the average fluorescence $\langle F \rangle$ and their fluctuations δF

$$F(t) = \langle F \rangle + \delta F(t) \quad \text{with} \quad \langle F \rangle = \frac{1}{t_{\text{meas}}} \int_0^{t_{\text{meas}}} F(t)\, dt \tag{2.4}$$

and the autocorrelation of the fluorescence signal is defined by

$$G(\tau) = \frac{\langle \delta F(t)\, \delta F(t+\tau) \rangle}{\langle F(t) \rangle \langle F(t) \rangle} = \frac{\langle F(t)\, F(t+\tau) \rangle}{\langle F(t) \rangle \langle F(t) \rangle} - 1\,. \tag{2.5}$$

The fluorescent signal is compared with itself for different lag times τ by calculating the autocorrelation function, and thereby the self similarity of the signal is tested. For small lag times the fluorophore is still in the confocal volume, emitting photons, so the similarity is high. For large lag times the fluorophore has left the volume, so the correlation curve decays to zero, because there is no similarity in the signal anymore. The average residence time of the fluorophore in the confocal volume is found at the half maximum of the correlation curve, and this time is related to the diffusion coefficient D of the fluorescent molecule (Fig. 2.4(d)).

The detected fluorescence signal F from n different fluorescent molecules can be described as follows

$$F(t) = \sum_{i=1}^{n} \kappa_i\, \sigma_{\text{ex},i}\, \varphi_i \int_V I_{\text{ex}}(\vec{r})\, S(\vec{r})\, C_i(\vec{r}, t)\, d^3\vec{r} \tag{2.6}$$

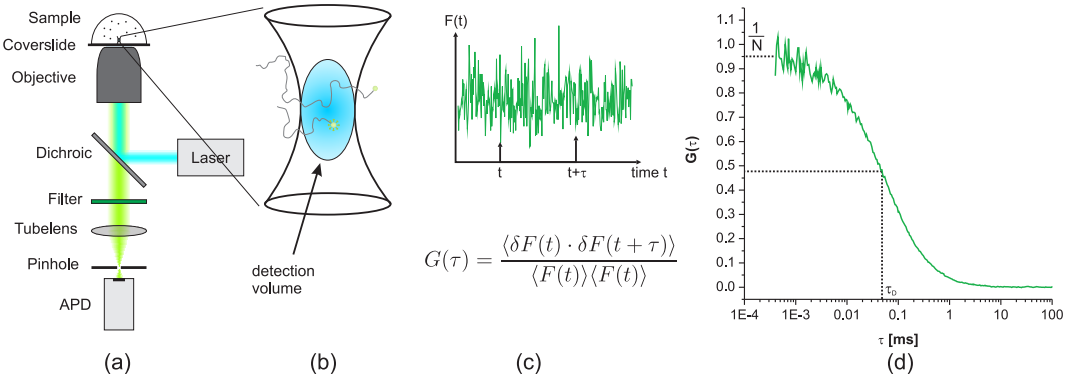

Figure 2.4: Principle of FCS: (a) A confocal volume is created by focusing a laser through the objective. The emitted fluorescence is collected with the same objective, spectrally and spatially filtered by a bandpass filter and a pinhole, respectively, and detected by an APD. (b) Molecules diffuse through the confocal volume and give rise to a fluctuating intensity trace (c). The autocorrelation curve (d), which is a measure for the self similarity of the signal is calculated from the intensity trace. By fitting appropriate models to the curve, physical parameters can be extracted.

with κ the detector efficiency, σ_{ex} and φ as the fluorophore properties extinction coefficient and quantum yield, respectively. The excitation intensity profile $I_{\text{ex}}(\vec{r})$ and the normalized collection efficiency function $S(\vec{r})$ characterize the confocal volume, and $C(\vec{r},t)$ is the concentration of the fluorescent molecules. With the following definitions of the molecular brightness η and molecule detection function $W(\vec{r})$

$$\eta_i = \kappa_i \, \sigma_{\text{ex},i} \, \varphi_i \, I_0 \tag{2.7}$$

$$W(\vec{r}) = \frac{I_{\text{ex}}(\vec{r})}{I_0} \, S(\vec{r}) \tag{2.8}$$

the fluorescence signal can be written as

$$F(t) = \sum_{i=1}^{n} \int_V W(\vec{r}) \, \eta_i \, C_i(\vec{r},t) \, d^3\vec{r} \tag{2.9}$$

and the fluorescence fluctuations as

$$\delta F(t) = \sum_{i=1}^{n} \int_V W(\vec{r}) \, \delta(\eta_i \, C_i(\vec{r},t)) \; d^3\vec{r}. \tag{2.10}$$

For the case of τ=0 and only one species (n=1) in eq. (2.5) and with proportionality of the fluorescence signal to the concentration and thereby to the mean particle number $\langle N \rangle$ (see eq. (2.6) and (2.9)), we find

$$G(0) = \frac{\langle \delta F^2 \rangle}{\langle F \rangle^2} = \frac{\langle \delta N^2 \rangle}{\langle N \rangle^2} = \frac{1}{\langle N \rangle} \, , \tag{2.11}$$

because $\langle \delta N^2 \rangle = \text{Var}(N) = \langle N \rangle$, due to the Poisson distributed number of molecules in the detection volume (Fig. 2.4(b)). In reality fluorophores show photophysical effects, which change the molecular brightness η and thereby lead to fluctuations in the fluorescence intensity, which result in distortions of the correlation curve.

The experimental molecular brightness η_{exp} is usually calculated from the measured and averaged fluorescence intensity $\langle F \rangle$ and the mean particle number $\langle N \rangle$ and corresponds to η defined in eq. (2.7) in the following way (the definition of the effective volume V_{eff} can be found in eq. (2.20))

$$\eta_{\text{exp}} = \frac{\langle F \rangle}{\langle N \rangle} = \eta \, \frac{\int W(\vec{r}) \, d^3\vec{r}}{V_{\text{eff}}} = \eta \, \frac{V}{V_{\text{eff}}} \, . \tag{2.12}$$

2.3.2 Derivation of the Model-Function for Autocorrelation

To extract physical parameters like concentrations and diffraction coefficients from correlation curves a model function has to be derived. A more general and more detailed derivation of the correlation function can be found in [103]. Starting with eq. (2.5) and inserting eq. (2.10) we get

$$G(\tau) = \frac{\sum_{i=1}^{n}\sum_{j=1}^{n}\int_{V'}\int_{V} W(\vec{r})\,W(\vec{r}')\langle\delta(\eta_i\,C_i(\vec{r},t))\;\delta(\eta_j\,C_j(\vec{r}',t+\tau))\rangle\;d^3\vec{r}\,d^3\vec{r}'}{\left(\sum_{i=1}^{n}\int_{V} W(\vec{r})\,\langle\eta_i\,C_i(\vec{r},t)\rangle\;d^3\vec{r}\right)^2} \tag{2.13}$$

and for the simpler case n=1

$$G(\tau) = \frac{\int_{V'}\int_{V} W(\vec{r})\,W(\vec{r}')\langle\delta(\eta\,C(\vec{r},t))\;\delta(\eta\,C(\vec{r}',t+\tau))\rangle\;d^3\vec{r}\,d^3\vec{r}'}{\left(\int_{V} W(\vec{r})\,\langle\eta\,C(\vec{r},t)\rangle\;d^3\vec{r}\right)^2}\,. \tag{2.14}$$

The fluctuation term can be separated

$$\delta(\eta_i\,C_i(\vec{r},t)) = C_i(\vec{r},t)\,\delta\eta_i + \eta_i\,\delta C_i(\vec{r},t)\,. \tag{2.15}$$

Under the assumption that the molecular brightness η is constant ($\delta\eta_i$=0) and with the following definition of the concentration correlation function

$$\Phi_{i,j}(\vec{r},\vec{r}',\tau) = \langle\delta C_i(\vec{r},t)\,\delta C_j(\vec{r}',t+\tau)\rangle\,, \tag{2.16}$$

eq. (2.13) can be simplified to

$$G(\tau) = \frac{\sum_{i=1}^{n}\sum_{j=1}^{n}\int_{V'}\int_{V} W(\vec{r})\,W(\vec{r}')\,\eta_i\,\eta_j\,\Phi_{i,j}(\vec{r},\vec{r}',\tau)\;d^3\vec{r}\,d^3\vec{r}'}{\left(\sum_{i=1}^{n}\int_{V} W(\vec{r})\,\langle\eta_i\,C_i(\vec{r},t)\rangle\;d^3\vec{r}\right)^2} \tag{2.17}$$

and for the case n=1 to

$$G(\tau) = \frac{\int_{V'}\int_{V} W(\vec{r})\,W(\vec{r}')\,\Phi(\vec{r},\vec{r}',\tau)\;d^3\vec{r}\,d^3\vec{r}'}{\left(\int_{V} W(\vec{r})\,\langle C(\vec{r},t)\rangle\;d^3\vec{r}\right)^2}\,. \tag{2.18}$$

The molecule detection function $W(\vec{r})$ describes the detection volume and is influenced by the focused laser beam and the pinhole. For the creation of a confocal volume a collimated laser beam with a radial gaussian intensity distribution is focused with a high numerical aperture (NA) objective. If the back aperture is underfilled, the lateral intensity distribution can be described by a gaussian. In most cases the back aperture is overfilled, to achieve smaller detection volumes. This leads to diffraction rings in the lateral excitation profile. In the axial direction the detection volume is confined by a pinhole in the image plane. The best assumptions for real confocal volumes are Gauss-Lorentz models (examples can

be found in [16, 18, 104]), but none of these models lead to a analytical expression of the model function. Therefore, the detection volume is approximated by a 3D-Gauss model [4]

$$W(\vec{r}) = \exp\left(-\frac{2(x^2+y^2)}{\omega_0^2} - \frac{2z^2}{z_0^2}\right). \tag{2.19}$$

ω_0 is the lateral radius of the detection volume, where the intensity of the laser beam is fallen to $1/e^2$. Two times z_0 is the axial length of the detection volume and is often substituted by the structure parameter S (eq. (2.26)). To simplify the model functions we define the effective volume V_{eff}

$$V_{\text{eff}} = \frac{\left(\int_V W(\vec{r})\, d^3\vec{r}\right)^2}{\int_V (W(\vec{r}))^2\, d^3\vec{r}} = \pi^{\frac{3}{2}}\, \omega_0^2\, z_0\,. \tag{2.20}$$

To determine the concentration correlation function $\Phi(\vec{r}, \vec{r}', \tau)$, the diffusion-transport-reaction-equation [103]

$$\frac{\partial \delta C_i(\vec{r},t)}{\partial t} = D_i\, \nabla^2\, \delta C_i(\vec{r},t) + \sum_{j=1}^{n} T_{ij}\, \delta C_i(\vec{r},t) - \vec{v}(\vec{r},t)\, \nabla \delta C_i(\vec{r},t)\,, \tag{2.21}$$

with D_i the diffusion coefficient of the molecular species i, T_{ij} as the elements of the reaction matrix T and $\vec{v}(\vec{r},t)$ the flow velocity (the relative velocity between the fluorescent particle and the detection volume), has to be solved.

Translational Diffusion

For the case of translational diffusion ($\vec{v}(\vec{r},t)$=0) with one species (n=1) (eq. (2.21)) the concentration correlation function (2.16) can be calculated [2, 103] to

$$\Phi(\vec{r}, \vec{r}', \tau) = \frac{\langle C(\vec{r},t)\rangle}{(4\,\pi\, D\, \tau)^{\frac{3}{2}}}\ \exp\left(-\frac{(\vec{r}-\vec{r}')^2}{4\, D\, \tau}\right). \tag{2.22}$$

Using this in eq. (2.18) gives the model function for the autocorrelation curve in the case of translational diffusion with one species to

$$G(\tau) = \frac{1}{\langle C(\vec{r},t)\rangle\, V_{\text{eff}}}\ \frac{1}{1+\frac{4\,D\,\tau}{\omega_0^2}}\ \frac{1}{\sqrt{1+\frac{4\,D\,\tau}{z_0^2}}}\,. \tag{2.23}$$

With the following equation for the mean particle number $\langle N\rangle$ and the definitions of the diffusion time τ_{D} and the structure parameter S

$$\langle N\rangle = \langle C(\vec{r},t)\rangle\, V_{\text{eff}} \tag{2.24}$$

$$\tau_{\text{D}} = \frac{\omega_0^2}{4\, D} \tag{2.25}$$

$$S = \frac{z_0}{\omega_0} \tag{2.26}$$

the model function can be further simplified to

$$G(\tau) = \frac{1}{\langle N \rangle} \frac{1}{1+\frac{\tau}{\tau_\mathrm{D}}} \frac{1}{\sqrt{1+\frac{\tau}{S^2\,\tau_\mathrm{D}}}}\,. \tag{2.27}$$

In case of translational diffusion for multiple species (n>1) the concentration correlation function contains only diagonal elements [103]

$$\begin{aligned} \Phi_{i,j}(\vec{r},\vec{r}',\tau) &= \frac{\langle C_i(\vec{r},t)\rangle}{(4\,\pi\,D_i\,\tau)^{\frac{3}{2}}} \exp\left(-\frac{(\vec{r}-\vec{r}')^2}{4\,D_i\,\tau}\right) && \text{for} \quad i=j \\ \Phi_{i,j}(\vec{r},\vec{r}',\tau) &= 0 && \text{for} \quad i\neq j\,. \end{aligned} \tag{2.28}$$

The autocorrelation function is then written as the weighted sum of the correlation functions of the different species

$$G(\tau) = \sum_{i=1}^{n} \Lambda_i^2\, G_i(D_i,\tau) \tag{2.29}$$

with the brightness weighting factor

$$\Lambda_i = \frac{\eta_i\,\langle C_i\rangle}{\sum_{j=1}^{n}(\eta_j\,\langle C_j\rangle)} \tag{2.30}$$

and the single species correlation function

$$G_i(D_i,\tau) = \frac{1}{\langle C_i(\vec{r},t)\rangle\,V_\mathrm{eff}} \frac{1}{1+\frac{4\,D_i\,\tau}{\omega_0^2}} \frac{1}{\sqrt{1+\frac{4\,D_i\,\tau}{z_0^2}}}\,. \tag{2.31}$$

Because of the unknown molecular brightness of the single species η_i the squared brightness weighting factor Λ_i^2 is written as a fraction f_i. This, together with the definitions in eq. (2.24), (2.25), and (2.26), simplifies the autocorrelation function to

$$G(\tau) = \frac{1}{\langle N\rangle} \sum_{i=1}^{n} \left(f_i \frac{1}{1+\frac{\tau}{\tau_{D,i}}} \frac{1}{\sqrt{1+\frac{\tau}{S^2\,\tau_{D,i}}}} \right) \quad \text{with} \quad \sum_{i=1}^{n} f_i = 1\,. \tag{2.32}$$

Translational Diffusion and Active Transport

Additionally to the translational diffusion a relative velocity between the fluorescent particles and the observation volume can be found. The reason for this directed motion is either the active transport of the fluorescent particles, for example due to active transport in cells or due to a flow in capillary, or the motion of the observation volume on the sample, for example due to scanning.

Again the concentration correlation function is calculated from the diffusion-transport-reaction-equation (2.21) for the case of one fluorescent species (n=1) [7, 14] to

$$\Phi(\vec{r},\vec{r}\,',\tau) = \frac{\langle C(\vec{r},t)\rangle}{(4\,\pi\,D\,\tau)^{\frac{3}{2}}}\;\exp\!\left(-\frac{(\vec{r}-\vec{r}\,'+\vec{v}\,\tau)^2}{4\,D\,\tau}\right). \tag{2.33}$$

Inserting this in eq. (2.18) and after the integrations, the model function for the autocorrelation curve in the case of translational diffusion and active transport with one species follows as

$$G(\tau) = \frac{1}{\langle C(\vec{r},t)\rangle\,V_{\text{eff}}}\;\frac{\exp\!\left(\frac{-(v_x^2+v_y^2)\,\tau^2}{\omega_0^2+4\,D\,\tau}\right)}{1+\frac{4\,D\,\tau}{\omega_0^2}}\;\frac{\exp\!\left(\frac{-v_z^2\,\tau^2}{z_0^2+4\,D\,\tau}\right)}{\sqrt{1+\frac{4\,D\,\tau}{z_0^2}}}. \tag{2.34}$$

Using the definitions in (2.24) and (2.26) and for the usual case that the flow is only perpendicular to the optical axis (v_z=0), the model function can be further simplified to

$$G(\tau) = \frac{1}{\langle N\rangle}\;\frac{1}{1+\frac{4\,D\,\tau}{\omega_0^2}}\;\frac{1}{\sqrt{1+\frac{4\,D\,\tau}{S^2\,\omega_0^2}}}\;\exp\!\left(\frac{-v^2\,\tau^2}{\omega_0^2\;+\;4\,D\,\tau}\right), \tag{2.35}$$

with

$$v = |\vec{v}| = \sqrt{v_x^2+v_y^2} \tag{2.36}$$

the absolute value of the velocity. Note that the autocorrelation function depends only on the magnitude of the flow velocity $\vec{v}(\vec{r},t)$ and not on the direction.

Triplet and Blinking

In the diffusion-transport-reaction-equation (2.21) the general case of reactions is described, but for many cases the problem gets quickly too complicated. A simple and solvable case is the change of a fluorophore from the bright to the dark state and back, without changing the diffusion coefficient of the fluorophore.

$$B \underset{k_{-1}}{\overset{k_1}{\rightleftharpoons}} D$$

The concentration correlation function can be calculated [103] from eq. (2.21)

to

$$\begin{aligned}
\Phi_{BB}(\vec{r},\vec{r}',\tau) &= \frac{\langle C_B(\vec{r},t)\rangle}{(4\,\pi\,D\,\tau)^{\frac{3}{2}}}\;\frac{k_{-1}+k_1\,e^{-(k_1+k_{-1})\,\tau}}{k_1+k_{-1}}\;\exp\!\left(-\frac{(\vec{r}-\vec{r}')^2}{4\,D\,\tau}\right)\\
\Phi_{DD}(\vec{r},\vec{r}',\tau) &= \frac{\langle C_D(\vec{r},t)\rangle}{(4\,\pi\,D\,\tau)^{\frac{3}{2}}}\;\frac{k_1+k_{-1}\,e^{-(k_1+k_{-1})\,\tau}}{k_1+k_{-1}}\;\exp\!\left(-\frac{(\vec{r}-\vec{r}')^2}{4\,D\,\tau}\right)\\
\Phi_{BD}(\vec{r},\vec{r}',\tau) &= \frac{\langle C_B(\vec{r},t)\rangle}{(4\,\pi\,D\,\tau)^{\frac{3}{2}}}\;\frac{k_1+k_1\,e^{-(k_1+k_{-1})\,\tau}}{k_1+k_{-1}}\;\exp\!\left(-\frac{(\vec{r}-\vec{r}')^2}{4\,D\,\tau}\right)\\
\Phi_{DB}(\vec{r},\vec{r}',\tau) &= \Phi_{BD}(\vec{r},\vec{r}',\tau)
\end{aligned} \tag{2.37}$$

Inserting these concentration correlation functions into eq. (2.17) gives the following autocorrelation function

$$\begin{aligned}
G(\tau) = \frac{1}{(\langle C_B(\vec{r},t)\rangle + \langle C_D(\vec{r},t)\rangle)\,V_{\text{eff}}}\;\frac{1}{1+\frac{\tau}{\tau_{\text{D}}}}\;\frac{1}{\sqrt{1+\frac{\tau}{S^2\,\tau_{\text{D}}}}}\\
\cdot\left(1+K\,\left(\Lambda_B-\frac{1}{K}\,\Lambda_D\right)^2\,e^{-\frac{\tau}{\tau_b}}\right)
\end{aligned} \tag{2.38}$$

with the definitions of the equilibrium constants K and the relaxation time τ_b

$$K = \frac{k_1}{k_{-1}} = \frac{\langle C_D\rangle}{\langle C_B\rangle} \tag{2.39}$$

$$\tau_b = \frac{1}{k_{-1}+k_1} \tag{2.40}$$

and the brightness weighting factor Λ_i (2.30).

For the case that the molecular brightness of the dark state is zero (η_D=0) the autocorrelation function can be written in the usual form for triplet blinking with $\tau_b = \tau_{\text{T}}$

$$G(\tau) = \frac{1}{\langle N\rangle}\,\left(1+\frac{f_{\text{T}}}{1-f_{\text{T}}}\,\exp\left(-\frac{\tau}{\tau_{\text{T}}}\right)\right)\,\frac{1}{1+\frac{\tau}{\tau_{\text{D}}}}\,\frac{1}{\sqrt{1+\frac{\tau}{S^2\,\tau_{\text{D}}}}}\,, \tag{2.41}$$

with the triplet fraction $f_{\text{T}} = K/(K+1) = \langle C_D\rangle/(\langle C_B\rangle + \langle C_D\rangle)$.

Eq. (2.41) is only correct for the case that the rate constants k_1 and k_{-1} are constant. In reality this is not fulfilled, because k_1 is intensity dependent, and therefore the probability to enter the dark-state is different at different places of the confocal volume. The eq. (2.41) is still used as a good approximation. A more detailed study can be found in [105] and another approach in [106].

2.4 Two-Focus Fluorescence Cross-Correlation Spectroscopy

In two-focus fluorescence cross-correlation spectroscopy (2f-FCCS), two separated foci are created by focusing two laser into the sample(Fig. 2.5(a)). The laser beams enter the objective under a slight angular difference. The fluorescence signal F from both foci is auto- and cross-correlated. Only molecules which visited both detection volumes, either due to active transport/flow or diffusion, contribute to the cross-correlation curve (Fig. 2.5(c)). The distance R between the two foci is an external ruler, which allows absolute measurements of diffusion constants [16] and introduces direction sensitivity in flow measurements [14]. With the two fluorescent intensities $F_1(t)$ and $F_2(t)$ the auto- and cross-correlation curves are defined by

$$G_{\mathrm{AC},1}(\tau) = \frac{\langle \delta F_1(t) \cdot \delta F_1(t+\tau) \rangle}{\langle F_1(t) \rangle \langle F_1(t) \rangle} \tag{2.42}$$

$$G_{\mathrm{AC},2}(\tau) = \frac{\langle \delta F_2(t) \cdot \delta F_2(t+\tau) \rangle}{\langle F_2(t) \rangle \langle F_2(t) \rangle} \tag{2.43}$$

$$G_{\mathrm{CC},1}(\tau) = \frac{\langle \delta F_1(t) \cdot \delta F_2(t+\tau) \rangle}{\langle F_1(t) \rangle \langle F_2(t) \rangle} \tag{2.44}$$

$$G_{\mathrm{CC},2}(\tau) = \frac{\langle \delta F_2(t) \cdot \delta F_1(t+\tau) \rangle}{\langle F_1(t) \rangle \langle F_2(t) \rangle} \,. \tag{2.45}$$

The model functions to fit the autocorrelation curves are the same as for trans-

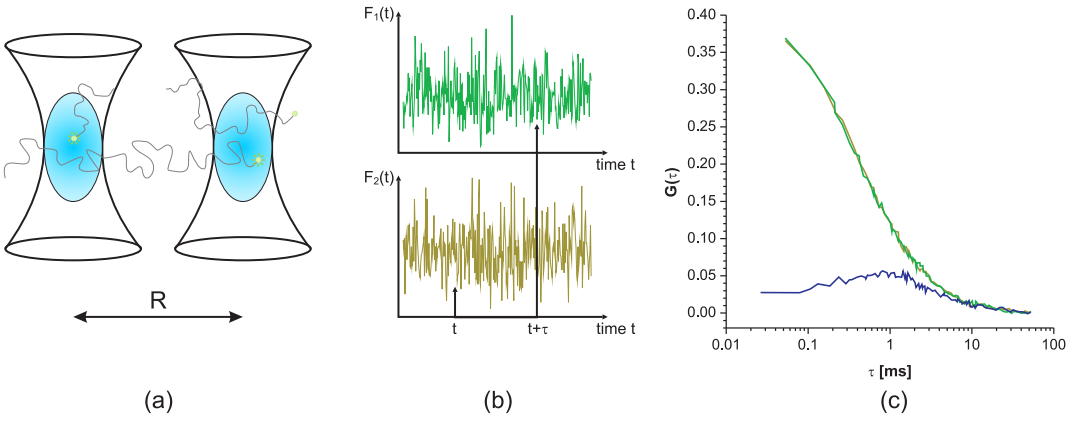

Figure 2.5: Principle of two-focus FCCS: (a) Two foci are created by objective focussed laser beams with a distance R. (b) Molecules diffuse through the confocal volumes and give rise to two fluctuating intensity traces. (c) Auto- (green, darkgreen), and cross-correlation (blue) curves calculated from the intensity traces [107].

lational diffusion and active transport in section 2.3.2. The derivation of the cross-correlation model function follows in principle the same way as for the autocorrelation, but we have to consider two different molecule detection functions $W_1(\vec{r})$ and $W_2(\vec{r})$. The analog equation to (2.18) for the case of cross-correlation is shown here

$$G_{\mathrm{CC},1}(\tau) = \frac{\int_{V'}\int_{V} W_1(\vec{r})\, W_2(\vec{r}\,')\, \Phi(\vec{r},\vec{r}\,',\tau)\, d^3\vec{r}\, d^3\vec{r}\,'}{\left(\int_V W_1(\vec{r})\, \langle C(\vec{r},t)\rangle\, d^3\vec{r}\right)\, \left(\int_V W_2(\vec{r})\, \langle C(\vec{r},t)\rangle\, d^3\vec{r}\right)} \tag{2.46}$$

$$G_{\mathrm{CC},2}(\tau) = \frac{\int_{V'}\int_{V} W_2(\vec{r})\, W_1(\vec{r}\,')\, \Phi(\vec{r},\vec{r}\,',\tau)\, d^3\vec{r}\, d^3\vec{r}\,'}{\left(\int_V W_1(\vec{r})\, \langle C(\vec{r},t)\rangle\, d^3\vec{r}\right)\, \left(\int_V W_2(\vec{r})\, \langle C(\vec{r},t)\rangle\, d^3\vec{r}\right)}\,. \tag{2.47}$$

In the standard case the two foci are identical, but shifted by the distance R, so they are described by the same molecule detection function shifted by R

$$W_1(\vec{r}) = \exp\left(-\frac{2(x^2+y^2)}{\omega_0^2} - \frac{2z^2}{z_0^2}\right) \tag{2.48}$$

$$W_2(\vec{r}) = \exp\left(-\frac{2((x-R)^2+y^2)}{\omega_0^2} - \frac{2z^2}{z_0^2}\right). \tag{2.49}$$

Translational Diffusion

For the case of only translational diffusion we use eq. (2.22) for the concentration correlation function and get for the model function

$$G_{\mathrm{CC,i}}(\tau) = \frac{1}{\langle C(\vec{r},t)\rangle\, V_{\mathrm{eff}}}\, \frac{1}{1+\frac{4\,D\,\tau}{\omega_0^2}}\, \frac{1}{\sqrt{1+\frac{4\,D\,\tau}{z_0^2}}}\, \exp\left(\frac{-R^2}{\omega_0^2+4\,D\,\tau}\right). \tag{2.50}$$

Here both cross-correlations are identical, because molecules diffuse into all directions.

Translational Diffusion and Active Transport

In the case of active transport we use the concentration correlation function from eq. (2.33) and get for the model functions

$$G_{\mathrm{CC},1}(\tau) = \frac{1}{\langle N\rangle}\, \frac{1}{1+\frac{4\,D\,\tau}{\omega_0^2}}\, \frac{1}{\sqrt{1+\frac{4\,D\,\tau}{z_0^2}}}\, \exp\left(-\frac{v^2\,\tau^2 + R^2 - 2\,R\,v\,\tau\cos(\alpha)}{\omega_0^2+4\,D\,\tau}\right) \tag{2.51}$$

$$G_{\mathrm{CC},2}(\tau) = \frac{1}{\langle N\rangle}\, \frac{1}{1+\frac{4\,D\,\tau}{\omega_0^2}}\, \frac{1}{\sqrt{1+\frac{4\,D\,\tau}{z_0^2}}}\, \exp\left(-\frac{v^2\,\tau^2 + R^2 + 2\,R\,v\,\tau\cos(\alpha)}{\omega_0^2+4\,D\,\tau}\right) \tag{2.52}$$

in case that the flow is perpendicular to the optical axis (v_z=0) and the definition for v in eq. (2.36). The angle α is the angle between the flow velocity and the vector between the two foci. The second equation is the backward and the first the forward cross-correlation, which shows a peak, due to the fluorophores transported from volume one to volume two by the flow.

2.5 Dual-Color Fluorescence Cross-Correlation Spectroscopy

To study the interaction of molecules with autocorrelation is problematic, because the interaction can only be determined by a change in the diffusion coefficient. For globular proteins the diffusion coefficient is approximately proportional to the cubic root of the molecular mass, and therefore a change of the molecular weight by at least an order of magnitude is necessary to determine the interaction precisely [7]. Dual-color fluorescence cross-correlation spectroscopy enhances the sensitivity and resolution dramatically. Two spectrally separated laser lines are focussed into the same spot (Fig. 2.6(a)). The fluorescence from two spectrally distinct fluorophores diffusing through the confocal volume (Fig. 2.6(b)) is collected, spectrally separated and detected in two channels. Both intensity traces (Fig. 2.6(c)) are auto- and cross-correlated (Fig. 2.6(d)). If both fluorophores interact and diffuse together through the confocal volume, there is a correlation between the spectral channels, which give rise to a positive cross-correlation. Therefore, dual-color FCCS is a powerfull tool to study binding, because it measures dynamic colocalization.

In analogy to the spatial cross-correlation the cross-correlation for dual-color FCCS is defined. Instead of having fluorescence signals from two separated volumes, in dual-color FCCS there are fluorescent signals from two spectral channels, here called 'red' (r) and 'green' (g)

$$G_{\mathrm{AC,g}}(\tau) = \frac{\langle \delta F_{\mathrm{g}}(t) \cdot \delta F_{\mathrm{g}}(t+\tau) \rangle}{\langle F_{\mathrm{g}}(t) \rangle \langle F_{\mathrm{g}}(t) \rangle} \tag{2.53}$$

$$G_{\mathrm{AC,r}}(\tau) = \frac{\langle \delta F_{\mathrm{r}}(t) \cdot \delta F_{\mathrm{r}}(t+\tau) \rangle}{\langle F_{\mathrm{r}}(t) \rangle \langle F_{\mathrm{r}}(t) \rangle} \tag{2.54}$$

$$G_{\mathrm{CC,gr}}(\tau) = \frac{\langle \delta F_{\mathrm{g}}(t) \cdot \delta F_{\mathrm{r}}(t+\tau) \rangle}{\langle F_{\mathrm{g}}(t) \rangle \langle F_{\mathrm{r}}(t) \rangle} \tag{2.55}$$

$$G_{\mathrm{CC,rg}}(\tau) = \frac{\langle \delta F_{\mathrm{r}}(t) \cdot \delta F_{\mathrm{g}}(t+\tau) \rangle}{\langle F_{\mathrm{g}}(t) \rangle \langle F_{\mathrm{r}}(t) \rangle} \,. \tag{2.56}$$

The fluorescent signal in one spectral channel arises from all molecules which carry the distinct label, that is from all molecules having this label alone, and additionally from all which carry both labels. Therefore, the fluorescence fluctuations

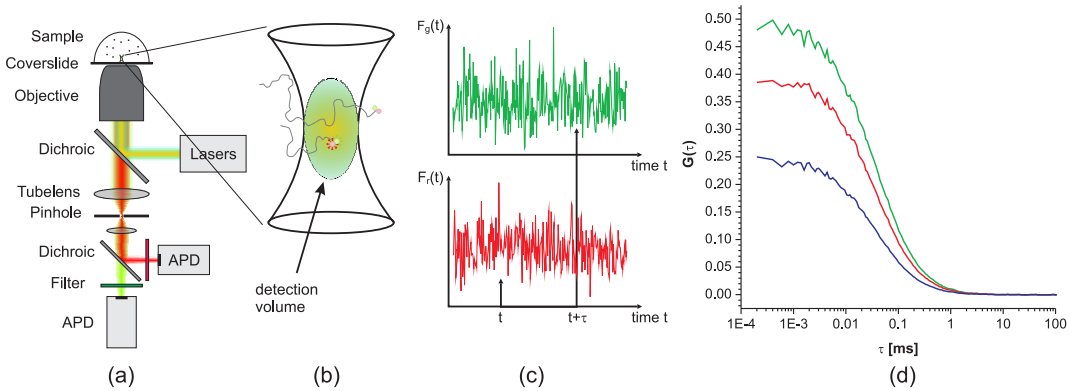

Figure 2.6: Principle of dual color FCCS: (a) Two spectrally separated laser lines are focussed into the same focus, and the collected fluorescence is spectrally separated by a dichroic beam splitter and emission filters into two spectral channels. (b) Spectrally distinct fluorophores, which diffuse to the detection volume, give rise to two fluctuating intensity traces (c). (d) Auto- (red, green) and cross-correlation (blue) curves calculated from the intensity traces. Only two different fluorophores which diffuse together give rise to the cross-correlation curve.

(eq. (2.10)) are

$$\delta F_{\mathrm{g}}(t) = \int_V W_{\mathrm{g}}(\vec{r})\,\eta_{\mathrm{g}}\,\delta(C_{\mathrm{g}}(\vec{r},t) + C_{gr}(\vec{r},t))\;d^3\vec{r} \tag{2.57}$$

$$\delta F_{\mathrm{r}}(t) = \int_V W_{\mathrm{r}}(\vec{r})\,\eta_{\mathrm{r}}\,\delta(C_{\mathrm{r}}(\vec{r},t) + C_{gr}(\vec{r},t))\;d^3\vec{r}. \tag{2.58}$$

In the general case the two detection volumes described by W_{g} and W_{r} do not overlap completely and have different sizes. Here the correlation functions for the simplified case of two identical detection volumes are shown

$$G_{\mathrm{AC,g}}(\tau) = \frac{\langle C_{\mathrm{g}}\rangle\, M_{\mathrm{g}}(\tau) + \langle C_{gr}\rangle\, M_{gr}(\tau)}{(\langle C_{\mathrm{g}}\rangle + \langle C_{gr}\rangle)^2\, V_{\mathrm{eff}}} \tag{2.59}$$

$$G_{\mathrm{AC,r}}(\tau) = \frac{\langle C_{\mathrm{r}}\rangle\, M_{\mathrm{r}}(\tau) + \langle C_{gr}\rangle\, M_{gr}(\tau)}{(\langle C_{\mathrm{r}}\rangle + \langle C_{gr}\rangle)^2\, V_{\mathrm{eff}}} \tag{2.60}$$

$$G_{\mathrm{CC}}(\tau) = \frac{\langle C_{gr}\rangle\, M_{gr}(\tau)}{(\langle C_{\mathrm{g}}\rangle + \langle C_{gr}\rangle)\,(\langle C_{\mathrm{r}}\rangle + \langle C_{gr}\rangle)\, V_{\mathrm{eff}}}, \tag{2.61}$$

with

$$M_i(\tau) = \frac{1}{1+\frac{\tau}{\tau_{D,i}}}\,\frac{1}{\sqrt{1+\frac{\tau}{S^2\,\tau_{D,i}}}} \tag{2.62}$$

for the case of translational diffusion.

Usually the most interesting parameter is the relative cross-correlation amplitude, which can be obtained from the amplitudes of the correlation curves

$$G_{\mathrm{AC,g}}(0) = \frac{1}{(\langle C_{\mathrm{g}}\rangle + \langle C_{gr}\rangle)\, V_{\mathrm{eff}}}\,, \qquad G_{\mathrm{AC,r}}(0) = \frac{1}{(\langle C_{\mathrm{r}}\rangle + \langle C_{gr}\rangle)\, V_{\mathrm{eff}}}\,, \\ G_{\mathrm{CC}}(0) = \frac{\langle C_{gr}\rangle}{(\langle C_{\mathrm{g}}\rangle + \langle C_{gr}\rangle)\,(\langle C_{\mathrm{r}}\rangle + \langle C_{gr}\rangle)\, V_{\mathrm{eff}}}\,, \tag{2.63}$$

to

$$\frac{\langle C_{gr}\rangle}{\langle C_{\mathrm{g}}\rangle + \langle C_{gr}\rangle} = \frac{\langle N_{gr}\rangle}{\langle N_{\mathrm{g}}\rangle + \langle N_{gr}\rangle} = \frac{G_{\mathrm{CC}}(0)}{G_{\mathrm{r}}(0)}\,, \\ \frac{\langle C_{gr}\rangle}{\langle C_{\mathrm{r}}\rangle + \langle C_{gr}\rangle} = \frac{\langle N_{gr}\rangle}{\langle N_{\mathrm{r}}\rangle + \langle N_{gr}\rangle} = \frac{G_{\mathrm{CC}}(0)}{G_{\mathrm{g}}(0)}\,. \tag{2.64}$$

The amount of interacting particles compared to all green particles can be obtained by dividing the amplitudes of the cross-correlation curve by the amplitude of the red autocorrelation curve, and the fraction of interacting particles normalized to all red particles is given by the ratio of the cross-correlation amplitude and the amplitude of the green autocorrelation curve.

2.6 Problems and Artifacts in Fluorescence Correlation Spectroscopy

Due to the high sensitivity of FCS and the influence of the sample onto the optical beampath, the results obtained by FCS can easily be influenced by artifacts.

Correlation curves can easily be biased, due to the correlation mechanism. If the measurement time is chosen too short, the shape of the correlation curve will be distorted, and the slow dynamics will be lost. Especially if slow dynamics shall be resolved, providing adequately long measurement times is crucial.

2.6.1 Optical Artifacts in Fluorescence Correlation Spectroscopy

The real confocal volume differs from its approximation by a 3D-gauss-model eq. (2.19). A comparison between the 3D-gauss-approximation and a calculation of a real confocal volume can be seen in Fig. 2.7. The isosurface, where the molecule detection function has fallen to $1/e^2 \approx 0.13$ of its maximum, looks like a cylinder with rounded ends [108]. For freely diffusing fluorophores in 3D the deviations from the 3D-gauss model can be neglected. But it has to be kept in mind that evaluation of the effective volume from a fluorophore, with a known diffusion coefficient, does not describe the actual dimensions of the detection volume [7]. For the determination of the diffusion coefficient of molecules diffusing in a two-dimensional membrane, the deviation of the real detection volume from the 3D-Gauss-model has to be acknowledged, because the x-y sections are larger in

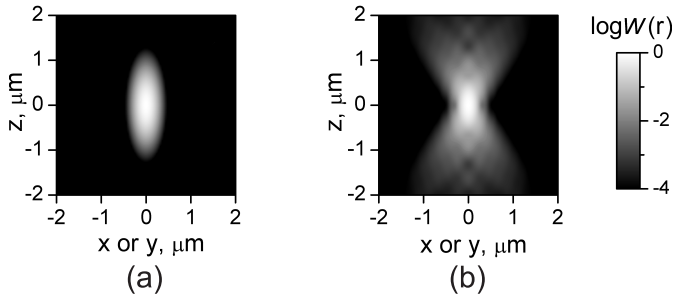

Figure 2.7: Shape of confocal volumes: (a) The shape of a 3D Gaussion model. (b) Real shape from a theoretical calculation, both taken from [7].

an out of focus plane compared to the focal plane. Therefore, the z-scan method should be used [109, 110].

The excitation laser beams are usually linearly polarized. The focussing of a linearly polarized laser beam with a high-NA objective results in an elliptical cross-section of the confocal volume, but the deviations from a round cross-section are really small [108, 111] and can be neglected.

Cover-Slide Thickness

All high NA objectives used today are corrected for the use with a cover-slide. For FCS, even more elaborated objectives are used, which have a correction ring to adjust the cover-slide thickness. The effects of a mismatched cover-slide thickness were studied in [108] showing an error of around 100 % for the concentration and around 30 % for the diffusion coefficient for 10 µm deviation. So the correction ring has to be adjusted carefully, because even high quality cover-slides have a thickness variation of ±10 µm.

Refractive Index Mismatch

Water-immersion objectives are corrected to image in a medium with the refractive index of water n=1.333. Most media, like buffers and cells, where FCS is used in, have a slightly different refractive index, ranging from 1.333 to 1.380. This leads to an error in the concentration estimation of 600 % and for the diffusion coefficient of 50 % [108]. For the calculation in [108] it was considered that the focus is 200 µm deep in the sample, because the longer the distance which the light travels through a refractive index mismatched medium, the stronger are the disturbances of the focal volume and the bigger are the errors. Measuring FCS close to the cover-slide, as it is done for example in adherent cells, strongly reduces these errors [112]. The errors induced by refractive index mismatch can be corrected at least partially by an adjustment of the cover-slide thickness correction ring [113]. Even

better result would be obtained by using an objective with a correction ring for the refractive index.

Laser Beam Astigmatism

Laser beam astigmatism describes the non-flatness of the optical wave-front, due to mirror curvature or the usage of optical waveguides. The errors are in the range of the errors of a mismatched cover-slide thickness and are biggest when using overfilling laser beams to create diffraction limited spots [108].

2.6.2 Triplet Blinking and Saturation

The effects of saturation and photobleaching (see section 2.6.4) are mostly present simultaneously. Saturation increases the apparent diffusion time, photobleaching decreases it. Which effect is the more dominant one, depends on the excitation laser power, the geometry of the sample, the diffusion coefficient and the photophysical properties of the fluorophore. While for fluorophores freely diffusing in 3D saturation effects dominate, the opposite is seen for fluorophores diffusing in a 2D membrane [7].

In section 2.3.2 the model function for triplet blinking was developed for the approximated case that the triplet rates are intensity independent. The errors due to this approximation are usually small, but the occupation of a triplet state

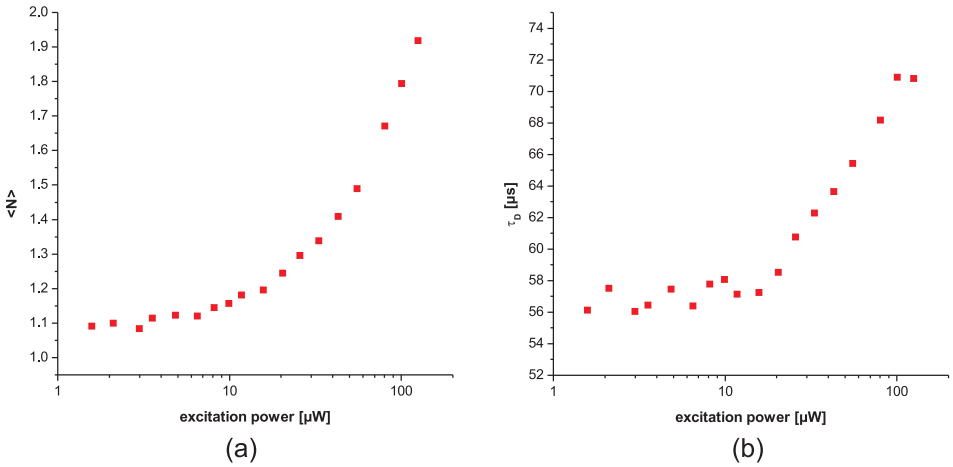

Figure 2.8: Effect of saturation: (a) Dependence of mean particle number $\langle N \rangle$ from the excitation power, with the increase of $\langle N \rangle$ due to saturation. (b) The same dependence for the diffusion time τ_D. Both measured with Alexa 488 on a home-built setup.

increases the saturation, due to the longer off-time of the fluorophores.

For the development of the triplet model function (eq. (2.41)) in section 2.3.2, it was assumed that the emission profile is the same as the excitation profile. Even for low excitation intensities this assumption can be violated. The fluorophores in the center of the confocal volume, which are excited with the highest intensities, can not absorb more photons, because the electronic ground state is already depleted. This leads to flattening of the emission profile, which is then approximated with a broader gaussian distribution, leading to longer apparent diffusion times τ_D and lower apparent concentration values (Fig. 2.8). The effect of saturation was studied in [106, 114, 115]. While in [114] a simple saturation model is used to explain the power dependence of the measured diffusion time and mean particle number, in [106] a simple model is derived to extract the correct parameters from an experimental autocorrelation curve, which was measured at modest laser powers. Excitation with pulsed laser increase saturation effects compared to cw-excitation [115]. The best way is of course to avoid saturation effects as much as possible, by the usage of modest excitation powers, where saturation effects are low.

2.6.3 Uncorrelated Background

Uncorrelated background influences the amplitude of the correlation curve and thereby the apparent concentration. The apparent diffusion coefficient is not influenced. There are many sources for uncorrelated background. At low count rates, the detector dark counts may be important, but also excitation light reaching the detector, due to insufficient blocking, stray light, or Raman scattering can play a role. In biological samples, the main source of uncorrelated background is autofluorescence. This is residual fluorescence from non-labeled molecules.

The correction is simply derived from eq. (2.5) by replacing the measured fluorescence intensity F with the real fluorescence intensity $\tilde{F}$ and the uncorrelated background signal B

$$F(t) = \tilde{F}(t) + B\,. \tag{2.65}$$

This leads to the following corrected or real correlation curves $\tilde{G}(\tau)$

$$\tilde{G}(\tau) = \frac{(\langle\tilde{F}\rangle + B)^2}{\langle\tilde{F}\rangle^2}\, G(\tau) \tag{2.66}$$

and for cross-correlation

$$\tilde{G}_{CC}(\tau) = \frac{\langle\tilde{F}_1\rangle + B_1}{\langle\tilde{F}_1\rangle}\, \frac{\langle\tilde{F}_2\rangle + B_2}{\langle\tilde{F}_2\rangle}\, G_{CC}(\tau)\,. \tag{2.67}$$

In the case of dual-color cross-correlation '1' has to be replaced by 'g' and '2' by 'r'.

2.6.4 Photobleaching

The property of fluorophores to photobleach leads to two types of photobleaching artifacts in FCS: Bleaching in the detection volume and depletion of fluorophores in the reservoir. The photobleaching probability is excitation intensity dependent, therefore artifacts due to photobleaching are usually present at high excitation laser powers. In *in vitro* measurements photobleaching can be reduced by the usage of anti-bleaching reagents, like ascorbic acid and 2-mercaptoethylamine (MEA) [116]. Also the reduction of oxygen in the buffer can prevent photobleaching, but leads usually to a strong built up of the triplet state population, because oxygen is known to quench the triplet states [116, 117]. Another approach to prevent bleaching, especially in samples with small diffusion coefficients, is scanning FCS [21, 22, 28].

Photobleaching in the Detection Volume

If the reservoir of the fluorophores outside the detection volume can be considered as infinite, the bleaching of fluorophores in the detection volume reduces the measured diffusion time, while the global concentration is not reduced. Due to the irreversible off-switching of the fluorophore, for the autocorrelation analysis it seems as the fluorophore has left the detection volume earlier, and therefore the estimated diffusion time τ_{D} is reduced. Usually autocorrelation curves with bleaching are fitted with the following model [117–119]

$$G(\tau) = \frac{1}{\langle N \rangle} \left(1 - f_{\mathrm{B}} + f_{\mathrm{B}}\, e^{-k_{\mathrm{PB}}\,\tau}\right) \frac{1}{1+\frac{\tau}{\tau_{\mathrm{D}}}} \frac{1}{\sqrt{1+\frac{\tau}{S^2\,\tau_{\mathrm{D}}}}}\,, \tag{2.68}$$

with the bleaching fraction f_{B} and the photobleaching rate k_{PB}. Due to the intensity dependence of the photobleaching rate, this is only a very approximate approach, and due to the fact that the highest excitation intensities are in the center of the detection volume, a central hole is burnt in the fluorophore distribution. Therefore, photobleaching should be avoided by using low enough excitation laser powers.

Depletion of Fluorophores due to Photobleaching

If the reservoir of fluorophores can not be considered as infinite, like in cells, photobleaching will lead to a depletion of fluorophores. In this case the autocorrelation curve is mainly influenced by the decreasing count rate, which leads to a strong distortion of the correlation curve. There are two ways to correct for this effect. In the first way the fluorescence intensity is divided into shorter pieces with a weaker decay. These pieces are autocorrelated, and the correlation curves are averaged [120]. This works only if the depletion is not too strong. A more general way is to

correct the fluorescence intensity before calculating the correlation curve. Therefore, the shape of the fluorescence intensity is fitted with one or more exponential functions, and the fluorescence intensity is transformed/rectified as described in [104, 120].

2.6.5 Detector Afterpulsing and Dead Time

Two detector artifacts play a role in FCS. The dead time is the time window in which a detector can not detect a second photon, after it detected the first one. This limits the temporal resolution and the maximal detectable fluorescence. The dead time artifact can be seen in the correlation curve as an anti-correlation at short time scales. For modern actively quenched APDs the dead time is around 100 ns, and therefore plays only a small role in present FCS experiments. The best way to avoid this artifact is to use the detector in its linear regime, which can be found for modern APDs below a fluorescent count rate of 500 kHz.

The second and more important artifact is afterpulsing. Here the detector creates a spurious pulse immediately after the detection of a photon. This leads to strong correlation on short time scales and is predominantly seen for low fluorescent count rates. It can be avoided by splitting the fluorescent signal on two detectors and calculating the cross-correlation curve, because the afterpulsing is not correlated between detectors. But this reduces the fluorescent intensity more than twice per detector, and therefore may be crucial in some experiments. In [121] a simple way is described how autocorrelation curves can be corrected for afterpulsing. Therefore, the afterpulsing probability of the detector has to be determined. Therefor, the autocorrelation curve $G_0(\tau)$ with a totally uncorrelated light source, like a battery driven LED, is obtained for the APD. Then the corrected autocorrelation curve $\tilde{G}(\tau)$ can be calculated from the measured curve $G(\tau)$ with the following formula

$$\tilde{G}(\tau) = G(\tau) - \frac{\langle F_0 \rangle}{\langle F \rangle} G_0(\tau)\,, \tag{2.69}$$

with the average fluorescence intensity $\langle F_0 \rangle$ of the calibration measurement, where $G_0(\tau)$ was obtained and the average fluorescence intensity $\langle F \rangle$ during the measurement of $G(\tau)$.

2.6.6 Problems of Fluorescence Correlation Spectroscopy *in vivo*

For FCS measurements in biological samples, especially in cells, some additional problems can occur. The problem of autofluorescence, which usually leads to an uncorrelated background, is treated in section (2.6.3). Often also a really slow diffusing or even immobilized fraction of fluorescent molecules exists, which is bleached in the beginning of the experiment. Artifacts in the correlation curves

due to this bleaching can be avoided by pre-bleaching the measurement spot: positioning the laser beam on the measurement spot for some seconds, without acquiring a correlation curve.

Especially by measurements in cellular compartments it happens that the compartment is smaller than the confocal volume. For this case completely new models have to be derived, which can be found in [122, 123].

The correlation curves measured in cells often decay slower than it would be expected in case of simple diffusion. This occurs, because the diffusion of the molecules can be hindered due to unspecific interactions or due to the crowded environment which is found in cells. This effect is often called anomalous diffusion [124–129], a concept were the mean square displacement grows slower than for free diffusion, usually as $\sim t^{\alpha}$, with $0 < \alpha < 1$. This concept is a rather mathematical model called fractional Brownian motion [130], without any particular underlying physical mechanism. The model function is derived in [7]

$$G(\tau) = \frac{1}{\langle N \rangle} \frac{1}{1 + (\tau/\tau_{\mathrm{D}})^{\alpha}} \frac{1}{\sqrt{1 + S^{-2}\,(\tau/\tau_{\mathrm{D}})^{\alpha}}}\,. \tag{2.70}$$

Due to the lacking underlying physical mechanism and no improvement in the fitting of our *in vivo* FCCS data by the anomalous diffusion model (2.70) compared to a two component model (2.32), the latter one is preferred in this work, as in [131].

2.6.7 Artifacts in Fluorescence Cross-Correlation Spectroscopy

The artifacts in fluorescence cross-correlation spectroscopy are crosstalk from one detection channel to the other and, for the case of dual-color FCCS, an imperfect overlap of the two detection volumes.

Spatial Crosstalk in 2f-FCCS

The major problem in two-focus FCCS is spatial crosstalk. Due to the gaussian intensity distribution perpendicular to the optical axis, the two foci overlap. The overlap decreases with increasing distance R and leads to spatial crosstalk. In a simple picture the fluorophores in the overlapping region are excited by both lasers simultaneously and the fluorescence of these fluorophores is detected in both channels and leads to positive cross-correlation for short lag times, called 'pseudo auto-correlation curve' [14]. This is not included in the theoretical derivation of the model function and has to be removed from the experimental data. In case of flow measurements larger distances R can be used, because many fluorophores travel through both volumes and give rise to the cross-correlation curve, due to their directed motion. By subtracting the backward from the forward cross-correlation curve the crosstalk can be totally removed, but this procedure also

removes completely the diffusion influence on the cross-correlation curve. In the case of stronger flows this is negligible, because the probability that fluorophores diffuse back against the flow is nearly zero. In the case of absolute measurements of the diffusion coefficient the distance R is small, and the problem of spatial crosstalk is solved by pulsed interleaved excitation (PIE) [16, 22].

Spectral Crosstalk in dual-color FCCS

A major problem in dual-color fluorescence cross-correlation spectroscopy is spectral crosstalk. Due to the long tail towards longer wavelengths in the emission spectra of organic fluorophores, detection of fluorescence from the 'green' fluorophore in the 'red' channel is not avoidable. 'Green' and 'red' stands for shorter and longer emission wavelengths, respectively. Spectral crosstalk can be avoided by pulsed interleaved excitation (PIE) [132, 133]. In most commercial FCS systems only continuous wave (cw) excitation is implemented, and therefore PIE can not be used to avoid spectral crosstalk. For this reason the recorded FCCS curves or the resolved fit parameters have to be corrected afterwards with the following formalism.

The measured fluorescence F depends on the emitted fluorescence $\tilde{F}$ by the following equations

$$F_\mathrm{g} = \tilde{F}_\mathrm{g} + \gamma\,\tilde{F}_\mathrm{r} \qquad\qquad F_\mathrm{r} = \tilde{F}_\mathrm{r} + \beta\,\tilde{F}_\mathrm{g}\,, \tag{2.71}$$

with γ and β the crosstalk from the 'red' fluorophore into the 'green' channel and vice versa, respectively. The crosstalk (leakage) coefficients γ and β can be determined by exciting only one kind of fluorophore, measuring the fluorescence in both channel and dividing the signal in the wrong channel by the signal from the correct channel. So $\gamma = F_\mathrm{g}/F_\mathrm{r}$ measured with 'red' fluorophores only and $\beta = F_\mathrm{r}/F_\mathrm{g}$ measured with 'green' fluorophores only. The real emitted fluorescence $\tilde{F}$ can be calculated with

$$\tilde{F}_\mathrm{g} = \frac{F_\mathrm{g} - \gamma\,F_\mathrm{r}}{1-\gamma\,\beta} \qquad\qquad \tilde{F}_\mathrm{r} = \frac{F_\mathrm{r} - \beta\,F_\mathrm{g}}{1-\gamma\,\beta}\,. \tag{2.72}$$

The measured correlation curve $G(\tau)$ is defined as in eq. (2.5), with the measured fluorescent intensities F

$$G_{i,j}(\tau) = \frac{\langle F_i(t)\,F_j(t+\tau)\rangle - \langle F_i\rangle\,\langle F_j\rangle}{\langle F_i(t)\rangle\langle F_j(t)\rangle} \tag{2.73}$$

and the real correlation curve $\tilde{G}(\tau)$ with the emitted fluorescence intensities $\tilde{F}$

$$\tilde{G}_{i,j}(\tau) = \frac{\langle \tilde{F}_i(t)\,\tilde{F}_j(t+\tau)\rangle - \langle \tilde{F}_i\rangle\,\langle \tilde{F}_j\rangle}{\langle \tilde{F}_i(t)\rangle\langle \tilde{F}_j(t)\rangle}\,. \tag{2.74}$$

Inserting eq. (2.72) gives for the real 'red' autocorrelation

$$\tilde{G}_{\mathrm{r}}(\tau) = \frac{\langle (F_{\mathrm{r}}(t) - \beta\, F_{\mathrm{g}}(t))\,(F_{\mathrm{r}}(t+\tau) - \beta\, F_{\mathrm{g}}(t+\tau))\rangle - \langle F_{\mathrm{r}}(t) - \beta\, F_{\mathrm{g}}(t)\rangle^2}{\langle F_{\mathrm{r}}(t) - \beta\, F_{\mathrm{g}}(t)\rangle^2} \tag{2.75}$$

and with the assumption $\langle F_{\mathrm{r}}(t)\, F_{\mathrm{g}}(t+\tau)\rangle = \langle F_{\mathrm{g}}(t)\, F_{\mathrm{r}}(t+\tau)\rangle$ and some simple mathematics follows

$$\begin{aligned}\tilde{G}_{\mathrm{r}}(\tau) = {} & \frac{\langle F_{\mathrm{r}}(t)\, F_{\mathrm{r}}(t+\tau)\rangle - \langle F_{\mathrm{r}}(t)\rangle^2 + \beta\,(\langle F_{\mathrm{g}}(t)\, F_{\mathrm{g}}(t+\tau)\rangle - \langle F_{\mathrm{g}}(t)\rangle^2)}{\langle F_{\mathrm{r}}(t) - \beta\, F_{\mathrm{g}}(t)\rangle^2} \\ & - \frac{-2\,\beta\,(\langle F_{\mathrm{g}}(t)\, F_{\mathrm{r}}(t+\tau)\rangle - \langle F_{\mathrm{g}}(t)\rangle\,\langle F_{\mathrm{g}}(t)\rangle)}{\langle F_{\mathrm{r}}(t) - \beta\, F_{\mathrm{g}}(t)\rangle^2}\,.\end{aligned} \tag{2.76}$$

With the definition from eq. (2.73) this can be written as

$$\tilde{G}_{\mathrm{r}}(\tau) = \frac{\langle F_{\mathrm{r}}(t)\rangle^2\, G_{\mathrm{r}}(\tau) + \beta^2\,\langle F_{\mathrm{g}}(t)\rangle^2\, G_{\mathrm{g}}(\tau) - 2\,\beta\langle F_{\mathrm{r}}(t)\rangle\,\langle F_{\mathrm{g}}(t)\rangle\; G_{\mathrm{CC}}(\tau)}{\langle F_{\mathrm{r}}(t) - \beta\, F_{\mathrm{g}}(t)\rangle^2} \tag{2.77}$$

and analog follows for the real 'green' autocorrelation curve

$$\tilde{G}_{\mathrm{g}}(\tau) = \frac{\langle F_{\mathrm{g}}(t)\rangle^2\, G_{\mathrm{g}}(\tau) + \gamma^2\,\langle F_{\mathrm{r}}(t)\rangle^2\, G_{\mathrm{r}}(\tau) - 2\,\gamma\langle F_{\mathrm{g}}(t)\rangle\,\langle F_{\mathrm{r}}(t)\rangle\; G_{\mathrm{CC}}(\tau)}{\langle F_{\mathrm{g}}(t) - \gamma\, F_{\mathrm{r}}(t)\rangle^2}\,. \tag{2.78}$$

For the real cross-correlation curve follows from eq. (2.74) with eq. (2.72)

$$\begin{aligned}\tilde{G}_{\mathrm{CC}}(\tau) = {} & \frac{\langle (F_{\mathrm{g}}(t) - \gamma\, F_{\mathrm{r}}(t))\,(F_{\mathrm{r}}(t+\tau) - \beta\, F_{\mathrm{g}}(t+\tau))\rangle}{\langle F_{\mathrm{g}}(t) - \gamma\, F_{\mathrm{r}}(t)\rangle\,\langle F_{\mathrm{r}}(t) - \beta\, F_{\mathrm{g}}(t)\rangle} \\ & - \frac{\langle F_{\mathrm{g}}(t) - \gamma\, F_{\mathrm{r}}(t)\rangle\,\langle F_{\mathrm{r}}(t) - \beta\, F_{\mathrm{g}}(t)\rangle}{\langle F_{\mathrm{g}}(t) - \gamma\, F_{\mathrm{r}}(t)\rangle\,\langle F_{\mathrm{r}}(t) - \beta\, F_{\mathrm{g}}(t)\rangle}\end{aligned} \tag{2.79}$$

and with the assumption $\langle F_{\mathrm{r}}(t)\, F_{\mathrm{g}}(t+\tau)\rangle = \langle F_{\mathrm{g}}(t)\, F_{\mathrm{r}}(t+\tau)\rangle$ and some simple mathematics follows

$$\begin{aligned}\tilde{G}_{\mathrm{CC}}(\tau) = {} & \frac{(1+\gamma\,\beta)\,(\langle F_{\mathrm{g}}(t)\, F_{\mathrm{r}}(t+\tau)\rangle - \langle F_{\mathrm{g}}(t)\,\rangle\,\langle F_{\mathrm{r}}(t)\rangle)}{(1+\gamma\,\beta)\,(\langle F_{\mathrm{g}}(t)\rangle\,\langle F_{\mathrm{r}}(t)\rangle)}\,\dots \\ \dots\, & \frac{-\beta\,(\langle F_{\mathrm{g}}(t)\, F_{\mathrm{g}}(t+\tau)\rangle - \langle F_{\mathrm{g}}(t)\rangle^2) - \gamma\,(\langle F_{\mathrm{r}}(t)\, F_{\mathrm{r}}(t+\tau)\rangle - \langle F_{\mathrm{r}}(t)\rangle^2)}{-\beta\,\langle F_{\mathrm{g}}(t)\rangle^2 - \gamma\,\langle F_{\mathrm{r}}(t)\rangle^2}\end{aligned} \tag{2.80}$$

With the definition from eq. (2.73) for the real cross-correlation curve follows

$$\tilde{G}_{\mathrm{CC}}(\tau) = \frac{(1+\gamma\,\beta)\,\langle F_{\mathrm{g}}(t)\,\rangle\,\langle F_{\mathrm{r}}(t)\rangle\, G_{\mathrm{CC}}(\tau) - \beta\,\langle F_{\mathrm{g}}(t)\rangle^2\, G_{\mathrm{g}}(\tau) - \gamma\,\langle F_{\mathrm{r}}(t)\rangle^2\, G_{\mathrm{r}}(\tau)}{(1+\gamma\,\beta)\,(\langle F_{\mathrm{g}}(t)\rangle\,\langle F_{\mathrm{r}}(t)\rangle) - \beta\,\langle F_{\mathrm{g}}(t)\rangle^2 - \gamma\,\langle F_{\mathrm{r}}(t)\rangle^2}\,. \tag{2.81}$$

In most cases there is no crosstalk from the 'red' fluorophores into the 'green' channel, so $\gamma = 0$ and eq. (2.77), (2.78) and (2.81) simplify to

$$\tilde{G}_{\mathrm{g}}(\tau) = G_{\mathrm{g}}(\tau) \tag{2.82}$$

$$\tilde{G}_{\mathrm{r}}(\tau) = \frac{\langle F_{\mathrm{r}}(t)\rangle^2\, G_{\mathrm{r}}(\tau) + \beta^2\, \langle F_{\mathrm{g}}(t)\rangle^2\, G_{\mathrm{g}}(\tau) - 2\,\beta \langle F_{\mathrm{r}}(t)\rangle\, \langle F_{\mathrm{g}}(t)\rangle\, G_{\mathrm{CC}}(\tau)}{\langle F_{\mathrm{r}}(t) - \beta\, F_{\mathrm{g}}(t)\rangle^2} \tag{2.83}$$

$$\tilde{G}_{\mathrm{CC}}(\tau) = \frac{\langle F_{\mathrm{g}}(t)\,\rangle\, \langle F_{\mathrm{r}}(t)\rangle\, G_{\mathrm{CC}}(\tau) - \beta\, \langle F_{\mathrm{g}}(t)\rangle^2\, G_{\mathrm{g}}(\tau)}{\langle F_{\mathrm{g}}(t)\rangle\, \langle F_{\mathrm{r}}(t)\rangle - \beta\, \langle F_{\mathrm{g}}(t)\rangle^2}\,. \tag{2.84}$$

Imperfect Overlap of Detection Volumes in 2f-FCCS

The dual-color FCCS model functions in eq. (2.59)-(2.61) were derived for the case of perfectly overlapping detection volumes. In reality this is often not the case. Due to different beam waist and different divergence of the excitation laser beams the detection volumes are shifted along the optical axis and have different sizes. In case of not shifted, but different sized detection volumes the maximum of the relative cross-correlation amplitude (eq. (2.64)) to the smaller volume increase and can even exceed one. For an explicit analytical treatment of this case see [104, 134].

Any shift of the detection volumes reduces the maximum of the relative cross-correlation amplitude, and therefore reduces the dynamic range of the cross-correlation measurements. This can be analytically handled using the formalism for 2f-FCCS from section 2.4.

The usual way to correct for imperfect detection volume overlap is to normalize all relative cross-correlation amplitudes to the relative cross-correlation amplitude of a cross-correlation standard. Highly purified double stranded DNA or RNA, where each strand carries one fluorophore is often used as a cross-correlation standard.

2.7 Data Evaluation

To extract the relevant parameters from a measured FCS curve a model function is fitted to the experimental data. This model has to be carefully selected by the experimenter, because the proper choice of a model is extremely important to obtain meaningful and stable parameters. This model is usually fitted to the experimental data using a nonlinear least square fitting algorithm. Such a fitting algorithm fits a model function $G(\tau, p_k)$, depending on the model parameters $p_k = [N,\, f_{\mathrm{T}},\, \tau_{\mathrm{T}},\, \tau_{\mathrm{D}},\, \ldots]$, to the experimental data $G_i(\tau_i)$, with τ_i the single measured time points, by minimizing the squared residuals

$$\mathrm{res}_i = G_i - G(\tau_i, p_k)\,. \tag{2.85}$$

To minimize the value $r(p_k)$

$$r(p_k) = \sum_{i=1}^{N} \mathrm{res}_i^2 \,, \tag{2.86}$$

which is the sum of the squared residuals, the nonlinear least square algorithm iteratively varies the model parameters p_k, beginning from start parameters $p_{0,k}$. Here the start parameters have to be carefully selected, otherwise the fitting algorithm may converge to a local instead of the global minimum or not at all.

The quality of a fit is usually measured by the reduced χ^2-value, which is defined by

$$\chi^2 = \frac{1}{N-p-1} \sum_{i=1}^{N} \left(\frac{G_i - G(\tau_i, p_k)}{\sigma_i} \right)^2 . \tag{2.87}$$

p is the number of model parameters p_k and σ_i the standard deviation at the data point i. For the reduced χ^2-value the fit residual at the data point i is compared with the statistical noise at the same point. In a fit, with a model perfectly describing the experimental data, the residuals are only given by the statistical noise, and therefore χ^2 is around one. If the model can not describe the experimental data completely, χ^2 is bigger than one, and if a χ^2 lower than one is achieved, the model contains too many parameters p_k and is able to fit some part of the statistical noise.

In FCS experiments many temporal orders of magnitude are covered. To avoid huge amounts of data and to limit the calculation time, multiple-tau correlators are used to calculate the correlation curves. In multiple-tau correlators the channel width increases with increasing lag times, and as a result the standard deviation σ depends on the lag time τ. The amplitude of the statistical noise is higher for short lag times compared to longer ones [135]. Therefore, the standard deviation σ_i has to be estimated for every data point i. There are several possibilities to estimate the standard deviation σ [104]:

- If the correlation curve is calculated by a software algorithm, the statistical noise can be extracted as well.
- The standard deviation can be estimated from the spread of different correlation curves, measured under the same conditions.
- The experimental curve is approximated by a smoothed curve $\bar{G}$ and the standard deviation is evaluated by the standard deviation of $\delta G_j = G_j - \bar{G}(\tau_j)$ with j running in a window around τ_i.

Due to the dependence of the standard deviation on the lag time τ a weighted fitting algorithm is advantageous in FCS. To perform a weighted fit, the residuals

are multiplied with a weight w_i. In a weighted fit

$$r(p_k) = \sum_{i=1}^{N} (\mathrm{res}_i \, w_i)^2 = \sum_{i=1}^{N} ((G_i - G(\tau_i, p_k)) \, w_i)^2 \tag{2.88}$$

is minimized. Usually the inverse of the standard deviation is used as a weight $w_i = 1/\sigma_i$. For this case the weighted nonlinear least square fitting algorithm minimizes χ^2. The scattering width of weighted residuals is then equal for all lag times.

Modern nonlinear least square algorithms, as they are implemented in Matlab, report confidence intervals for the model parameters. These confidence intervals report the range where the value of the parameter p_k is still compatible with the statistical noise of the data. They indicate the minimal uncertainties of the model parameters. For *in vivo* measurements the fitted parameters are averaged over several samples for example cells, and much bigger errors are calculated from the sample distribution of the parameters.

Two important issues should be mentioned. The first is cross dependence, this means that at least two model parameters are not independent from each other, so that a change in one parameter can be balanced by the other one. These parameters show big confidence intervals. In FCS this can be seen, for example, while fitting a correlation curve which contains afterpulsing, with a two-component model including triplet. Then the triplet part fits partially the afterpulsing. To compensate for the missing triplet part, the fast diffusion fraction is moved to shorter lag times, what has to be balanced by the slow diffusion fraction, which has orders of magnitude slower dynamics than the afterpulsing.

The second issue to be mentioned is over-estimation. This can easily be achieved by the usage of too many free model parameters. This reduces the χ^2 value, but the physical meaning behind the model parameters is lost. Therefore, the number of free model parameters should be reduced as much as possible, either by using a simpler model or by fixing some parameters to values obtained by calibration measurements. This will probably increase χ^2 and the fit will look worse, but the values of the parameters are more reliable.

3 Resolving the Flow Profile of a Micro-Pump by Two-Focus FCCS

3.1 Introduction

Miniaturization in biomedical and chemical engineering has greatly advanced from microfabrication technology, which was initially designed for microelectronics and computer technology. Propelled by the vision of a fully-functional, miniaturized laboratory on a single chip, called Lab-on-Chip (LoC) and micro Total Analysis System (μTAS) [136], this field has rapidly developed.

A key requirement for most of these miniaturized system is the handling and manipulation of fluid volumes in the micro- and nanoliter range. The present approaches [137] all lack behind the demand, either they show a pulsed mode of action (micromechanical pumps), may harm sensitive biological samples (electroosmotic and electrophoretic pumping) or are still macroscopic (syringe pumps). One way to circumvent these disadvantages is the application of electrohydrodynamic pumping [138, 139]. Laminar flow velocities of up to 80 μm/s could be achieved outside the pumping region [139], while in the regions where the pump electrodes are present, highly stable turbulent flow patterns were recognized. If microparticles were present in the fluid, a particle agglomeration occurred in well-defined regions of the pump.

Here the flow profile inside the pump was studied in detail by two-focus fluorescence cross-correlation spectroscopy (2f-FCCS), to use it for further optimization of the micropump and to study the possibility to accumulate and filter microparticles with a micropump.

The theory of fluorescence correlation spectroscopy (FCS) in samples with directed motion was developed in 1978 [140]. The standard FCS scheme with one detection volume was used to map flow velocities in microstructures [141–143], but it lacks the ability to detect the flow direction and can only be applied in samples, where the transition time due to flow is much shorter than these for diffusion. As an extension the technique and theory of spatial or two-focus fluorescence cross-correlation spectroscopy (2f-FCCS) was developed by Brinkmeier et al. [14]. The use of two foci (Fig. 2.5 (p. 17)) provide direction dependent information and the distance R between the two foci introduce an additional ruler, which allows calibration free measurements. 2f-FCCS was used to study flow profiles [14, 144], conformational changes of DNA hairpin structures [145, 146] and the photochemistry of Kaede [80]. To suppress the spatial crosstalk, two photon excitation, with

interleaved pulses was used [147]. Although 2f-FCCS was developed for flow measurements, it can be used in combination with pulsed interleaved excitation to measure absolute diffusion coefficients [16].

3.2 The Micropump

3.2.1 Theory of Electrohydrodynamic Pumping

Electrohydrodynamic pumping achieves a motion of the fluid through the interaction of the electric field with the dielectric fluid medium. The electric force $\vec{f}_{\mathrm{el}}$ per fluid volume element for an incompressible fluid can be expressed by

$$\vec{f}_{\mathrm{el}} = \rho_{\mathrm{el}}\,\vec{E} - \frac{1}{2}\,E^2\,\nabla\varepsilon\,, \tag{3.1}$$

where ρ_{el} is the electric volume charge, $\vec{E}$ is the electric field and ε is the medium permittivity [148]. The first term describes the Coulomb force, where the electric field acts on the free charges in the fluid medium and the second term represents the force due to the interaction of the electric field with polarization charges. The free charges can be generated through three mechanisms: inhomogeneities within the fluid, dissociation and direct charge injection, called *induction*, *conduction*, and *injection*, respectively.

Polarization forces as well as the *induction* mechanism require a gradient in the electric properties of the fluid. Thus, polarization and induction both depend on inhomogeneities in the electric properties of the fluid. The induction of charges in a inhomogeneous fluid can be best explained for a simple system containing two layered fluids with different electric properties (Fig. 3.1). The current density $\vec{j}$ has to fulfill the continuity equation $\nabla\, j = 0$, so the current density perpendicular to the interface $j_{\perp}$ ist the same on both sides. With the Maxwell equations and

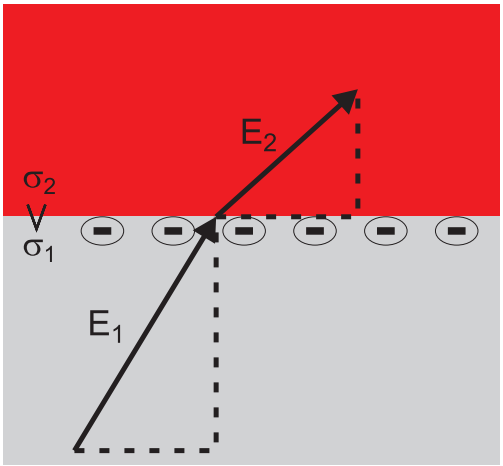

Figure 3.1: Schematic interface between two fluids with different conductivities $\sigma_{1/2}$ exposed to an electric field $\vec{E}$. Only the tangential components of the electric field are continuous across the interface This leads to a buildup of charges at the interface. With the shown orientation of the electric field and for $\sigma_1 < \sigma_2$ these charges are negative.

$\vec{j} = \sigma \vec{E}$ the surface charge is given by

$$\rho_S = E_{1\perp} \left(\varepsilon_2 \frac{\sigma_1}{\sigma_2} - \varepsilon_1 \right) = j_\perp \left(\frac{\varepsilon_2}{\sigma_2} - \frac{\varepsilon_1}{\sigma_1} \right). \tag{3.2}$$

With equal permittivities and $\sigma_1 < \sigma_2$ as in Fig. 3.1 the charges forming at the interface are negative. From the second part of equation (3.2) the charge relaxation time $\tau_{ch} = \varepsilon/\sigma$ can be defined and it follows that different charge relaxation times τ_{ch} are a precondition for the formation of net charges in the fluid bulk.

One way to induce different charge relaxation times are temperature gradients, because permittivity ε and conductivity σ of most liquids are temperature dependent. Temperature gradients are normally induced by ohmic heating, but also other methods like warming and cooling on different sides of the samples can be applied.

The formation of a double layer in liquids close to a charged solid surface also generates charges. Due to the Coulomb forces counter-ions are attracted to the charged surface, while co-ions are repulsed. At zero temperature the charges would perfectly cancel out each other, but at finite temperature thermal fluctuations lead to the formation of a charged layer of finite thickness.

The *conduction* process can also create a charged layer near the electrodes. Neutral electrolytic species can dissociate and recombine. The convection, diffusion, and migration of the generated ions in the electric field induce a current density, which gives the process its name. In strong electric fields the dissociation rate can exceed that of the recombination and create a non-equilibrium, heterocharge layer.

Charges can also be transferred directly from the electrodes into the fluid, what is called *injection*. To transfer charges from metal electrodes high field strength are required, therefore the *injection* process mainly occurs on the edges of the electrodes. This process is inadequate for many applications, because it often coincides with bubble formation, which may damage the electrodes. Additionally the charge injection changes the electric properties of the fluid and induce significant pH gradients.

To achieve a net flow in one direction a traveling electric wave is applied on the electrodes (Fig. 3.2). Such a wave creates charges by *induction* and *conduction* and for higher voltages also by *injection*. The electric field generates positive charges in the fluid below electrodes with positive potential and negative charges below electrodes with negative potential by *induction* and *injection*, while by the *conduction* mechanism opposite charges are generated. While the *conduction* and *injection* mechanisms only create charges close to the electrodes, the charges generated by *induction* span through the whole fluid, due to the overall temperature mechanism. If the electric wave travels a quarter period, a force is applied on the generated charges by the new electric field, leading to a net flow against the traveling wave direction for *induction* and *injection* and with the wave direction

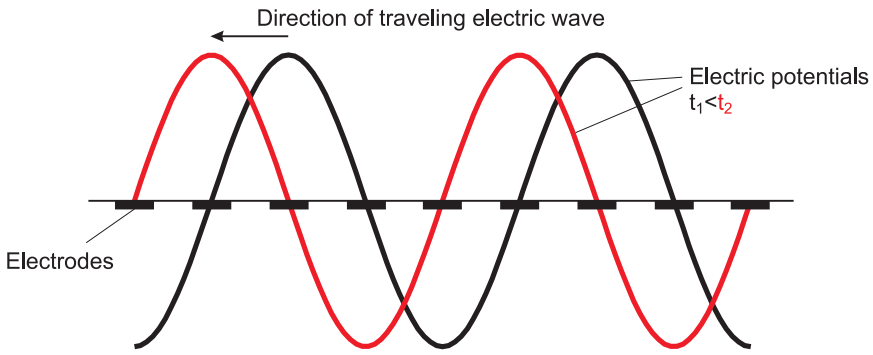

Figure 3.2: Traveling electric wave. In space periodical potentials are applied to the electrodes at a time point t_1 (black). On a later time point t_2 the potentials moved a quarter of the period to the left (red), forming a traveling electric wave.

for *conduction*. Which process is dominant depends on the used parameter set and determines the direction of the net flow. Most crucial is the synchronization of the travel velocity with the different charge relaxation and reaction times. These times can be influenced by adjusting the permittivity and conductivity of the fluid. The travel velocity depends on the frequency of the applied electric potential.

3.2.2 Manufacturing and Controlling of the Micropump

The micropump was designed by Maika Felten and her colleagues at the Fraunhofer Institute of Bio-Medical Techniques, Potsdam [148]. The channel is 200 µm

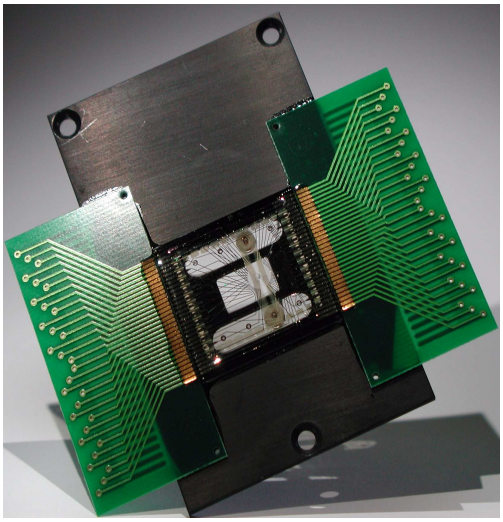

Figure 3.3: Micropump: The chip containing the micropump is mounted on a black metal plate, acting as a heat sink. The electrodes are connected with generator via the green circuit boards.

wide in the area of the electrodes and 100 µm elsewhere. 24 planar electrodes are on the roof of the channel and 36 on the bottom. The electrodes form stripes, stretch over the complete channel width, are 10 µm wide and the spacing between them is 10 µm. The micropump was manufactured by Gesim GmbH, Rossendorf. First the electrodes were structured by standard photo-lithographical techniques from Pt with an adhesion layer of Ti. Outside the channel the electrodes were passivated by a layer of silicon nitride. The channel was formed by a photo sensitive polymer layer and the channel was closed with a micro-patterned thin glass (170 µm) by a face to face adhesion technology, with positioning resolution better than 5 µm.

The traveling electric wave is generated by four rectangular signals, where the signal between neighboring electrodes is shifted by $\pi/2$ (Fig. 3.4). The rectangular signals are created by a high frequency generator, with four different phasings (Cytocon400, Cytoman-1, Evotec Technologies GmbH, Hamburg). The frequency is adjustable between 1 kHz and 12 MHz and is used to control the travel speed of the wave. The amplitude could be varied between 0 V and 10 V. By a wiring board between the generator and the micropump, every fourth electrode is driven with the same signal, having the same phase.

The in- and outlet of the micropump and a syringe were connected to a 4-way valve in such a way that either the pump could be filled by the syringe, or a closed loop was formed.

The laminar flow speeds outside the electrode array, were measured by fluorescence imaging of tracer beads on standard fluorescent microscope and the flow

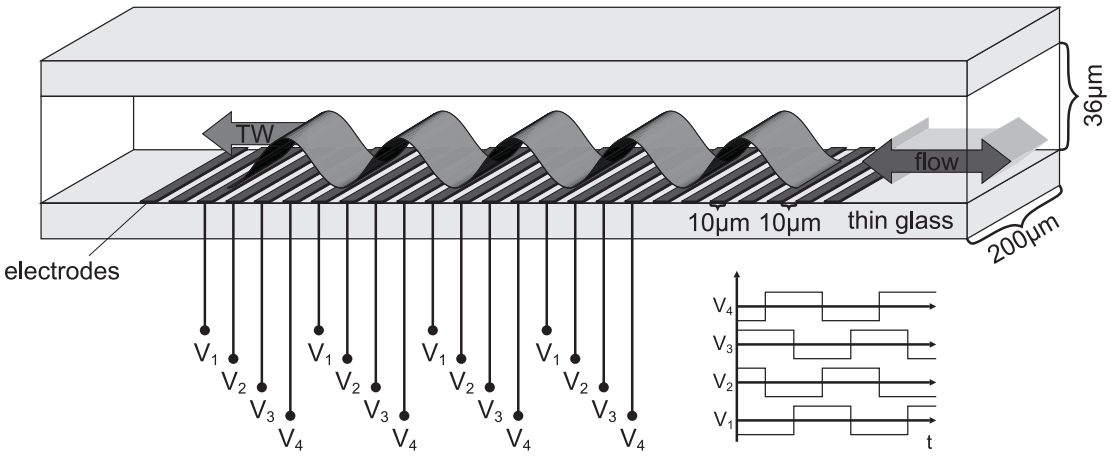

Figure 3.4: Micropump with applied electric potentials. Schematic drawing of the micropump with indication which potential is applied on which electrode. (For better visibility only bottom electrodes are shown.) Time course (lower right) of the applied potentials on four successive electrodes. Four rectangular potentials with phase shifts of $\pi/2$ are used.

speeds were estimated by a standard tracking algorithm. Inside the electrode array the complex flow patterns were mapped by two-focus fluorescence cross-correlation spectroscopy (2f-FCCS).

3.3 Two-focus Fluorescence Cross-Correlation inside the Micropump

3.3.1 Theoretical Considerations

The model functions for 2f-FCCS in the case of active transport were derived in section 2.4

$$G_{\mathrm{AC}}(\tau) = \frac{1}{\langle N\rangle}\,\frac{1}{1+\frac{4\,D\,\tau}{\omega_0^2}}\,\frac{1}{\sqrt{1+\frac{4\,D\,\tau}{S^2\,\omega_0^2}}}\,\exp\!\left(\frac{-v^2\,\tau^2}{\omega_0^2\,+\,4\,D\,\tau}\right) \tag{3.3}$$

$$G_{\mathrm{CC},1}(\tau) = \frac{1}{\langle N\rangle}\,\frac{1}{1+\frac{4\,D\,\tau}{\omega_0^2}}\,\frac{1}{\sqrt{1+\frac{4\,D\,\tau}{z_0^2}}}\,\exp\!\left(-\frac{v^2\,\tau^2+R^2-2\,R\,v\,\tau\cos(\alpha)}{\omega_0^2+4\,D\,\tau}\right) \tag{3.4}$$

$$G_{\mathrm{CC},2}(\tau) = \frac{1}{\langle N\rangle}\,\frac{1}{1+\frac{4\,D\,\tau}{\omega_0^2}}\,\frac{1}{\sqrt{1+\frac{4\,D\,\tau}{z_0^2}}}\,\exp\!\left(-\frac{v^2\,\tau^2+R^2+2\,R\,v\,\tau\cos(\alpha)}{\omega_0^2+4\,D\,\tau}\right). \tag{3.5}$$

The forward cross-correlation curve (eq. (3.4)) shows a characteristic peak (Fig. 3.5) and the position of the maximum directly corresponds to the flow velocity. In case of no diffusion ($D = 0$) the flow velocity v is given by the simple relation

$$v = \frac{R\cos(\alpha)}{\tau_{\max}}. \tag{3.6}$$

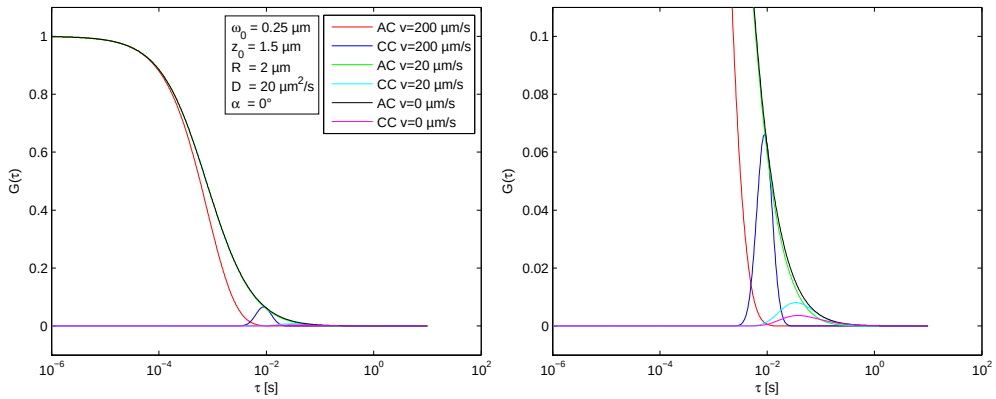

Figure 3.5: 2f-FCCS curves: Calculated auto- and cross-correlation curves for pure diffusion (v=0) and flow velocities of 20 and 200 µm/s.

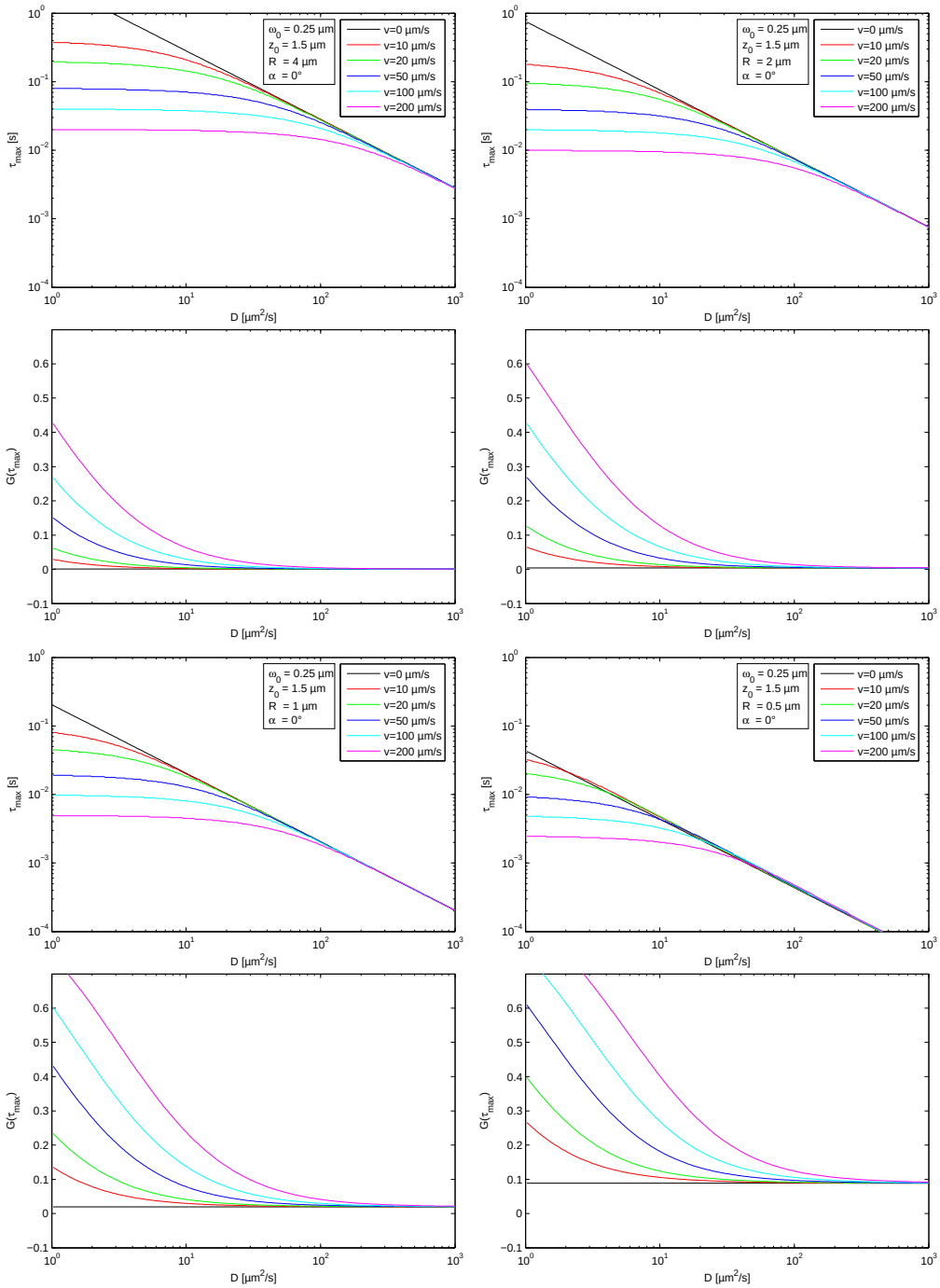

Figure 3.6: Position and amplitude of the cross-correlation peak: The position (lag time τ) and the amplitude of the cross-correlation peak in dependence on the flow velocity v over diffusion coefficient D is shown for decreasing distances of $R = 4$, 2, 1, and 0.5 µm.

To find the best experimental realization, the dependence of the resolvable velocity on the diffusion coefficient D and the distance R has to be studied. The results can be seen in Fig. 3.6 and show the position (lag time τ) and the amplitude of the cross-correlation peak for several distances R and several flow velocities v. It is clearly visible in the graphs that the velocity resolution increases with decreasing diffusion coefficient. For an increasing distance R the peak positions get more separated, but in contrast the amplitude of the peak decreases. For this reason, here a compromise has to be found that the peak is not lost in the noise of an experimental correlation curve.

The direction of flow only influences the amplitude of the cross-correlation peak and not the position (Fig. 3.7). Therefore, the direction of flow is only roughly distinguishable, because the peak amplitude is strongly influenced by experimental artifacts.

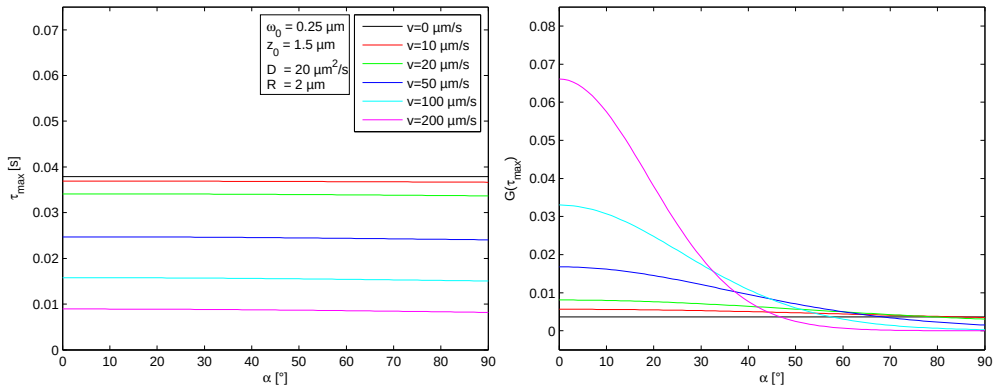

Figure 3.7: Direction dependence of the peak position: The position (lag time τ) and the amplitude of the cross-correlation peak in dependence on the flow direction α.

To conclude these theoretical considerations: A distance R between 1 and 2 µm would be a good compromise, between enough resolution of the peak position and a high enough peak amplitude. The resolution increases with decreasing diffusion coefficient, but decreasing diffusion coefficient means increasing particle size and thereby stronger direct influence of electric fields created by the micropump. The direction of the flow can only be roughly determined, if it is parallel or antiparallel to the vector between the two foci, because the amplitude of the peak is additionally influenced by experimental artifacts. For better direction estimation it is necessary to turn the sample, to find the angular position with the highest peak amplitude.

3.3.2 Experimental Realization

As a good compromise between a slow diffusion and not to big particles, CdSe/ZnS quantum dots (Adirondack Green, Evident Technologies) with a size of 20 nm at a concentration of 100 nM were used as fluorescent species. The aqueous solution had a conductivity of 35 mS/m. A driving voltage of 8 V and a frequency of 7 MHz was applied to the 36 electordes on the bottom (z=0) of the pump. All 2f-FCCS measurements were performed on a home-built setup (Fig. 3.8). The quantum dots were excited by the 488 nm line from an Ar-Kr-laser (Inova 70, Coherent). The laser beam was split and recollected by two beam splitters, creating two laser beams, which enter the objective (UPlanApo 60x/1.2 W, Olympus) with a small angular difference. Two foci with a distance R of 2.2 µm are created. Each foci was

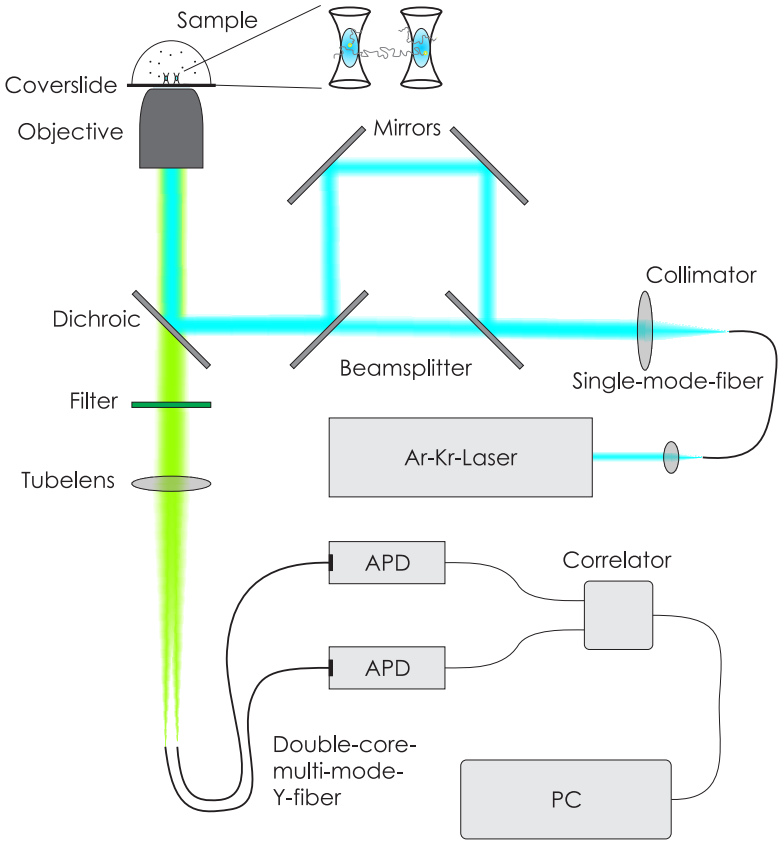

Figure 3.8: Home built 2f-FCCS setup: Two laser beams enter the objective with a small angular difference, creating two laser foci. The emitted fluorescence is collected with the same objective, spectrally filtered, directed onto a double-core multi-mode Y-fiber and detected with two APD. The signals from the APDs are correlated with a hardware correlator and evaluated with a PC.

3.3 µm high and 560 nm wide and had an effective volume of 0.73 fl. The emitted fluorescent light (λ=520 nm) was separated from the excitation light by a dichroic beam splitter (Q 505 LP, AHF, Tuebingen, Germany) and filtered by an emission filter (HQ 532/70, AHF). The fluorescent light from both foci was directed onto the one-end side of a double-core multi-mode Y-fiber, which splits into two fiber containing one core each, a so called bifurcated fiber (Avantes, RB Eerbeek, The Netherlands). The distance between the two cores was nominal 125 µm, which corresponds to a distance R of 2.1 µm between the two foci. The real distance of 2.2 µm was measured by imaging the foci with a CCD camera, therefor the imaging light path was calibrated with a ruler slide. The light from each core was detected by an avalanche photodiode (APD) (SPCM-CD 3017, Perkin Elmer). A hardware correlator (Flex-02-12D/B, Correlator.com, Bridgewater, NJ) processed the the signals from the APDs to obtain an autocorrelation curve from each spot and two cross-correlation curves, one in backward and one in forward direction. The fluorescent signals were collected 6 times for 60 s each at each position in the micropump.

The correlation curves were evaluated with a self-written Matlab script (The Mathworks). To remove the spatial crosstalk, the backward cross-correlation curve was subtracted from the forward cross-correlation curve, leading to the flow cross-correlation curve, as it is described by Brinkmeier et al. [14]. The flow cross-correlation curve and the autocorrelation curves were fitted globally with the model functions (3.3) and (3.4). As fit algorithm a weighted nonlinear least square algorithm was used. For a better estimation of the flow velocity the residuals of the flow cross-correlation curve were five times more weighted, than the residuals of the autocorrelation curves.

3.4 Results

The flow far away from the electrode array was already measured by detecting the tracks of fluorescent beads in the µm size using a standard fluorescent microscope and shows a laminar Poiseuille flow profile [139]. For the parameter set which we used for the 2f-FCCS measurements the maximum Poiseuille flow speed was 48 µm/s. Above the electrode array the flow pattern were too complex to be resolved by the usage of tracer beads (Fig. 3.9). Additionally tracer beads of µm size are affected by dielectrophoretic forces directly, so that their motion can not be attributed to hydrodynamic drag forces alone. For the quantum dots, with a diameter of 20 nm which were used for the 2f-FCCS measurements the influence of the dielectrophoretic forces can be neglected.

Representative correlation curves are shown in Fig. 3.10. These curves were measured at position x=280 µm, y=100 µm, z=10 µm. The calculated flow cross-correlation curve and its fit is plotted in addition to the measured auto-, forward

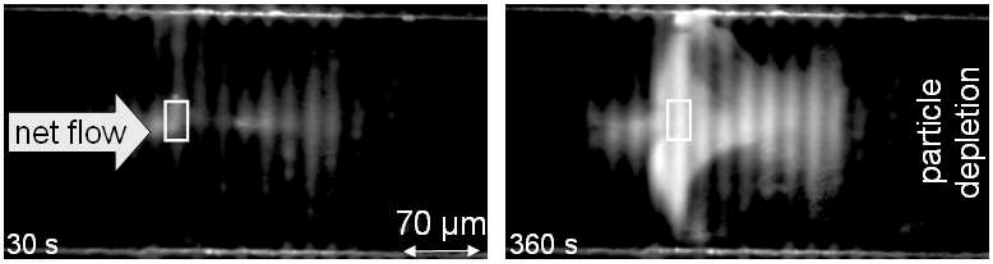

Figure 3.9: Accumulation of particles. Fluorescent particles with a diameter of 200 nm become trapped due to the interaction of hydrodynamic and dielectrophoretic forces. (Measurement by Maika Felten, Fraunhofer-IBMT, Potsdam.)

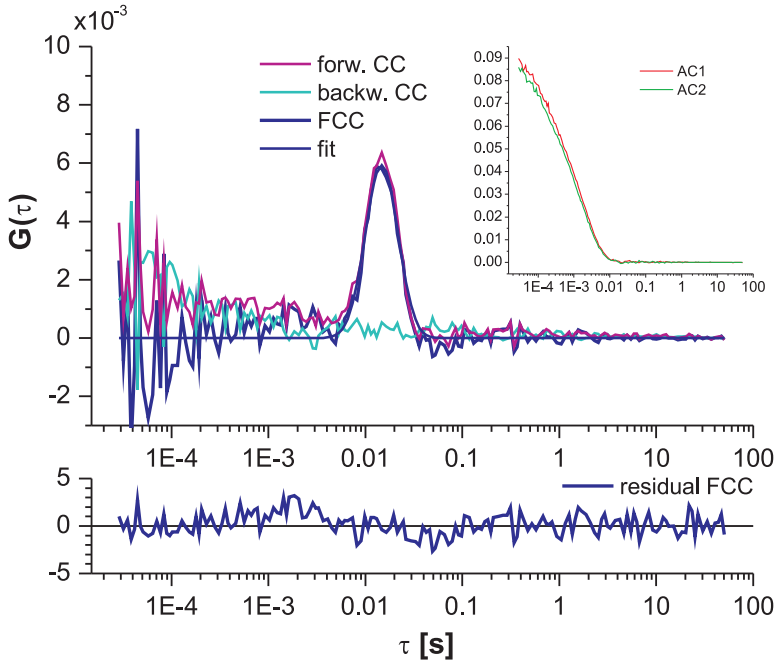

Figure 3.10: Two-focus correlation curves. Correlation curves measured at position x=280 µm, y=100 µm, z=10 µm. In addition to the measured forward and backward cross-correlation curves (CC) the flow cross-correlation curve (FCC) is plotted, which is calculated by subtraction of the backward from the forward cross-correlation curve. The autocorrelation curves (AC) are plotted in the inset. The correlation curves were fitted as described in the text and a flow velocity of 126 µm/s was determined. The weighted residuals of the fit are plotted in the lower graph.

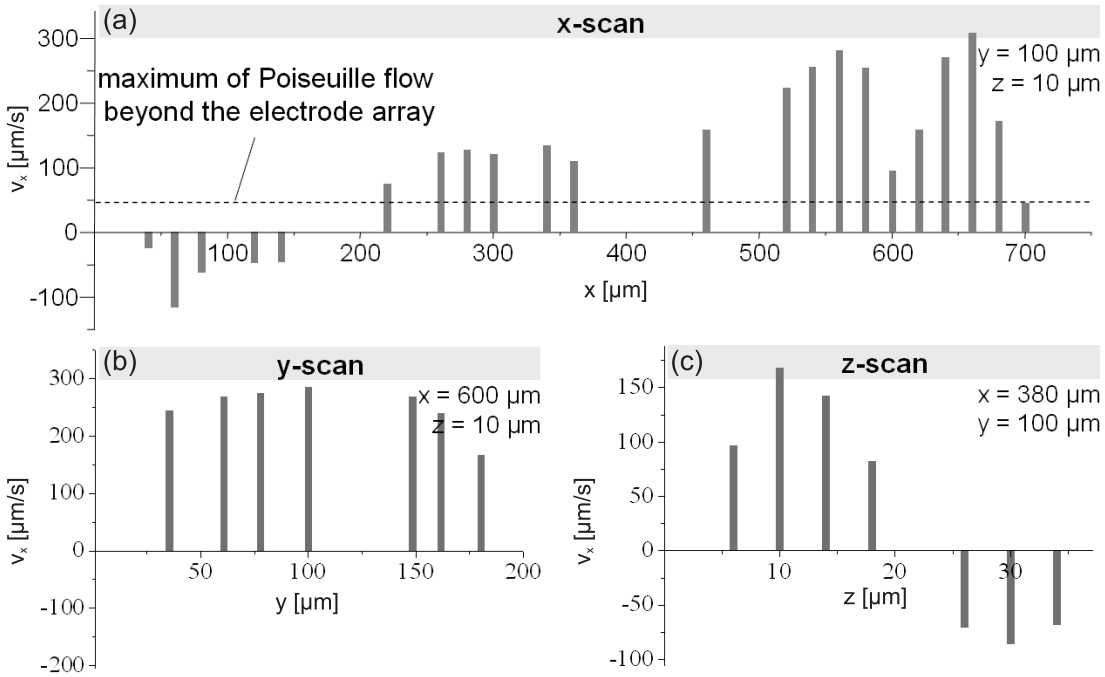

Figure 3.11: 2f-FCCS flow profiles. Flow velocities in direction along the channel measured with 2f-FCCS along three mutually perpendicular lines above the electrode array. The flow above the electrode array is less regular than the Poiseuille flow profile outside the electrode array. The flow direction changes in the x-scan (a) and the z-scan (c). Negative signs indicate a flow opposite to the direction of the net flow. The maximum flow velocity of the Poiseuille net flow outside the electrode array is indicate by the dashed line in (a).

and backward cross-correlation curves. The lower graph shows the weighted residuals from the global fit. The fitting algorithm resolved a flow velocity of 126 µm/s at this position.

To map the velocity profile in the micropump above the electrode array the position of the two foci was systematically scanned through the channel volume. The results from all 2f-FCCS measurements are summarized in Fig. 3.11. The graphs represent scans along three mutually perpendicular axes. Positive velocity values indicate a flow in the direction of the net flow measured outside the electrode array. The x-scan along the channel axis was detected 10 µm above the electrode plane at half of the channel width. Position x=20 µm is in the middle between the first and second electrode (electrodes are 10 µm wide and uncovered room between the electrodes is also 10 µm wide). Above the left part of the electrode array, the flow runs opposite to the direction of the net flow (Fig. 3.11(a)). For x-values larger than 200 µm, i.e. behind the tenth electrode, the flow direction reverses and coincides with the net flow direction. Between 500 and 700 µm, the

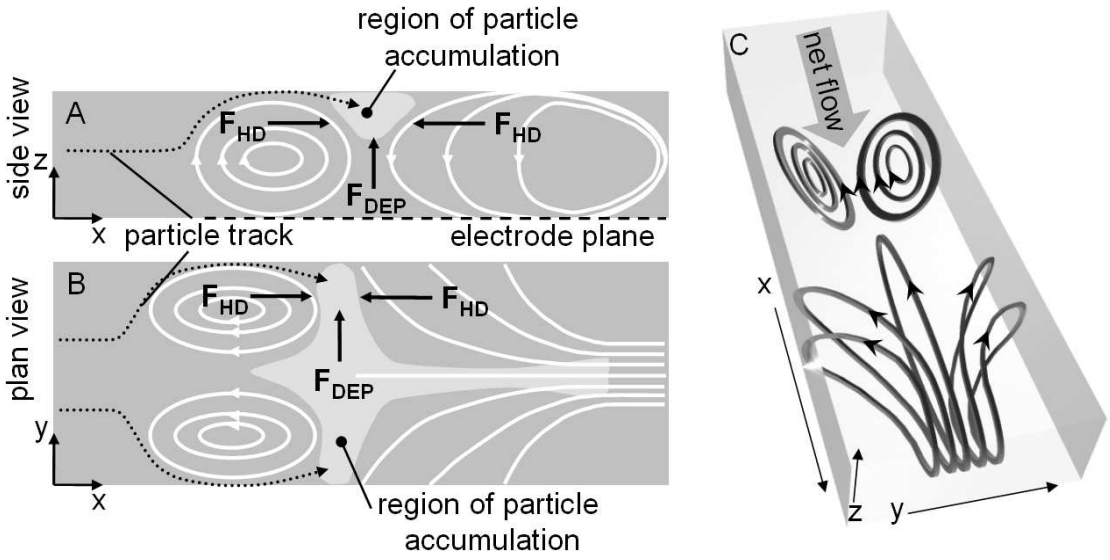

Figure 3.12: Scheme of flow pattern. Flow pattern as derived from visual particle tracking and from 2f-FCCS measurement. Additionally the forces are drawn, which act on the particles. The vortical streaming exerts hydrodynamic forces on the particles. These forces cause the motion of the particles away from the cores of the vortices. The particles move towards the regions between two adjacent vortices. Additionally, DEP forces act on the particles. They prevent the particles from approaching the channel bottom and push them from the channel center towards the sidewalls, where the electric field is lower.

flow is fastest and reaches velocities of up to 300 µm/s. This is approximately six times the maximum flow velocity of the Poiseuille flow outside the electrode array (line in Fig. 3.11(a)).

The y-scan was also measured 10 µm above the electrodes at x = 600 µm (Fig. 3.11(b)). The distribution of measured flow velocities is well approximated by a parabolic profile.

Along the z-direction, a reversal of the flow is observed for larger z-values (Fig. 3.11(c)). Here, the zero-crossing point is located in the middle of the channel. However, the flow showing a positive sign and being closer to the electrodes is approximately two times faster than the backflow observed near the channel top. Consequently, more liquid is transported along the positive x-direction than in the opposite direction. This pattern is compatible with the positive net flow.

Figure 3.12 summarizes the flow pattern obtained from the 2f-FCCS measurements together with the results of tracer bead imaging above the electrode array. The sketch shows a flowline pattern, which features two vortices of different size rotating in opposite directions. The front vortex rotates in the direction of the net flow and the planes that are associated with closed flow lines are tilted. The rear vortex rotates against the net flow direction and the planes of the closed flow lines

are bent. The fluorescence cross-correlation spectroscopy (FCCS) measurements showed the existence of the vortices and their rotation direction, while the particle imaging resolved the positioning, tilting and bending of the vortices.

3.5 Discussion

A complex flow behavior was observed in the electrohydrodynamic micropump, where fluidic transport is usually dominated by laminar flow lines. Propagating electric fields generated by arrays of microelectrodes act in a complex manner not only on the fluidic medium but also directly on the particles, if they are bigger than 50 nm to 100 nm. For this reason, 2f-FCCS was applied to determine the flow profile, as it allows the introduction of probes that are not affected by the electric field. Quantum dots with a diameter of 20 nm were used as these probes. Since the dielectrophoretic force is proportional to the particle volume, they experienced an electric force which was by more than one order of magnitude below that on the smallest particles which exhibited accumulation. Hence, the application of 2f-FCCS allowed us to distinguish between forces that act on volume elements of the fluid medium and forces directly acting on particles. In addition to electric forces, thermal convection may also play a role, as the field distribution leads to localized ohmic heating.

The observation of the particle flow and the 2f-FCCS both provide evidence for the occurrence of two flow vortices above the electrodes. They rotate in opposite direction (Fig. 3.12). The rear vortex is probably formed by the combination of a localized force field above the electrode array and the flow resistance in the confined microchannel geometry. At the rear end of the array, the accelerated fluid elements experience a strong flow resistance. The flow evades into that part of the channel, where the electrohydrodynamic forces are too weak to counteract the flow resistance. The 2f-FCCS data do not allow integrating the flow density over the entire cross-section of the channel. However, the higher positive flow velocities measured in the lower half of the microchannel close to the electrode array are compatible with the positive net flow measured distant from the electrodes (Fig. 3.11). A vertical component of the flow profile may be due to temperature convection. Its action might be most effective just at the rear end of the array where the flow experiences a strong resistance.

At the front vortex, the flow profile as measured using 2f-FCCS contradicts the theoretical predictions [148]. It remains unclear which physical effect contributes to the generation of the front vortex.

The ability to generate a well-defined vortical flow on a micrometer scale provides the possibility to manipulate nanosized particles through hydrodynamic forces. To explain the accumulation of particles, the behavior of a particle in a vortical flow is considered. When a particle is exposed to a vortex, radial forces

act on the particle [149], e.g., centrifugal force, pressure gradient force, and Stokes drag. The crucial parameter determining whether the resulting radial force component points towards the center of the vortex or in the outward direction is the ratio between the liquid density ρ_l and that of the particle ρ_p. For ratios $\rho_\mathrm{l}/\rho_\mathrm{p} < 1$, theory predicts the ejection of particles from the vortex center [150, 151] which was confirmed by several experimental investigations [152, 153]. Here, $\rho_\mathrm{l}/\rho_\mathrm{p} = 0.95$, what suggests that particles should accumulate between the vortices. An enrichment was observed in this region. However the particles were confined to the channel wall opposite to the electrode array. This behavior is explained by dielectrophoretic forces. In the applied frequency regime, negative dielectrophoresis acts on the particles such that the force vector points against the field gradient and particles are repelled away from the array towards the upper channel wall. As the strength of the dielectrophoretic force is proportional to the volume of particles, the process of accumulation is more effective for larger particles than for smaller ones.

The micropump has to be further optimized to function as an effective filtering or enrichment device. A more complex design of the electrode arrays may offer various options for defining regions in the channel where enrichment or depletion of particles prevail. Narrow side channels that enter at positions where maximum particle density is achieved are considered as design elements that allow to continuously extract particles for producing concentrated particle suspension. For example this could be used to accelerated the still complex and tedious task of enriching viruses from diluted samples for testing purposes.

The formation of vortices reduces the efficiency of the electrohydrodynamic pumping. If one runs the device as a pump, the elimination or reduction of these vortices is desirable. A more complex electrode pattern may suppress the formation of vortices. To ascertain the most effective way of avoiding the vortices, more complex simulations together with design variations of the device are necessary.

For both optimization directions all kinds of FCS, which can measure flow, like 2f-FCCS or scanning FCS [26, 154] may be used to discriminate between hydrodynamic and dielectrophoretic forces.

3.6 Conclusion

The flow pattern inside a pumping microdevice was analyzed by 2f-FCCS. The microdevice allows the generation of an electric traveling wave along a linear array of microelectrodes in a fluidic channel, which can be used to pump small volumes of liquid media through microfluidic channels and to filter and accumulate micro- and nanoparticles from suspensions.

Such a microdevice using the electrohydrodynamical principle displays a complex flow profile, which is not resolvable by common techniques. Additionally

dielectrophoretic forces act on particles larger than 50 nm to 100 nm, preventing the elucidation of the pure electrohydrodynamic forces. Here the flow profile of such a pump was mapped by 2f-FCCS using small (20 nm) quantum dots as fluorescent particles. The combination of the flow velocity map, resolved by 2f-FCCS with the results from the bead imaging allowed the reconstruction of a complex flow pattern, consisting of two vortices of different sizes and opposite directions of rotation. This flow pattern explained the observed complex particle trajectories in the force field and the accumulation of particles in well-defined regions above the microelectrode array. Only the high precision of 2f-FCCS in measuring flow velocities even with small fluorescent particles made it possible to separate the electrohydrodynamic forces acting on the solvent from the dielectrophoretic forces acting on larger particles. This allowed the elucidation of the correct flow pattern inside the micropump.

4 RNA Interference

4.1 The Discovery of RNA Interference

Small double stranded RNAs (dsRNAs) have emerged as key regulators of gene expression, acting in an evolutionary conserved group of post-transcriptional gene silencing (PTGS) pathways found in eukaryotes. The discovery of these PTGS mechanisms especially of RNA interference (RNAi), where dsRNAs trigger the degradation of complementary messenger RNAs (mRNAs) revolutionized loss-of-function studies in many organisms. RNAi is now commonly used to study the role of a gene and has a great perspective in medical applications due to its high specificity.

Early experiments in plants and the worm C. elegans found a dramatic reduction in gene expression, if additional copies, antisense or sense RNA strands of this gene were introduced in the organism [155–157]. The mechanism leading to this strong silencing of gene expression was not understood, until Fire et al. discovered RNA interference in 1998 [158]. They injected dsRNA into C. elegans and found knock down of the corresponding genes, with much higher efficiency than single stranded sense or antisense RNA alone. In the following years RNAi was found in Drosophila [159], zebrafish [160, 161] and in mammals [162, 163].

The real effector molecules of RNAi were first identified in plants [164] and later also found in animals [165, 166]. These, around 20 nt long dsRNAs, are called short interfering RNAs (siRNAs).

In the early years RNAi was induced by long dsRNAs. In mammals these long dsRNAs lead to the activation of the unspecific interferon mediated immune response, which results in an overall block of translation and finally in Apoptosis. Therefore, RNAi experiments were impossible in mammals until Elbashir and coworkers demonstrated that siRNAs can induce RNAi in mammalian cells [167].

The second class of short RNAs the micro RNAs (miRNAs) was discovered 1993 in C. elegans [168]. Lee et al. found a 21 nt and a 61 nt long RNA encoded in the gene lin-4 and complementary sequences in the 3' untranslated region (UTR) of the gene lin-14. They proposed that lin-4 regulates lin-14 by a RNA-RNA-interaction. Many more miRNAs were identified in C. elegans, Drosophila melanogaster and humans [169–171], many of them are widely conserved among these animals. Now it is known that miRNA-mediated gene silencing is a strongly conserved mechanism, with over 800 known human miRNAs [172] regulating more than 60 % of all human gene coding sequences [173–175].

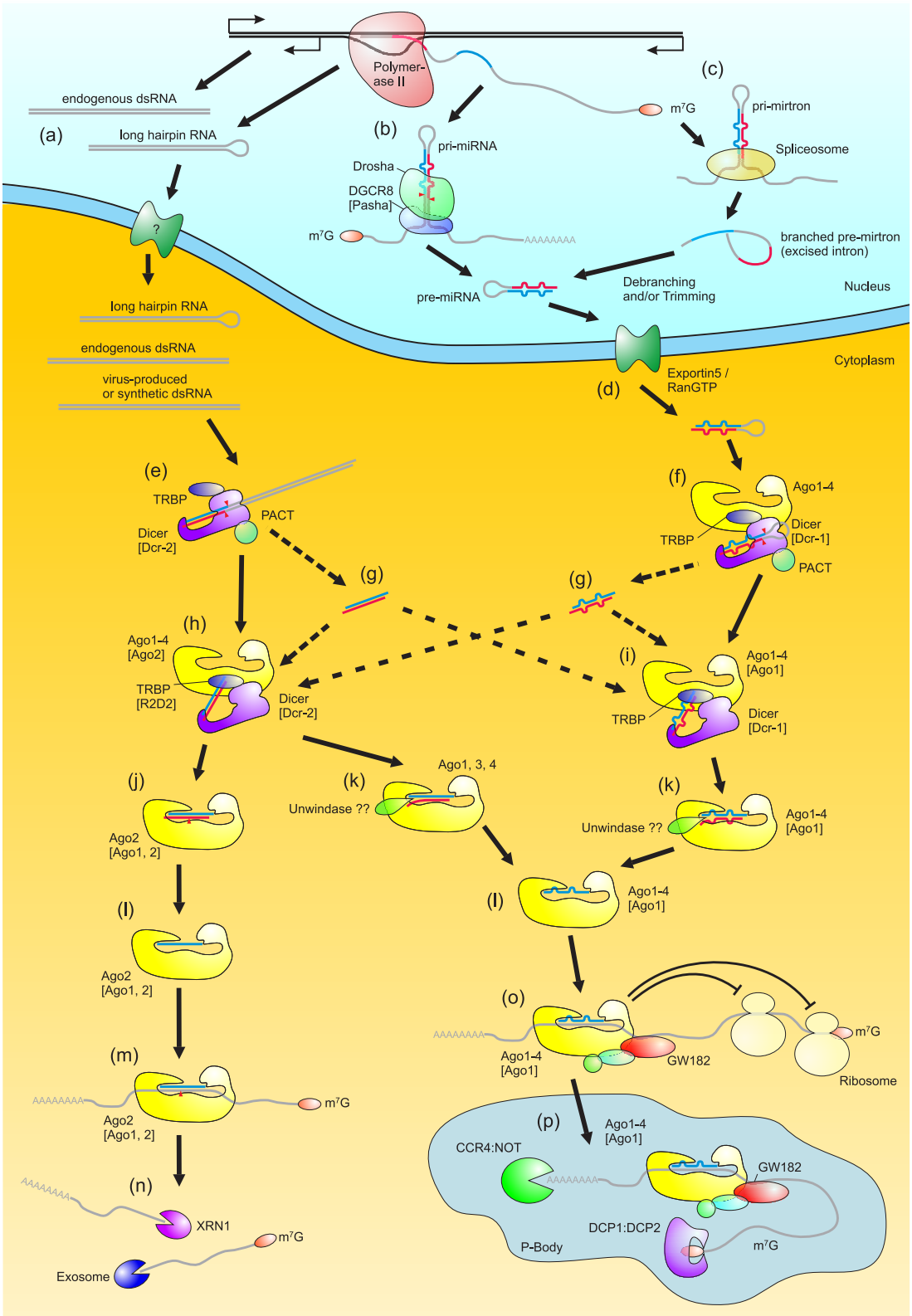
Polymer-
ase II
endogenous dsRNA
(a)
long hairpin RNA
(b)
pri-miRNA
Drosha
DGCR8
[Pasha]
m7G
AAAAAAAA
(c)
m7G
pri-mirtron
Spliceosome
branched pre-mirtron
(excised intron)
?
pre-miRNA
Debranching
and/or Trimming
Nucleus
Cytoplasm
long hairpin RNA
endogenous dsRNA
virus-produced
or synthetic dsRNA
Exportin5 /
RanGTP
(d)
(e)
TRBP
PACT
Dicer
[Dcr-2]
(f)
Ago1-4
Dicer
[Dcr-1]
TRBP
PACT
(g)
(g)
(h)
Ago1-4
[Ago2]
TRBP
[R2D2]
Dicer
[Dcr-2]
(i)
Ago1-4
[Ago1]
TRBP
Dicer
[Dcr-1]
(j)
Ago2
[Ago1, 2]
(k)
Ago1, 3, 4
Unwindase ??
(k)
Unwindase ??
Ago1-4
[Ago1]
(l)
Ago2
[Ago1, 2]
(l)
Ago1-4
[Ago1]
(o)
AAAAAAAA
Ago1-4
[Ago1]
GW182
m7G
Ribosome
(m)
AAAAAAAA
Ago2
[Ago1, 2]
m7G
(p)
Ago1-4
[Ago1]
CCR4:NOT
AAAAAAAA
GW182
DCP1:DCP2
P-Body
m7G
(n)
AAAAAAAA
XRN1
m7G
Exosome

4.2 Biogenesis of Small RNAs

There are many different types of short RNAs, e.g. siRNAs, miRNAs, piRNAs etc. They differ in their origin, their maturation pathways and in their mode of gene regulation inside cells. The best characterized small double stranded RNA silencing triggers are siRNAs and miRNAs. Therefore, this chapter focusses an these two. siRNAs derive from long double stranded RNAs, have nearly perfect complementarity to their target, are loaded in the RNA-induced silencing complex (RISC), and induce cleaveage of the targeted mRNA. This mechanism called RNAi is conserved among eucaryotes, because it is a powerful immune response against viral infections and protects the genome against transposons. In contrast miRNAs are endogenous short single stranded RNAs that form hairpin like structures which contain mismatches and bulges. They are found in algae, plants, protists, animals, and viruses [179, 180]. miRNAs are involved in temporal and spatial development, in tissue maintenance [181], and regulate gene expression by repression of translation and mRNA degradation. The following chapter will focus on the origin, maturation and effector step of short RNAs in animals, especially in mammals (mainly humans) and flies (Drosophila melanogaster).

4.2.1 Origin of Long dsRNAs

siRNAs are produced from long double stranded RNAs, which can be of endogenous or exogenous origin. Endogenous dsRNAs in mammals were only found in gonads and early embryos, where they derive from transposons [182–184] (Fig. 4.1(a)). In contrast in flies endogenous dsRNAs were found in gonads and soma, where they also originate from heterochromatic regions [185–189].

Exogenous dsRNAs are either of synthetic origin or are the natural replication products of viruses, as has been shwon in flies [190–192].

4.2.2 Nuclear Maturation of micro RNAs

The precursors of miRNAs originate in the nucleus, where the production and first maturation step takes place. The primary transcript of miRNA genes is a capped and polyadenylated mRNA that folds into clearly defined local hairpin structures [193–195]. These, so called primary miRNAs (pri-miRNAs) are transcribed from

Figure 4.1 ***(facing page)*****:** Origin, maturation and effector steps of siRNAs and miRNAs in human. Differences of the short RNA maturation in flies from the human system are indicated in square brackets. A detailed description of the various RNAi processing and activity steps can be found in sections 4.2 and 4.3. The symbols for Dicer and Ago are inspired from the structure and function of these proteins described in [176–178].

miRNA genes by polymerase II in a highly tissue specific manner [196–198], although a minor group of miRNAs associated with Alu-repeats is transcribed by polymerase III [199]. The hairpin structures contain a highly conserved double-stranded stem, which is 30 base pairs (bp) long (Fig. 4.1(b)) [200–202].

pri-miRNAs are processed to precursor miRNAs (pre-miRNAs) by the so called microprocessor complex (Fig. 4.1(b)) [203, 204]. The microprocessor complex consists of the RNase III class II protein Drosha and DGCR8 (in flies called Pasha) [205–208]. DGCR8 binds the single-stranded double-stranded junction of the pri-miRNA with its two dsRNA binding domains (dsRBDs) [206, 207, 209] and directs Drosha to its cleavage site 11 nt (one helical turn) away from the junction on the double-stranded stem [210]. The two RNase III domains of Drosha form an intramolecular dimer with two active sites forming one processing center. The RNase III domain A cleaves the 3' strand, leaving the 3' end of the pre-miRNA with a 2 nt overhang and a hydroxyl group, while the RNase III domain B cleaves the 5' strand, leaving a monophosphate [204, 207]. The microprocessor complex discriminates its substrate from other secondary mRNA structures by the length of the double stranded stem and the number and size of the contained bulges [211], it was proposed that DGCR8 performs this discrimination, because its two dsRBDs form a structure which binds al 33 bp long double-stranded stem [209, 212].

A Drosha independent pre-miRNA maturation pathway, called the mirtron pathway was found in 2007. The intron encoded pre-miRNA is directly cut out by the Spliceosome, leading to a branched pre-mirtron which is the excised intron. This pre-mirtron is then debranched and sometimes trimmed by exonucleases to form a pre-miRNA (Fig. 4.1(c)) [213–215].

All the different pathways produce pre-miRNAs having a double-stranded stem around 20 nt long, containing the miRNA and a terminal loop. The 3' end has a 2 nt long overhang with a hydroxyl group and the 5' end contains a monophosphate. For the next maturation step these pre-miRNAs have to be exported to the cytoplasm, what is performed by Exportin5/RanGTP (Fig. 4.1(d)). Exportin5/RanGTP binds all dsRNAs with a stem longer than 14 bp and having 3' overhangs or blunt ends. They are transported through the nuclear envelope, where the GTP is hydrolyzed and the short RNA is released into the cytoplasm [216–219].

4.2.3 Small RNA Processing in the Cytoplasm

The production of short RNA duplexes, which can be loaded in the Ago proteins, is performed by Dicer in the cytoplasm. Dicer is a RNase III class III protein [220] which is highly conserved among eucaryotes. Dicer cleaves dsRNAs and pre-miRNAs 21-23 nt away from the terminus, leaving a 2 nt long overhang and a hydroxyl group at the 3' end and a monophosphate at the 5' end [166, 221] (Fig. 4.1(e,f)). The cleavage reaction depends on Mg^{2+} ions, and is in most cases ATP

independent [221, 222]. The association of Dicer with its substrates relies on Dicers dsRBD and PAZ domain. The PAZ domain binds the terminus of the dsRNA or pre-miRNA, preferential a terminus with a 2 nt long 3' overhang [223–227]. The PAZ, the DUF283, and a part of the RNase III domain A form the internal ruler for the cleavage after ∼22 nt. As in Drosha the RNase III domains form an internal dimer, containing one processing center with two active sites. RNase III domain A cleaves the 3' strand leaving a hydroxyl group and a 2 nt long overhang, while domain B cleaves the 5' strand leaving a monophosphate [176, 177, 228]. Recombinant Dicer can produce short RNA duplexes alone [222, 229, 230], but is normally found together with dsRNA-binding proteins *in vivo*.

In humans only one Dicer protein exists. It associates with the dsRNA-binding proteins TRBP [229, 231] and PACT [230] to process dsRNA into siRNAs (Fig. 4.1(e)). Both proteins increase the activity of Dicer [232] by the reduction of autoinhibition by Dicers helicase domain [233]. Human pre-miRNAs are processed to miRNA duplexes by the RISC loading complex (RLC), composed of Dicer, TRBP, PACT, and one of the four human Ago proteins (Fig. 4.1(f)) [230, 234–236]. This complex also loads the miRNA into RISC (see section 4.2.4).

In contrast to humans two Dicer proteins exist in flies which have distinct roles. A complex of Dicer-1 and the PB-isoform of the dsRNA-binding protein Loquacious (LOQS-PB), also known as R3D1, process pre-miRNAs into miRNA duplexes (Fig. 4.1(f)) [237–240]. Dicer-1 is very similar to human Dicer and does not need ATP for its activity. LOQS-PB activates the pre-miRNA processing of Dicer-1 and restrains Dicer-1 from dsRNA processing [241]. The second dicer of flies, Dicer-2 processes in a complex with the PD-isoform of Loquacious (LOQS-PD) [240, 242] dsRNA into siRNAs in an ATP dependent manner (Fig. 4.1(e)) [243, 244]. Dicer-2 contains instead of a PAZ domain a DExH domain.

4.2.4 RISC Loading and Passenger Strand Separation

For the generation of a fully functional RISC, the siRNA and miRNA duplexes have to be loaded in the Ago proteins. The loading is performed by the RISC loading complex (RLC) which binds the duplexes and senses the hybridization energy of the first four nucleotides from each terminus (Fig. 4.1(h,i)). The RLC can differentiate between hybridization energies that differ only by 0.5 kcal/mol. The strand with the less tightly bound 5' end is loaded into the Ago protein, and therefore becomes the guide strand [245, 246]. The cleavage competent Ago2 proteins in flies and humans, cleave the passenger strand of siRNAs [247–250], accelerating the release of the passenger strand from Ago2 (Fig. 4.1(j)). In flies the activation of RISC is accelerated by the endonuclease C3PO which removes the cleavage products [251]. For miRNAs and the other cleavage incompetent Ago proteins a bypass mechanism is proposed (Fig. 4.1(k)) [248], which does not need ATP [235, 252]. A potential protein for the unwinding of the passenger strand

in the bypass mechanism, was found in RNA Helicase A [253]. In all cases the passenger strand is released from the Ago protein and degraded in the cytoplasm.

Due to the different number of Dicer and Ago proteins in humans and flies, the loading mechanism differs between them in detail. In flies siRNAs and miRNAs are released from the Dicer proteins after cleavage (Fig. 4.1(g)) and are rebound by the different RISC loading complexes [254] which facilitate the loading into different Ago proteins [255]. The interaction of the two Dicer proteins with the short RNA duplexes depend on the number of mismatches and bulges inside the duplex. While Dicer-1 and Dicer-2/R2D2 compete for short RNA duplexes, which contain only some mismatches [256], Dicer-2/R2D2 refuses miRNAs, especially these with mismatches in the cleavage region [257] and binds perfectly complementary siRNAs [243, 256, 258]. The dsRNA binding protein R2D2 interacts with the tighter bound 5' end and senses thereby the 5' monophosphate of the passenger strand end, while Dicer-2 interacts with the other end. The R2D2/Dicer-2 complex loads the siRNA duplex into Ago2 (see Fig. 4.1(h)) [259–263]. Dicer-1 interacts with all short RNAs and tries to load them into Ago1. Perfectly complementary siRNAs are rejected by Ago1, so that only miRNAs are loaded into Ago1 (Fig. 4.1(i)) [241, 256]. The loading of miRNA-duplexes into Ago1 is an ATP dependent process, while the following unwinding and passenger strand release is ATP independent and facilitated by mismatches outside the cleavage region of the miRNA-duplex [257].

In humans siRNAs and miRNAs are loaded to the same extend to all four Ago proteins [264–267] by the RLC. As for Drosophila Ago1 all four human Ago Proteins prefer short RNA duplexes with mismatches in the central region. The loading of short RNA duplexes in to the Ago protein is ATP dependent, while the following unwinding is ATP independent and is facilitated by mismatches outside the cleavage region (Fig. 4.1(i)). Only the cleavage competent human Ago2 can unwind perfectly complementary siRNAs, by cleaving the passenger strand (Fig. 4.1(h)) [252].

Earlier publications [234–236, 268] found that the minimal human RLC is composed of Dicer, TRBP and one of the four Ago proteins and that the loading of siRNAs is ten times less efficient than the loading of pre-miRNAs. A very recent publication [252], showed that in cell lysate the loading efficiency is equal for siRNAs, miRNAs, and pre-miRNAs, suggesting that the before found minimal RLC is not the canonical RLC, but reflects a complex which performs bypass incorporation of single-stranded forms of small RNA duplexes and hairpin RNAs [229, 252, 269].

From crystal structures the picture evolves that the short RNA is first bound to the PAZ domain of Ago [226, 227, 270, 271]. Due to conformational changes the first 5' basepair of the guide strand is opened, and this guide strand end is inserted into the 5' binding pocket. There the 5' phosphate is bound by a Mg^{2+} ion. The first five 5' terminal nucleotides of the guide strand interact with the conserved

region around the binding pocket in a sequence independent way [178, 271–274].

4.3 Gene Regulation by Small RNAs

The maturation steps of small RNAs described in the previous sections, create an active RNA-induced silencing complex (RISC). RISC is a big cellular complex which consists of many different proteins [275]. The core protein of all RISCs is an Ago protein [255, 276–278], which is loaded with a single stranded short RNA [269, 277, 279] (see Fig. 4.1(l)). To regulate the expression of genes, the active RISC interacts with mRNAs. If the mRNA contains a complementary sequence to the Ago loaded single stranded RNA, both RNAs hybridize. In dependence of the RISC composition, the Ago protein will then regulate the gene expression by either mRNA cleavage, translational repression, or mRNA degradation. Due to the separation of transcription and translation in the nucleus and cytoplasm, respectively, transcriptional gene silencing is a nuclear process and translational repression a cytoplasmic process. The cleavage of RNAs was found both in the cytoplasm and in the nucleus [280, 281].

4.3.1 Target Recognition

For the identification of complementary target RNAs, the active, guide strand containing, RISC has to interact with mRNAs. Crystal structures of guide strands bound to Ago and Piwi proteins show that the first ten nucleotides of the 5'-end form an A-helix [271, 273, 274]. The nucleotides 2 to 8 are exposed to the solvent, thereby forming the primary pairing region, called the seed region. To find the complementary site on the targeted RNA, RISC does not scan the targeted RNA unidirectional [282, 283], but interacts in a nonspecific way with single stranded RNA to promote the sequence specific pairing of the seed region with the targeted RNA [284]. The complete process of target recognition is accelerated nine times by RISC, compared to the pairing of guide strand to its targeted mRNA without RISC [284]. Target recognition by RISC is ATP independent [285], and active translation of the targeted mRNA is not necessary [282, 283]. A stable pairing of the seed region induces translational repression (see section 4.3.3) [286, 287]. Incase of fully complementary strands, hybridization propagates to the 3' end, while the Ago protein undergoes big conformational changes [288–290], and the 3'end of the guide strand is released from the PAZ domain [291].

Target recognition and thereby also the later effector step depends strongly on the secondary structure of the targeted mRNA at the complementary site. Hairpin structures, where the targeted site forms a duplex, but also other secondary structures inhibit the binding of active RISC. The higher the number of paired nucleotides of the target sequence, the stronger the inhibition of RISC activity [284, 292–295].

4.3.2 Messenger RNA Cleavage

The cleavage of targeted mRNAs by RISC is the best understood RNA mediated gene regulation process. Ago2 is the only cleavage competent Ago protein found in mammals and flies [249, 265, 266, 296], so only RISC containing Ago2 proteins can perform gene regulation by mRNA cleavage. If the guide strand nearly perfectly matches the target site (at least nucleotides 2-15) and forms at least one complete turn of an A-form double helix, the targeted mRNA will be cleaved by Ago2 independent from the maturation pathway of the guide strand (Fig. 4.1(m)) [278, 297–299]. siRNAs which derive from dsRNAs, show normally such a high complementarity to their target sites, but also some miRNAs have enough complementarity to mediate cleavage of their targets [300, 301]. The targeted mRNA is cleaved between the bases which pair the 10th and 11th nucleotide of the guide strand, counted from the 5' end [299, 302]. This cleavage position is given by the Ago internal distance between the 5' binding pocket and the catalytic site [272, 290]. The catalytic site is located in the Piwi-domain, resembles a RNase H domain [303] and is a Asp-Asp-His (DDH) motif [269]. The cleavage reaction is an ATP-independent hydrolysis, leaving a 3' hydroxyl group and a 5' phosphate terminus [285, 304], catalyzed by two Mg^{2+} ions [305, 306]. The cleavage competent RISC is a true multiple turnover enzyme, which can catalyze several rounds of target-RNA cleavage [278, 299]. After cleavage the products are released and rapidly degraded by exonucleases [279]. The 5' cleavage product is degraded from its 3' end by the Exosome, which needs the Ski-complex to bind the RNA. While the 3' cleavage product is degraded from its 5' end by XRN1 (Fig. 4.1(n)) [307, 308].

RNA cleavage is sequence specific down to one nucleotide in the region around the cleavage site (nucleotides 9-12) [302, 309]. Mismatches and bulges are well tolerated at the 3' end of the guide strand [298, 310], while the limited space in the region of the Ago protein that anchors the seed region, allows only very few mismatches in the pairing of the seed region [290].

siRNAs can have off-target silencing effects. The short length of only 8 nt, makes the seed region relative unspecific. Thereby pairing with sequences similar to the targeted RNA can trigger RISC mediated gene silencing, causing off-target silencing effects [311–314].

4.3.3 Translational Repression and mRNA Degradation

The huge majority of the over 800 known miRNAs mediate translational repression and mRNA degradation. Both are summarized under the name miRNA-mediated gene silencing [315–317]. miRNA-mediated gene silencing is the second gene regulation mechanism of RISC and plays a great role in temporal and spatial development and in tissue maintenance [181]. The human genome contains more

than 45000 conserved miRNA target sites, covering 60 % of all human gene coding sequences [173–175].

In humans all four Ago proteins can induce miRNA-mediated gene silencing [265, 278, 318, 319]. The miRNA loaded RISC is bigger than 900 kDa and contains many different proteins [275]. The best studied accompanying protein is GW182, also known as TNRC6 [234, 267, 275]. GW182 contains a GW/WG rich region, called the Ago-hook, which interacts with the 5' binding pocket of Ago, without disturbing the binding of the miRNA 5' end [320, 321], and thereby strongly increases miRNA-mediated gene silencing [320, 322, 323].

In flies, miRNAs are mainly loaded into Ago1 [255], therefore Ago1 containing RISC is the major miRNA-mediated gene silencing complex in this organism. In case of highly complementary miRNAs and endogenous siRNAs, which are not full complementary to their target RNA, also Ago2 can induce miRNA-mediated gene silencing [188, 324]. As in humans GW182 plays an essential role, and the miRNA-loaded RISC contains many more proteins [308, 323].

The inhibition of mRNA cleavage by mismatches between the guide strand and the targeted mRNA causes miRNA-mediated gene silencing, independent from the biogenesis of the loaded short RNA [297, 325]. miRNA target sites are normally found in the 3' untranslated region (UTR) of the targeted mRNA [204, 326–328], although it has been shown that target sites in the 5' UTR and even the coding region exists and exhibit silencing and repression activity [287]. The number of miRNA-target sites, regulate the strength of gene silencing. One target site is not enough to induce measurable silencing efficiencies, for example the let-7 targeted lin-41 mRNA contains two target sites, which are both necessary for gene silencing [287]. The effect of more target sites seems to be more than additive, four binding sites silence the gene four times stronger than two binding sites [325].

To perform miRNA-mediated gene silencing the miRNA-loaded RISC forms a stable association with the targeted RNA [267, 329–331]. In huge proteomic screens and also in other experiments it was seen that there are two different mechanisms for miRNA-mediated gene silencing - translational repression and mRNA degradation [332–335]. Both mechanisms are independent, but influence each other *in vivo* [335] and are described in the following sections.

Translational Repression

Translational repression describes a mechanism, where miRNA-loaded RISC inhibits the translation of the mRNA into a protein, without changing the level of the mRNAs inside the cell (Fig. 4.1(o)). It is independent from the key mechanisms of mRNA degradation - deadenylation and decapping [335–337] and functions also in the absence of processing bodies (P-bodies) [332]. The achieved gene silencing by repression of translation is only modest [333, 334].

There are two mechanisms for translational repression of miRNA-loaded RISC

[338]. The earlier found mechanism is the inhibition of translation elongation, where the production of the peptide is stalled somewhere after the initiation process of translation [339, 340]. This mechanism is supported by the fact that most miRNAs were found on actively translated mRNAs [341, 342]. In the second mechanism translation is repressed, by the inhibition of translation initiation [343]. In this mechanism RISC interacts with the cap structure of the targeted mRNA [323, 344] and interferes with the binding of translation initiation factors, because mRNAs lacking the m^7GpppG cap [345–347] and mRNAs bound to the translation initiation factors eIF4E and eIF4G [348] could not be repressed.

In flies it was recently shown that Ago1 containing RISC blocks a step after cap recognition, while Ago2 binds to eIF4E and blocks the eIF4E-eIF4G interaction, which points to the fact that the mechanism of translation repression can also depend on the Ago protein [324].

In at least one case it was shown that miRNA-repressed mRNAs were released from translational repression and entered again the translation machinery under changing environmental conditions [349].

mRNA Degradation

The second mechanism of miRNA-mediated gene silencing is mRNA degradation. It is involved in the silencing of all genes, which show a silencing of more than 3-fold, for highly repressed genes mRNA degradation is the major silencing mechanism [333]. In flies 60 % of all miRNA-targeted mRNAs are degraded [335].

The miRNA-mediated mRNA degradation takes place in so called processing bodies (P-bodies) (Fig. 4.1(p)). P-bodies are cellular organelles, where the complete mRNA dergradation, also the miRNA independent one, takes place [350]. Many proteins involved in mRNA degradation are found in P-bodies [351, 352], including the proteins that are involved in miRNA-mediated gene silencing, for example all four human Ago proteins [348, 353, 354] and GW182 [234, 308, 322, 355].

In flies only Ago1 containing RISC can trigger mRNA degradation in P-bodies, but not Ago2 containing RISC [324].

miRNA targeted mRNAs can localize to P-bodies in the presence of the miRNA together with the complete RISC (Fig. 4.1(o)). There the targeted mRNAs are stored and degraded. The degradation starts with deadenylation of the poly(A)-tail by the CCR4:NOT complex, with the deadenylases CAF1 and NOT1 [320, 335, 336] and is followed by decapping, which is executed by the decapping complex Dcp1:Dcp2 [320, 335, 337, 353]. After decapping the mRNA is degraded in a 5' to 3' manner by XRN1 [335, 351, 356].

In yeast miRNA targeted mRNAs shuttle between P-bodies (translation repression) and polysomes (active translation) in a cell state and cell stress dependent manner [357].

4.3.4 Transcriptional Gene Silencing

The third major gene silencing mechanism, is transcriptional gene silencing (TGS) (reviewed in [358, 359]). In contrast to mRNA cleavage, translational repression and miRNA-mediated mRNA degradation, which function post-transcriptional, TGS directly interferes with the transcription of a gene, and is therefore a nuclear process. TGS is induced by perfectly or imperfectly matching short RNAs which are complementary to the promoter sequence or the transcription start site sequence of the targeted gene [360–362]. These RNAs are called antigene RNAs (agRNAs), and the involved protein complex is called RNA-induced transcriptional silencing complex (RITS). In humans Ago1 and Ago2 loaded with an agRNA together with TRBP associate with the actively transcribed promoter site [363, 364] and interact directly with the actively transcribing Polymerase II [364, 365]. The agRNA guide strand hybridizes with the promoter sequence on an extended 5' UTR in the transcript and not on the template [360, 361]. RITS initiates then DNA- and/or Histone methylation. For DNA-methylation the DNA methyltransferase DNMT3a is activated by RITS and methylates CG dinucleotides [365, 366]. In Histone methylation, the Histone methyltransferase EZH2 performs Histone H3 lysine-9 di-methylation (H3K9) and Histone H3 lysine-27 tri-methylation (H3K27), which were found up to 720 bp downstream from the promoter sequence [364, 365]. Histone methylation can lead to the formation of heterochromatin.

4.4 Chemical Modifications

The wide usage of RNAi in reverse genetics and its growing usage as a therapeutic reagent is based on the following advantages of this technique. RNAi is highly specific, siRNAs as reagents are easily available and simply to design. The knowledge of an organisms genomic sequence permits rapid design and a genome-wide coverage. The disadvantages of RNAi are the relatively short lifetime of the silencing trigger, the dependency on the protein half-life due to targeting of the mRNA and the different delivery efficiencies among different tissues [368].

Nearly from the discovery of RNAi in mammalian cells [167] on, chemical modifications of siRNAs were studied to overcome these disadvantages. Many of these chemical modifications are well known from antisense drug research, a technology where single stranded antisense oligonucleotides are used to interfere with mRNA expression. The numerousness number of possible modifications [369, 370] can be classified in modifications of the phosphate backbone, modifications of the ribose and modifications of the nucleic base. Here the focus will be on four chemical modifications of RNA which have been already intensively studied to characterize their usefullness for RNAi based therapeutics. The chemical structure and the intracellular localization of these chemical modified siRNAs is shown in Fig. 4.2.

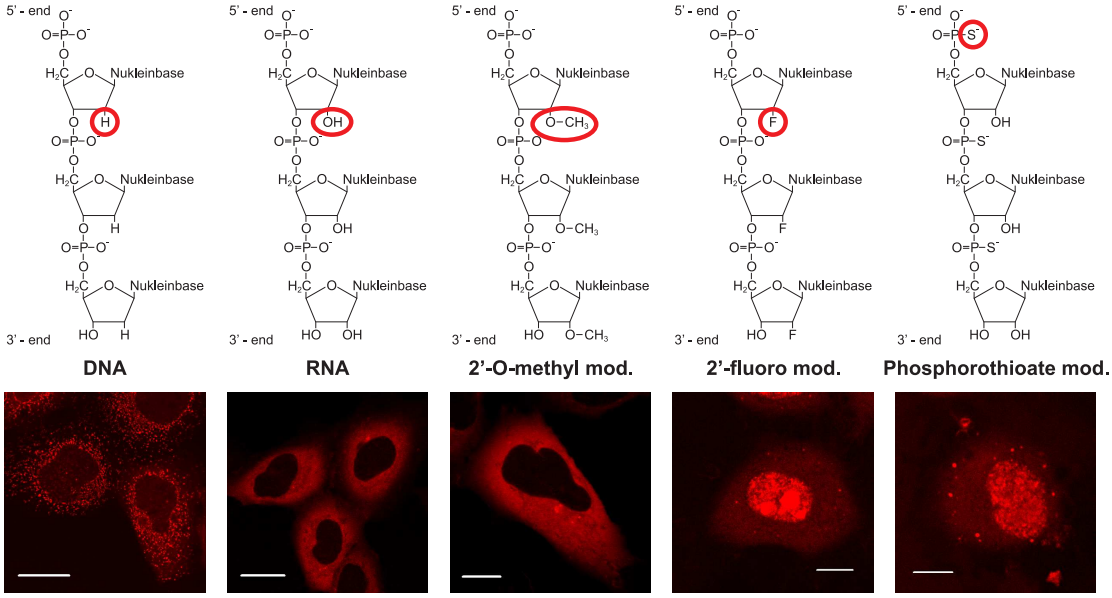

Figure 4.2: Chemical modifications and their intracellular localization: The upper row shows the chemical formulas of DNA, RNA, 2'-O-methyl modified RNA, 2'-fluoro modified RNA and phosphorothioate modified RNA (from left to right), and the lower row shows the respective intracellular localization patterns of short (21 nt) double stranded DNA/RNAs with 2 nt 3' overhang [367].

The replacement of RNA nucleotides with DNA nucleotides is known from the early beginning of siRNA usage [302] (Fig. 4.2). For a long time, they were used to replace the two 3' terminal nucleotides which form the overhang. The replacement of a complete siRNA strand with a complementary DNA strand abolished silencing activity [302]. A recent study shows that more nucleotides than the terminal ones can be replaced, without the loss of silencing activity. It is possible to replace the complete seed sequence of the guide strand, remaining the full silencing activity and additionally suppressing off-target silencing [371].

The substitution of the hydroxyl group at the second position of the ribose ring with a methylated oxygen is called the 2'-O-methyl modification (Fig. 4.2). It is like DNA a natural occurring modification known from transfer and ribosomal RNAs and also the 3' terminal nucleotide of Piwi-interacting RNAs (piRNAs) is 2'-O-methyl modified [372–375]. The dominantly cytoplasmic localization of 2'-O-methyl modified siRNAs is the same as for unmodified siRNAs (Fig. 4.2) [367].

Several studies show that 2'-O-methyl modifications of up to four consecutive nucleotides per strand at several positions are well tolerated. Longer consecutive 2'-O-methyl modifications decrease silencing activity [376–378]. Modifications on

the passenger strand are more tolerated than on the guide strand. siRNAs with completely 2'-O-methyl modified passenger strands were found, which show normal silencing activity [378, 379]. siRNAs with every second nucleotide modified, or with completely modified passenger strand show strongly increased serum stability combined with normal silencing activity [310, 378, 380]. In one case for a siRNA with every odd nucleotide 2'-O-methyl and every even 2'-fluoro modified a 500-fold increase in silencing activity was observed [380].

Completely 2'-O-methyl modified oligonucleotides bind to RISC loaded with a complementary guide strand and inhibit target mRNA cleavage and miRNA-mediated gene silencing [381, 382].

The 2'-O-methyl modification of the second guide strand nucleotide from the 5' end strongly reduce off-target silencing, probably due to weakening the pairing with targeted mRNA, and thereby reducing the binding to not perfect complementary targets [383]. On siRNAs missing the 5' phosphate, the 2'-O-methyl modification prevents the phosphorylation. Therefore, the 2'-O-methyl modification of the first sense strand nucleotide can be used to reduce the loading of the sense strand and to favor the loading of the antisense strand [384].

In 2'-fluoro modified RNA the hydroxyl group at the second position of the ribose is replaced by a fluorine (Fig. 4.2). 2'-fluoro modification show a strong nuclear localization, with a slight localization in P-bodies, in contrast to the 2'-O-methyl modification [367]. The 2'-fluoro modification of several single nucleotides and up to three consecutive nucleotides has nearly no negative effect on the silencing activity and in some cases increased the serum stability of the siRNA and the persistence of RNAi [298, 377, 378, 385–387].

The substitution of an oxygen in the phosphate backbone by a sulfur is called phosphorothioate modification. As for the 2'-fluoro modification also for the phosphorothioate modification a strong accumulation of the modified siRNAs in the nucleus is noted (Fig. 4.2) [367, 385]. The modification of several single nucleotides and up to four consecutive nucleotides does not interfere with silencing. For longer modifications typically a decrease in silencing activity is observed [376, 378, 385, 386]. The complete phosphorothioate modification of the antisense strand strongly reduced or abolished silencing, while the complete sense strand modification was tolerated [377, 379, 385]. In some studies cytotoxicity of longer phosphorothioate modification was observed [376, 386].

Bigger modifications on the termini of the siRNA strands, like the attachment of biotin or fluorophores are tolerated on both 3' termini and the 5' terminus of the sense strand, but not on the 5' terminus of the antisense strand [310, 388, 389].

5 RNAi Mechanism studied by FCCS *in vivo*

5.1 Introduction

Short interfering RNAs (siRNAs) are the effector molecules of an evolutionary conserved gene silencing mechanism called RNA interference (RNAi) [165–167]. These usually 21 nt long double stranded RNA molecules are loaded into the RNA-induced silencing complex (RISC), which contains an Argonaute protein. During the loading mechanism, the selection of the later called guide strand is governed by the thermodynamic stability of the duplex termini and stays in the now activated RISC [245, 246]. The recognition of targeted mRNAs by RISC is guided by the single stranded RNA on the basis of sequence complementarity. In case of nearly perfect complementarity between the guide strand and the targeted mRNA, RISC cleaves the mRNA, which gets subsequently degraded by exonucleases [266, 279, 302]. A detailed description of the complete RNAi mechanism can be found in chapter 4.

The identification of siRNAs as triggers of RNAi in mammalian cells [167] yielded in the development of chemically synthesized siRNAs. The specificity and simplicity of RNAi opened the wide field of therapeutic usage to siRNAs [390–392]. To improve the pharmacokinetic and pharmacodynamic[1] properties of siRNAs various modifications, e.g. the phosphorothioate backbone modification, 2'-O-methyl and 2'-fluoro sugar modification, have been comprehensively evaluated. These modifications and their effects in RNAi can be found in section 4.4.

So far, the effects of chemical modifications on siRNA mediated silencing have been studied by classical silencing readouts either by targeting an endogenous gene analyzed by western blot, qRT-PCR or by standard reporter assays, e.g. mRFP/ EGFP expression or the dual luciferase assay [298, 310, 367, 376, 377, 385]. Little is known about the mechanism of silencing inhibition by modified nucleotides which can e.g. affect affinity to RISC, strand separation, cleavage activity and/or the stability of the incorporated guide strand. In addition, the direct analysis of the RNAi mechanism in vivo in real time at the early phase of RISC activation (1-6 h) can result in a more detailed characterization of modified siRNAs, needed to further improve RNAi-based pharmaceuticals.

Here, dual-color fluorescence cross-correlation spectroscopy (FCCS) was used to directly access strand separation, guide strand incorporation and the duration of incorporation as well as RISC-target-RNA interaction *in vivo*. In contrast to the

[1] Pharmacodynamics explores what the drug does to the body, while pharmacokinetics explores what the body does to the drug.

classical silencing readouts, the high sensitivity of FCCS allowed the localization of individual steps of silencing inhibition, without the use of reporter systems or the requirement of translational regulation or knock down of mRNA or protein. The positional effects of the chemical modifications were characterized with high sensitivity in different cellular compartments in real time.

5.2 Material and Methods

Cell Culture

ER293 cells stably transfected with the pERV3 vector (Stratagene) were cultured at 37°C in DMEM (high glucose, Sigma) with 10% FBS (PAA Laboratories GmbH), 2 mM glutamine (Gibco), and 0.3 mg/ml G418 (50 mg/ml, Gibco). The stably expressing EGFP-Argonaute2 cell line 10G was generated by Thomas Ohrt (details can be found in [368]) and cultured at 7°C in DMEM (high glucose, Sigma) with 10% FBS, 2 mM glutamine, 0.3 mg/ml G418, and 0.4 mg/ml Hygromycin B. All cells were regularly passaged at subconfluency and were plated with 1-5 $\cdot 10^4$ cells/ml density.

Target and siRNA Sequences

All RNA strands were obtained from IBA GmbH (Goettingen) as single strands with 5'-phosphate, a 3'-amino group and labeled with Cy5 succinimidyl ester (Cy5-NHS, Amersham Biosciences) on the first nucleotide from the 3' end. Duplex siRNAs were prepared by mixing complementary sense siRNA and antisense siRNA at equimolar ratio, incubating at 80°C for 2 min followed by a cooling step at 1°C/min to 15°C. The annealing procedure was performed in the Mastercycler epGradientS (Eppendorf) in 110 mM K-gluconate, 18 mM NaCl, 10 mM HEPES, pH 7.4, and 0.6 mM MgSO4 with 10–60 mM siRNA concentrations. The quality of the duplex siRNAs was checked by agarose gel electrophoresis and high-performance liquid chromatography. The prepared siRNA duplexes were stored at -20°C.

Target-RNA sequence is derived from the pRL-TK vector (Promega) containing the target sequence for siTK3: CCA GAA GAA UUU GCA GCA UAU CUU GAA CCA UUC AAA GAG AAA GGU GAA GU, 2'-O-methyl modifications at positions 1-7 and 44-50 and Cy5 at the 3' end.

The siTK3 siRNAs were ordered with 2'-O-methyl modifications at several different positions, at least including the first four nucleotides from the 3' end.

antisense siTK3:	UGA AUG GUU CAA GAU AUG CUG
sense siTK3:	GCA UAU CUU GAA CCA UUC AUU
antisense siTK3-bulge:	UGA AUG GUC AUA GAU AUG CUG
sense siTK3-bulge:	GCA UAU CUA UGA CCA UUC AUU

For luciferase experiments SilencerTM Negative control #2 (NegsiRNA) from Ambion was used.

Luciferase Assay

Dual-luciferase assays (Promega GmbH) were performed 24-48 h after transfection according to the manufacturer's protocol for 24-well chambers and detected with a TD20/20 luminometer (Turner designs). Pp-luc target vector (pGL2-Control, Promega) was co-transfected with the control vector Rr-luc (pRL-TK, Promega GmbH). Lipofectamine 2000 (Invitrogen GmbH) was used for the triple transfection of the dual luciferase assay vectors pGL2-control (contains the cDNA of Firefly luciferase (FL)) and pRL-TK (contains the cDNA of Renilla luciferase (RL)) together with the siRNAs. The desired amount of each siRNA was mixed with 0.9 µg pGL2-control and 0.1 µg pRL-TK. The cells were transfected with the indicated amounts of siRNAs, 100 µl Opti-MEM, and 2 µl Lipofectamine 2000. 3-5 h after transfection the medium was replaced by 500 µl fresh growth medium.

The ratios of target (pRL-TK) to control (pGL2-control) luciferase concentrations were normalized to the NegsiRNA control.

Target-RNA Stability Assay

To test the target-RNA stability, double-labeled target-RNA (3'end-Alexa488, 5'end-Cy5) was incubated for several incubation times between 0 and 180 min in HeLa S20 extract at 37°C. To stop the degradation aliquots were stored on ice. Analysis of target-RNA after incubation was done by denaturing polyacrylamide gel electrophoresis (PAGE), containing urea and 18% polyacrylamide. The amount of intact target-RNA was quantified by measuring the mean intensity of the yellow band, containing both labels.

Microinjection

For the loading assay, 5-10 $\cdot 10^4$ 10G cells were transferred onto MatTek chambers coated with Fibronectin (25 µg/ml in PBS including $CaCl_2$ and $MgCl_2$, Roche) 24 h before microinjection. Immediately before microinjection the growth medium in the MaTek chamber was replaced by microinjection buffer (150 mM NaCl, 20 mM HEPES pH 7.4, 15 mM Glucose, 150 µg/ml BSA, 20 mM Trehalose, 5.4 mM KCl, 0.85 mM $MgSO_4$, 0.45 mM $CaCl_2$). The micropipette (Femtotip 2, Eppendorf) is loaded with 1.5-4 µM labeled siRNAs in 110 mM K-gluconate; 18 mM NaCl; 10 mM HEPES pH 7.4 and 0.6 mM $MgSO_4$. The micromanipulator consists of a FemtoJet and InjectMan NI2 which is mounted directly on a microscope. Working pressure for injection was between 20-40 hPa for 0.1 s and a holding pressure of 15 hPa. siRNAs were allways injected into the cytoplasm.

After microinjection the mircoinjection buffer was replaced with growth medium again and cells were put back into an incubator for different times.

For target-interaction assay, $18 \cdot 10^4$ 10G cells were transferred onto a Fibronectin coated MatTek chamber. For transfection with unlabeled siRNAs, 9 µl of the indicated siRNA (concentration 20 µM), together with 4 µl Lipofectamin 2000 and 300 µl Opti-MEM were added to cells covered with 1.5 ml growth medium. 3 h after transfection the medium was replaced by 2 ml fresh growth medium.

Between 10 and 18 h after transfection the labeled target-RNA was microinjected with the same procedure as for the labeled siRNAs, but instead of labeled siRNAs 1.5-4 µM labeled target-RNA in 110 mM K-gluconate; 18 mM NaCl; 10 mM HEPES pH 7.4 and 0.6 mM $MgSO_4$ was used.

FCCS Data Acquisition

For the FCCS measurements the growth medium was replaced by air buffer (150 mM NaCl, 20 mM HEPES pH 7.4, 15 mM Glucose, 150 µg/ml BSA, 20 mM Trehalose, 5.4 mM KCl, 0.85 mM $MgSO_4$, 0.6 mM $CaCl_2$). FCCS was performed on a commercial system consisting of a Confocor 3 attached to a LSM510 (Zeiss, Jena, Germany) at room temperature. The 488 nm Ar-laser-line was used to excite EGFP and the 633 nm line of a HeNe-laser was used to excite Cy5. Both laser lines were attenuated by an acousto-optical tunable filter to 3.5 and 1.05 kW/cm^2, respectively, in order to minimize photobleaching and cellular damage. Both excitation laser lines were directed by a 488/633 dichroic mirror (HFT) onto the back aperture of a Zeiss C-Apochromat 40x, N.A.=1.2, water immersion objective. The fluorescence light was collected by the same objective, separated from the excitation light by a 488/633 dichroic mirror (HFT), passing a confocal pinhole (70 µm in diameter) and split into two spectral channels by a second dichroic beam splitter (LP635). After removing residual laser light by a 505-610 nm bandpass or 655 nm longpass emission filter, respectively, the fluorescence light was recorded by avalanche photodiodes (APDs). Before each experiment the setup was adjusted using Alexa488/Cy5 double labeled siRNA, yielding cross-correlation amplitudes of 75 (±5%). The discrepancy to 100% is due to imperfect overlap of the detection volumes and/or imperfect labeling of the siRNA. In each cell, FCCS was measured in the nucleus and the cytoplasm. For each measurement, 8 runs, each 30 seconds long, were collected. Only cells that exhibited a higher number of red than green fluorophores in the focal volume were used, to avoid that a too low siRNA concentration limits the amount of cross-correlation.

For the localization of the cytoplasm and nucleus a picture of each measured cell was taken by laser scanning microscopy (LSM) using the same instrument, with the same beampath and APDs as detectors.

FCCS Data Analysis

The fluorescence signals of each run were software correlated following the definition of auto- and cross-correlation (see also eq. (2.53)-(2.56))

$$G_{i,j}(\tau) = \frac{\langle \delta F_i(t) \cdot \delta F_j(t+\tau) \rangle}{\langle F_i(t) \rangle \langle F_j(t) \rangle} \,. \tag{5.1}$$

Runs showing significant photobleaching or intracellular movement were discarded from the data evaluation. A model (eq. (5.2)) including two diffusing species and a term accounting for the photophysics (more details in sections 2.3.2 and 2.5) was fitted to the two autocorrelation and the cross-correlation curves, using a weighted Marquardt non-linear least square fitting algorithm (more details in section 2.7). The cross-correlation curve was the average of the two cross-correlation curves (red vs. green and green vs. red channel).

$$\begin{aligned} G_{i,j}(\tau) = G_{i,j}(0) \; & \left(1 + \frac{f_\mathrm{T}}{1-f_\mathrm{T}} \, \exp\left(-\frac{\tau}{\tau_\mathrm{T}} \right) \right) \\ & \cdot \left(\frac{f_1}{\left(1+\frac{\tau}{\tau_1}\right) \sqrt{1+\frac{\tau}{S^2\,\tau_1}}} + \frac{1-f_1}{\left(1+\frac{\tau}{\tau_2}\right) \sqrt{1+\frac{\tau}{S^2\,\tau_2}}} \right) \end{aligned} \tag{5.2}$$

f_T represents the fraction of molecules in the dark state, τ_T the lifetime of the dark state, τ_1 and τ_2 are the diffusion times of the two species, f_1 is the fraction of the first specie and S is the form factor, which is the ratio of axial (z_0) over the radial radius (ω_0). During the fit, the lifetime of the dark state τ_T was fixed to 130 µs and 70 µs for EGFP and Cy5, respectively. These values were determined in preceding experiments with EGFP and Cy5 *in vivo*. The triplet fraction f_T of the cross-correlation curve was fixed to zero. The amplitudes $G_{i,j}(0)$) were corrected for spurious autofluorescent background of the cells, using the mechanism described in section 2.6.3

$$\tilde{G}_{\mathrm{i,j}}(0) = \frac{\langle F_i \rangle}{\langle F_i \rangle - B_i} \, \frac{\langle F_j \rangle}{\langle F_j \rangle - B_j} \, G_{\mathrm{i,j}}(0) \,. \tag{5.3}$$

Here, $\langle F \rangle$ is the measured count rate and B the measured background count rate, which were determined in unlabeled ER293 cells. The background in the green channel was between 5 and 10% of the measured fluorescent signal and for the red channel between 1 and 2%. In addition, background corrected amplitudes $\tilde{G}_{\mathrm{i,j}}(0)$, were corrected for spectral crosstalk. Spectral crosstalk was only encountered from the green into the red channel, with an amount of β=0.7%. Subsequently, the green amplitude is unaffected, while the red and the cross-correlation amplitude need to be corrected for with the mechanism from section 2.6.7. Here $\langle \tilde{F} \rangle$ is the

background corrected count rate $\langle\tilde{F}\rangle = \langle F\rangle - B$

$$\hat{G}_{\mathrm{g}}(\tau) = \tilde{G}_{\mathrm{g}}(\tau) \tag{5.4}$$

$$\hat{G}_{\mathrm{r}}(\tau) = \frac{\langle\tilde{F}_{\mathrm{r}}\rangle^2\,\tilde{G}_{\mathrm{r}}(\tau) + \beta^2\,\langle\tilde{F}_{\mathrm{g}}\rangle^2\,\tilde{G}_{\mathrm{g}}(\tau) - 2\,\beta\langle\tilde{F}_{\mathrm{r}}\rangle\,\langle\tilde{F}_{\mathrm{g}}\rangle\,\tilde{G}_{\mathrm{CC}}(\tau)}{\langle\tilde{F}_{\mathrm{r}} - \beta\,\tilde{F}_{\mathrm{g}}\rangle^2} \tag{5.5}$$

$$\hat{G}_{\mathrm{CC}}(\tau) = \frac{\langle\tilde{F}_{\mathrm{g}}\,\rangle\,\langle\tilde{F}_{\mathrm{r}}\rangle\,\tilde{G}_{\mathrm{CC}}(\tau) - \beta\,\langle\tilde{F}_{\mathrm{g}}\rangle^2\,\tilde{G}_{\mathrm{g}}(\tau)}{\langle\tilde{F}_{\mathrm{g}}(t)\rangle\,\langle\tilde{F}_{\mathrm{r}}\rangle - \beta\,\langle\tilde{F}_{\mathrm{g}}\rangle^2}\,. \tag{5.6}$$

From the corrected amplitudes, the number of fluorescent particles in the detection volume were calculated, which are given by the following set of formulas:

$$\begin{aligned} G_{\mathrm{g}}(0) = \frac{1}{N_{\mathrm{g}} + N_{gr}}\,, \qquad G_{\mathrm{r}}(0) = \frac{1}{N_{\mathrm{r}} + N_{gr}}\,, \\ G_{\mathrm{CC}}(0) = \frac{N_{gr}}{(N_{\mathrm{g}} + N_{gr})\,(N_{\mathrm{r}} + N_{gr})}\,. \end{aligned} \tag{5.7}$$

Here, N_{g} is the number of only green labeled particles, N_{r} the number of only red labeled particles and N_{gr} the number of particles which carry both labels. The amount of cross-correlation was calculated by dividing the number of double labeled particles by all particles carrying a green label

$$\mathrm{CC} = \frac{N_{gr}}{N_{\mathrm{g}} + N_{gr}} = \frac{G_{\mathrm{CC}}(0)}{G_{\mathrm{r}}(0)}\,. \tag{5.8}$$

5.3 RISC Loading and Interaction with Target studied by FCCS *in vivo*

To investigate the influence of chemically modified siRNAs onto the formation and function of RISC, a ER293 based cell line in which hAgo2 is tagged with EGFP was used [368]. hAgo2 was chosen, because it associates with micro RNAs (miRNAs) and siRNAs [266, 267], is involved in nuclear RNAi [280, 281] and shows an endonucleolytical cleavage activity [299, 302]. The characterization of the 10G cell line, stably expressing EGFP-hAgo2, revealed that the fusion protein reproduces the enzymatic activity, sub-cellular localization, expression level and function of endogenous hAgo2 protein [368].

5.3.1 RISC-Loading Studied by Dual-Color FCCS

To study the formation of cleavage active RISC, by asymmetric incorporation of the guide strand and to show the stability of the activated RISC complex, Cy5-labeled siRNAs were microinjected in the 10G cell line and the cross-correlation amplitudes between EGFP-Ago2 and the Cy5-labeled siRNA were measured for

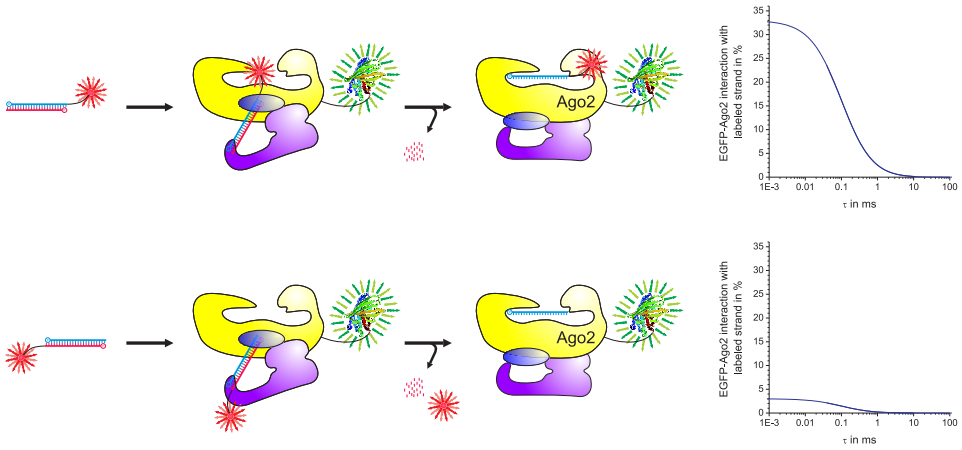

Figure 5.1: FCCS-incorporation assay. FCCS *in vivo* assay to study the asymmetric incorporation of siRNAs into RISC. The incorporation of the labeled strand results in increased cross-correlation amplitudes (upper panel), whereas the incorporation of the non-labeled strand results in low cross-correlation amplitudes (lower panel)

several incubation times. The incorporation of the labeled strand would result in increased cross-correlation amplitudes (Fig. 5.1, upper panel), whereas the incorporation of the non-labeled strand would lead to low cross-correlation amplitudes (Fig. 5.1, lower panel).

The ability of the FCCS-incorporation assay to measure the asymmetric incorporation of the guide strand was proven by measuring the incorporation of the siRNA siTK3, which targets the mRNA of Renilla luciferase encoded on the plasmid pRL-TK. The 5'-end hybridization energies of siTK3 were calculated as described [245] to define the guide and passenger strand (Fig. 5.2(a)). Due to its lower 5'-end hybridization energy, the upper strand in Fig. 5.2(a) forms the guide strand. siTK3 was used, because it displays a high level of Renilla luciferase silencing, demonstrating the incorporation of the guide strand into endogenous RISC (Fig. 5.2(b)). For the *in vivo* experiments, the siRNA was 2'-O-methyl modified at the first four nucleotides from the 3' end to increase the binding stability of the Cy5 label [368]. For comparison the silencing activity of the unmodified siTK3 is also plotted.

After microinjection of siTK3 10G cells display a nearly homogenous distribution of the siRNA in the cytoplasm, with a slight accumulation in P-bodies and an exclusion from the nucleus (Fig. 5.3(a)). The cross-correlation amplitudes measured up to 12 h after microinjection of the passenger strand labeled siTK3 were between 0% and 5% in the cytoplasm and nucleus (Fig. 5.3(c)). This indicates the exclusion of the passenger strand from RISC. In contrast to the low

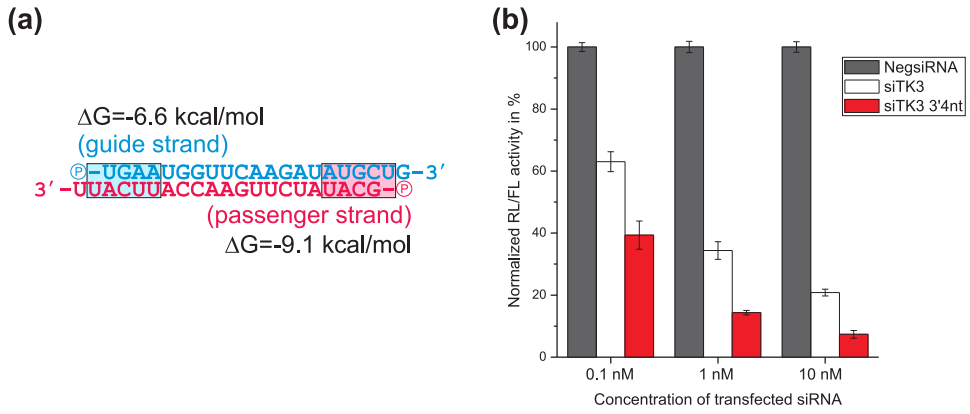

Figure 5.2: Silencing activity of siTK3. (**a**) Sequence and free energies of the siRNA siTK3. (**b**) Silencing activity of indicated amounts of siTK3 (red) and NegsiRNA (black, negative control) measured with a Dual-Luciferase Assay. siRNAs with a 2'-O-methyl modification at the first 4 nucleotides from the 3' ends were used for the *in vivo* experiments. For comparison the silencing activity of unmodified siTK3 is also shown in white (mean of three different experiments ±SD).

cross-correlation levels for the labeled passenger strand, for the guide strand labeled siTK3 the cross-correlation levels increased to a values of 20% and 10% in the cytoplasm and nucleus, respectively. The maximum was reached 6 h after microinjection followed by slight decline (Fig. 5.3(e)). This indicates the incorporation of the labeled guide strand into RISC. Guide strand labeled siRNAs could be observed for longer time periods compared to passenger strand labeled siRNAs, due to the loss of the Cy5 signal in labeled passenger strand containing cells. This most probably results from the stabilization of the guide strand caused by the interaction with RISC, whereas the passenger strand gets degraded.

Control experiments with EGFP supplemented with guide strand labeled siTK3 exhibited no cross-correlation amplitude (Fig. 5.4(a)), whereas a Alexa488 and Cy5 double labeled siRNA as positive control resulted in 75% cross-correlation *in vitro* (Fig. 5.4(b)).

As the relative cross-correlation amplitude is directly proportional to the concentration of the double labeled species (compare eq. (5.8)), these results demonstrate the specific incorporation of the guide strand into nuclear and cytoplasmic RISC, whereas the passenger strand is excluded during the loading process. Interestingly, the cross-correlation amplitudes increase and decline synchronously in the cytoplasm and nucleus, however in the nucleus to a lower extend. There are two obvious reasons that the cross-correlation amplitudes of the labeled guide strand (Fig. 5.3(d)) does not reach the maximal measurable amplitude of 75%

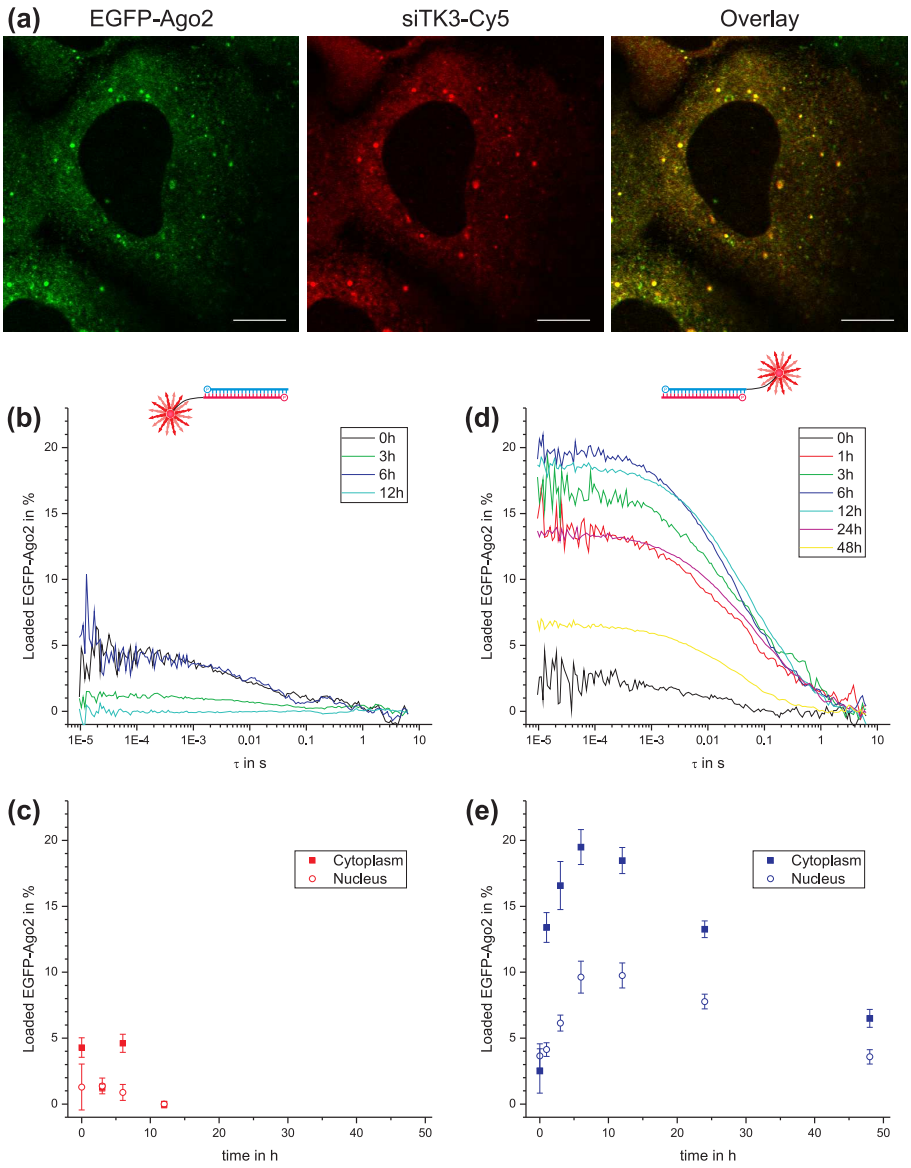

Figure 5.3: Asymmetric guide strand incorporation into RISC. (**a**) LSM images of 10G cells 3 h after microinjection of siTK3 (green: EGFP-Ago2, red: siTK3, right panel: overlay). Scale bars indicate 10 µm. (**b**) Normalized cross-correlation curves of EGFP-Ago2 and the labeled passenger strand of siTK3 in the cytoplasm for different incubation times after microinjection in 10G cells *in vivo*. (**c**) Resulting cross-correlation amplitudes for the labeled passenger strand in the cytoplasm (filled boxes) and the nucleus (open circles). (**d**) Normalized cross-correlation curves of EGFP-Ago2 and the labeled guide strand of siTK3 in the cytoplasm for different incubation times after microinjection in 10G cells *in vivo*. (**e**) Resulting cross-correlation amplitudes for the labeled guide strand in the cytoplasm (filled boxes) and the nucleus (open circles). Data are represented as mean±SEM.

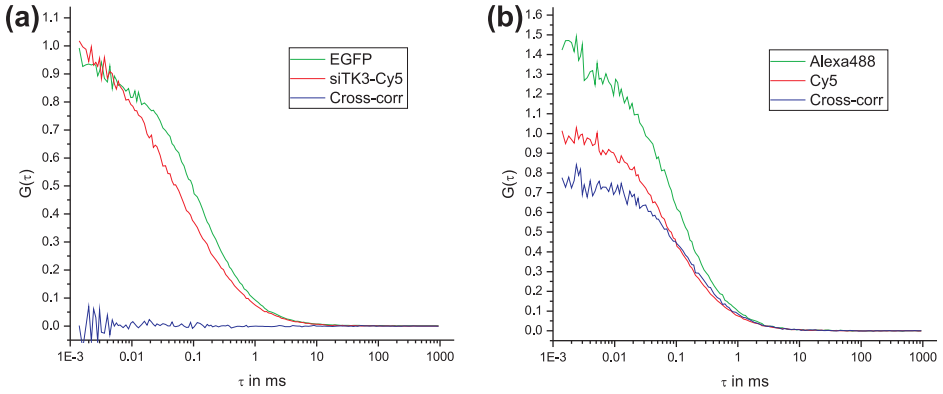

Figure 5.4: Incorporation assay controls. (**a**) Negative control, normalized auto- (green and red) and cross-correlation (blue) curves of EGFP (green) and siTK3-Cy5 (red) *in vitro*. (**b**) Positive control, normalized auto- (green and red) and cross-correlation (blue) curves of a Alexa488 (green) and Cy5 (red) double-labeled siRNA test sample *in vitro*.

(Fig. 5.4(a)). The first reason is that the cells contain unlabeled endogenous Argonaute proteins (Ago1-4), which binds also to the labeled siRNAs, and thereby preventing these labeled siRNAs from binding to labeled Ago2. The second reason is that human cells produce endogenous unlabeled miRNAs, which also become incorporated into labeled Ago2, and thereby blocking these Ago2 proteins from loading labeled siRNAs.

Nevertheless, these results demonstrate the suitability of the FCCS-incorporation assay to study the asymmetric incorporation of siRNAs into RISC.

5.3.2 Interaction Between RISC and Its Target Studied by Dual-Color FCCS

To probe the interaction of activated RISC with targeted RNAs, a 50 nt long target-RNA was designed. It contains the siTK3 target site and a Cy5 label at the 5' end. Seven nucleotides at each end were 2'-O-methyl modified to protect the single stranded target-RNA against intracellular RNases. 10 to 18 hours after the transfection of the 10G cells with the unlabeled siRNA, the Cy5-labeled target-RNA was microinjected into the cells. This time point was selected, because siRNA incorporation displayed its maximum between 6 and 24 h (compare Fig. 5.3(E)). The cross-correlation amplitudes between the loaded and cleavage activated EGFP-Ago2 and the Cy5-labeled target-RNA were measured for several incubation times. If the loaded guide strand does not contain a sequence that matches the sequence of the target-RNA, the interaction between RISC and the

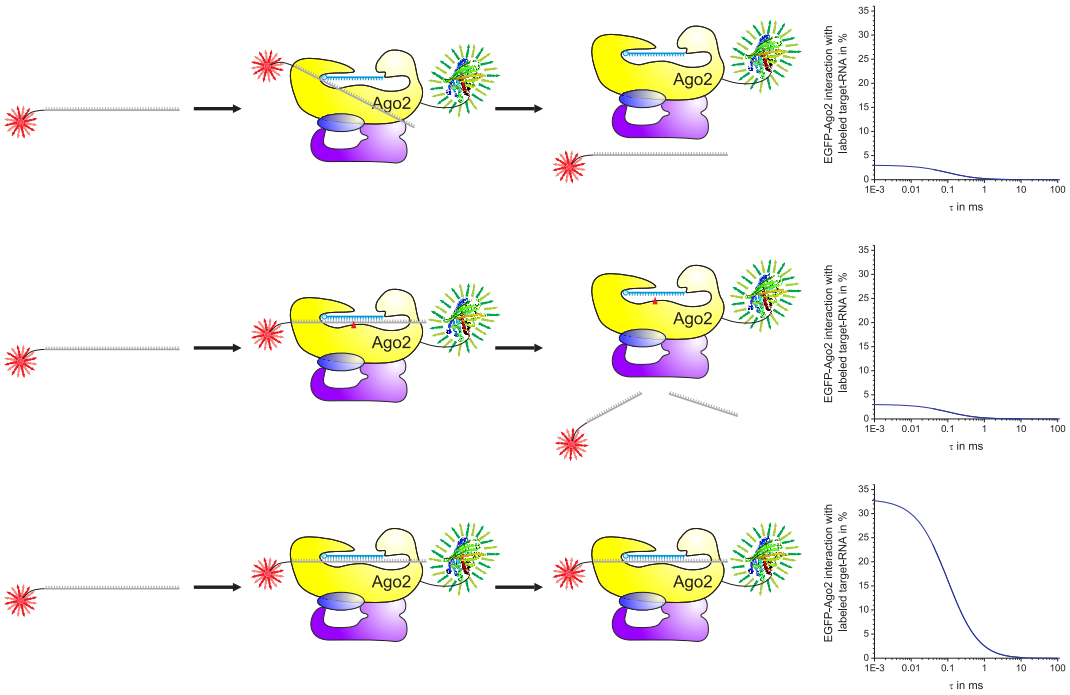

Figure 5.5: FCCS assay to measure RISC-target interaction. FCCS *in vivo* assay to study the interaction of activated RISC with its target. Three types of interaction are expectable. First, the target and the loaded guide strand do not have a complementary sequence. This leads to only a very short interaction, and the target is released unchanged from activated RISC and results in low cross-correlation amplitudes (upper panel). In case of perfect match between the loaded guide strand and the labeled target, the activated RISC binds the target and cleaves it. The cleavage products are released from RISC, which again results in low cross-correlation amplitudes (middle panel). In case of a matching sequence, but an inhibited cleavage activity, due mismatches, bulges, or chemical modifications, RISC and its target form a miRNA-like interaction, where the target stays bound to RISC, resulting in high cross-correlation amplitudes (lower panel).

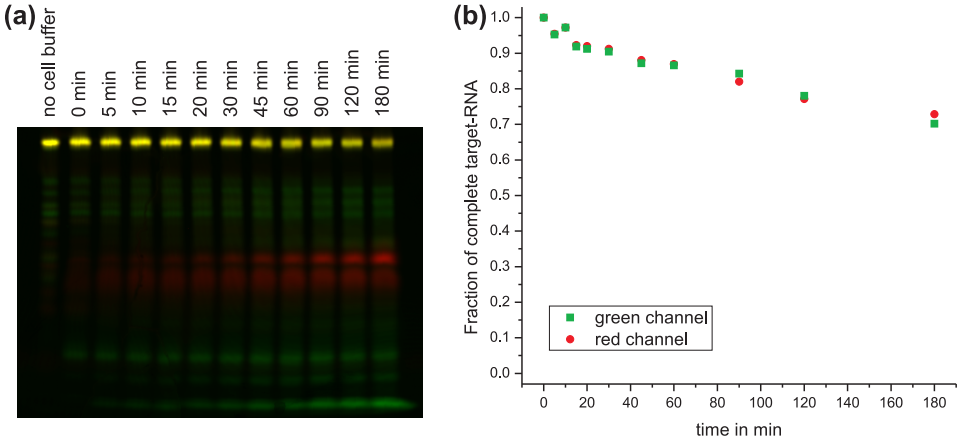

Figure 5.6: Stability of target-RNA. (**a**) PAGE picture of double labeled target-RNA (3'end-Alexa488, 5'end-Cy5) incubated for the given times with HeLa S20 cell extract at 37°C. (**b**) Fraction of intact target-RNA molecules over incubation time (Quantification from the PAGE picture).

target-RNA is very short and the target-RNA is released unchanged. This results in low cross-correlation amplitudes (Fig. 5.5, upper panel). In case of a perfect complementarity between loaded guide strand and target-RNA, RISC cleaves the target-RNA and the cleavage products are released from RISC. This again results in a low cross-correlation amplitude (Fig. 5.5, middle panel). In the third case, there is enough complementarity between guide strand and target-RNA, but the cleavage activity of RISC is impaired either due to mismatches, bulges, or chemical modifications. In this case the interaction between RISC and target-RNA is like a miRNA guided interaction, where the targeted RNA stays bound to RISC. This lead to high cross-correlation amplitudes (Fig. 5.5, lower panel).

To test the stability of the single stranded target-RNA against intracellular RNases, the target-RNA was incubated with HeLa S20 cell extract between 5 and 180 minutes at 37°C. The amount of intact target-RNA was analyzed by polyacrylamide gel electrophoresis (PAGE) (Fig. 5.6). After 60 min of incubation more than 85% and after 180 min more than 70% of target-RNA was intact (Fig. 5.6). The target-RNA was stable enough to test the interaction of loaded RISC and the target-RNA up to three hours after microinjection.

After microinjection the target-RNA localized to the cytoplasm and displayed a slight accumulation in the nucleus and even stronger in nucleolar structures (Fig. 5.7(a)). To study the interaction of siRNA loaded RISC with its target, the siRNA siTK3-bulge was used, where the bases 9-11 were replaced. This leads to the formation of a central bulge in the interaction with the siTK3 target site and

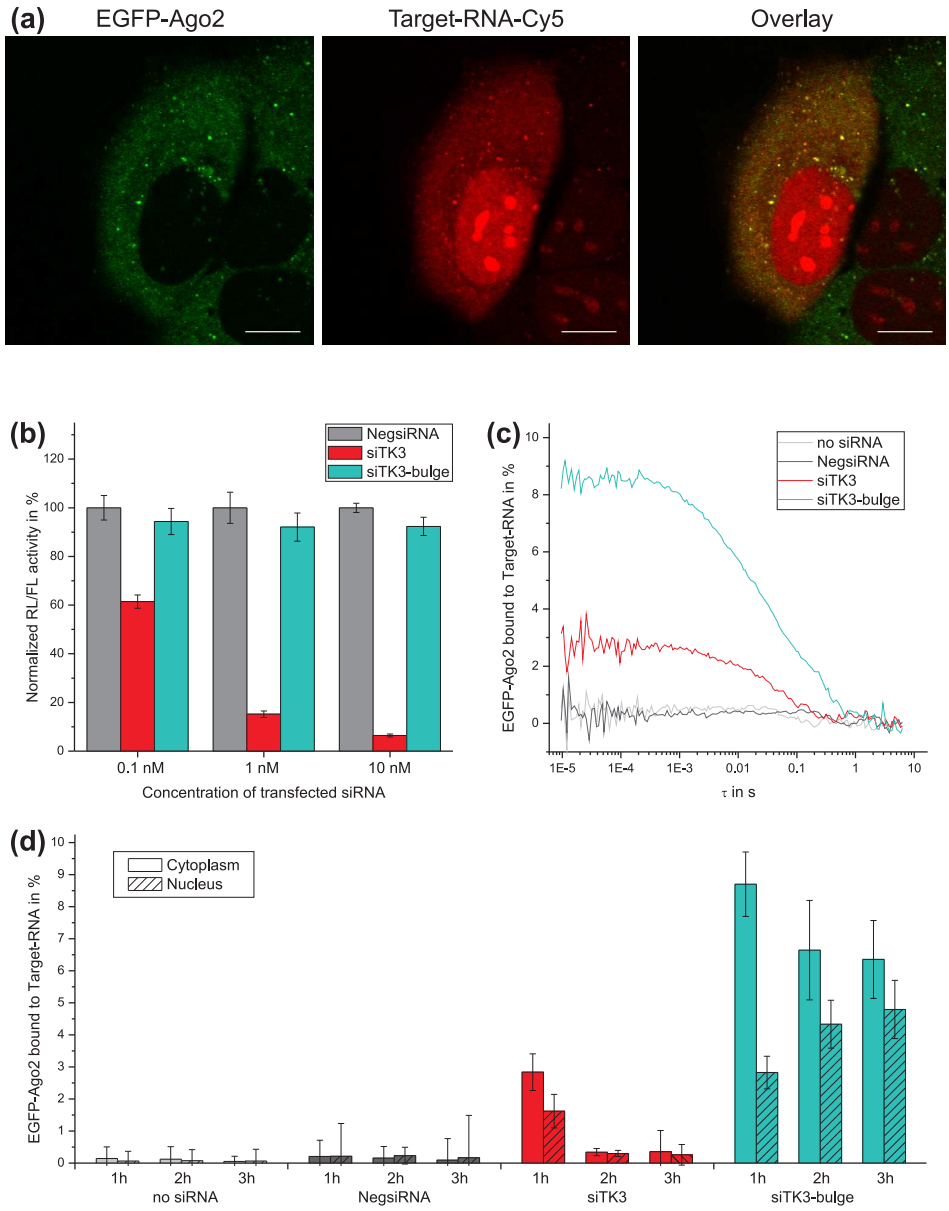

Figure 5.7: Target interaction of siTK3-bulge loaded RISC. (**a**) LSM images of 10G cells 1 h after microinjection of target-RNA (green: EGFP-Ago2, red: target-RNA, right panel: overlay). Scale bars indicate 10 µm. (**b**) Silencing activity of indicated amounts of siTK3-bulge measured with a Dual-Luciferase Assay. As controls silencing of NegsiRNA and siTK3 is also shown. Data are represented as mean±SD. (**c**) Normalized cross-correlation curves of EGFP-Ago2 loaded with indicated siRNAs and the Cy5-labeled target-RNA in the cytoplasm 1 h after microinjection in 10G cells *in vivo*. (**d**) Resulting cross-correlation amplitudes between target-RNA and RISC, loaded with indicated siRNAs, measured in the cytoplasm (empty bars) and the nucleus (striped bars), 1 h to 3 h after microinjection. Data are represented as mean±SEM.

thereby trigger a miRNA-like interaction. The results of the silencing assay show that siTK3-bulge is silencing inactive. It is unable to trigger the cleavage reaction of RISC (Fig. 5.7(b)). FCCS measurements in non-transfected and NegsiRNA transfected 10G cells after 1 to 3 h of target-RNA delivery showed no interaction of RISC with the target-RNA (Fig. 5.7(d)). This illustrates the assay specificity and the absence of miRNA target sites within the target-RNA. The transfection of perfectly matching and cleavage active siTK3 resulted in very low levels of EGFP-Ago2-target-RNA interaction. In contrast, the transfection of central bulge forming and silencing inactive siTK3-bulge yielded in high levels of RISC bound target-RNA in the cytoplasm. In the nucleus however, the interaction levels were 3-fold lower in the beginning but increased with longer incubation almost reaching cytoplasmic interaction levels after 3 h (Fig. 5.7(d)).

These results demonstrate the short interaction time of RISC loaded with a perfectly matching siRNA with the target-RNA and that bulges in the center of the guide-strand-target-RNA hybridization increase the lifetime of the RISC-target-RNA interaction. Additionally the localization of functional guide-strand loaded RISC to the nucleus and the accumulation of the cleavage impaired RISC-target-RNA complex in the nucleus is demonstrated.

Accordingly it was shown that *in vivo* FCCS is a perfect tool to study the interaction between siRNA-loaded RISC and targeted RNAs and that siTK3-bulge can function as a positive control in the following experiments.

5.3.3 Cellular Model for Human RISC Loading and Shuttling

For the understanding of the influence of chemically modified siRNAs on the RNAi pathway it is necessary to have a current model of the intracellular RNAi pathway. First a summary of the additional results published in our paper [393] will be given here, to motivate our model.

Mobility measurements of cytoplasmic and nuclear RISC by measuring the diffusion constant of EGFP-hAgo2 with fluorescence correlation spectroscopy (FCS) revealed that nuclear RISC (nRISC) diffuses much faster than cytoplasmic RISC (cRISC). Control measurements with EGFP in both compartments showed that this is not an environmental effect, because the diffusion of EGFP was the same in both compartments. With the assumption of spherical proteins the molecular mass could be calculate for cytoplasmic and nuclear RISC to (3.0±0.6) MDa and (158±26) kDa, respectively. From these results together with biochemical control experiments, we concluded that EGFP-Ago2 is part of a huge RISC complex in the cytoplasm, whereas in the nucleus RISC is most probably formed by the discrete EGFP-Ago2 protein. The concentration of EGFP-Ago2 was four to five times higher in the cytoplasm compared to the nucleus.

To further study nRISC, siRNAs targeting the nuclear RNA 7SK were microinjected in 10G cells and the cross-corrleation between EGFP-Ago2 and the guide

strand labeled siRNA was measured in both cellular compartments. To our surprise, we found an accumulation of loaded RISC in the nucleus for one out of three 7SK targeting siRNAs. A more detailed inspection showed that the accumulating siRNA targets a region of the 7SK RNA which forms a hairpin structure. This hairpin structure impairs the cleavage activity of Ago2 and probably leads to a miRNA-like interaction between nRISC and the targeted 7SK RNA. This miRNA-like interaction is probably the reason for the accumulation of RISC loaded with the hairpin targeting siRNA in the nucleus.

The target dependent accumulation of nRISC and the fact that nRISC is to small to form the RISC loading complex (RLC) (containing EGFP-Ago2, TRBP

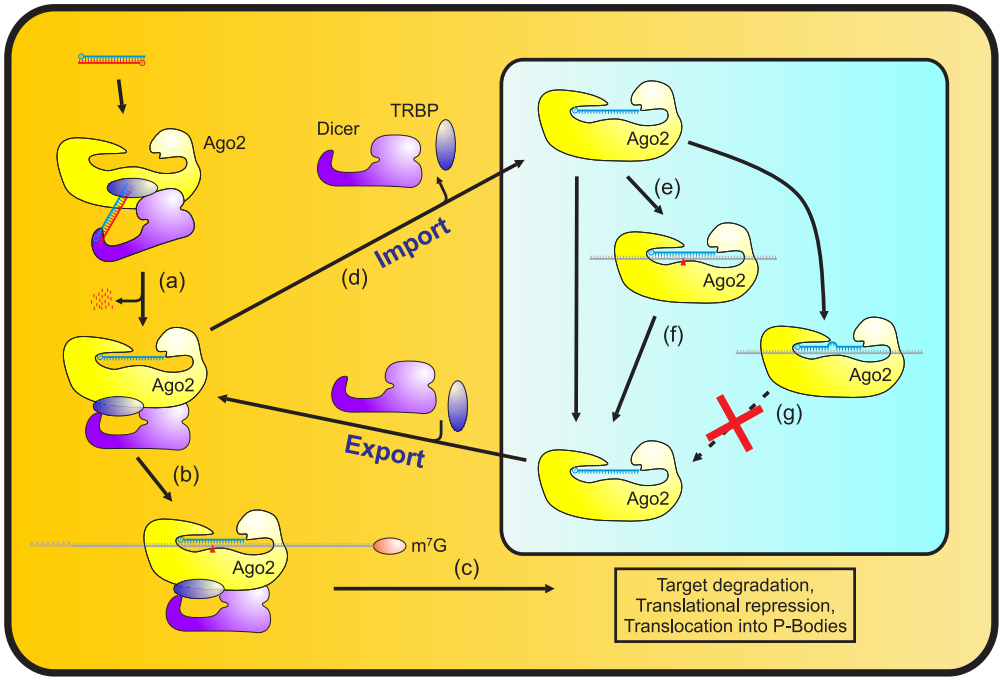

Figure 5.8: Human RISC loading and shuttling model. (a) Asymmetric guide strand incorporation is localized in the cytoplasm only. (b) Guide strand mediated target recognition in the cytoplasm. (c) A perfect match results in RISC mediated target degradation, while a more miRNA-like interaction leads to translational repression and translocation into P-bodies. (d) A fraction of cytoplasmic RISC is imported into the nucleus to ensure cell wide target regulation. The cytoplasmic co-factors dissociate from hAgo2 protein, thereby forming nRISC. (e) Guide strand mediated target recognition in the nucleus. (f) A perfect match results in RISC mediated target degradation and reformation of free nRISC, which can be exported into the cytoplasm, while a miRNA-like interaction leads to accumulation of RISC in the nucleus resulting in efficient regulation.

and Dicer, together around 380 kDa) lead to the hypothesis that RISC is predominantly loaded in the cytoplasm and shuttled between cytoplasm and nucleus. Additional reasons for this hypothesis are that siRNAs are to short to contain localization signals, so RISC has to find its target in both compartments and siRNAs have a cytoplasmic localization, mediated by Exportin 5 [216–219, 389]. To test this hypothesis the loading of RISC with the siRNA targeting the hairpin structure of 7SK was performed with and without blocking the transport mechanisms of the nuclear envelope by wheat germ agglutinin (WGA). Without blocking the nuclear envelope cross-correlation levels of more than 20% were found in both the cytoplasm and the nucleus. Injecting the siRNA together with WGA into the cytoplasm, left the cross-correlation in the cytoplasm unchanged but reduced the nuclear cross-correlation 3-fold down to 7%. The injection of the siRNA together with WGA into the nucleus changed the localization pattern of the siRNA from cytoplasmic to nuclear (visualized by LSM) and the cross-correlation level in the nucleus stayed on the low level, whereas the cytoplasmic cross-correlation decreased to 12%, due to low siRNA levels in the cytoplasm. These results support our hypothesis and lead us to formulate the following model (Fig. 5.8) for the intracellular RNAi pathway.

In our model a predominantly cytoplasmic loading of RISC and a shuttling mechanism for activated RISC between cytoplasm and the nucleus is proposed. (a) The RLC is localized and interacts with siRNAs and miRNAs exclusively in the cytoplasm. It senses the asymmetry of the silencing trigger and specifically incorporates the guide strand into hAgo2, thereby forming cRISC. The FCCS measurements showed the maximum for this incorporation within the first 3 to 12 hours, so the incorporation mechanism seems to be regulated. The majority of activated cRISC remains in the cytoplasm as a 3 MDa complex to regulate the gene expression of mRNAs. (b) The guide strand mediates the target interaction and in case of perfectly priming between the guide strand and the target RNA cRISC guides target degradation (c). In case of a miRNA-like interaction cRISC remains bound to the targeted mRNA and regulate its expression and/or translocation to P-bodies. (d) A fraction of cRISC translocates into the nucleoplasm, where it forms nRISC of $\sim$ 158 kDa, most likely composed of only hAgo2. This translocation into the nucleus ensures a cell wide target regulation. (e) Again also in the nucleus the guide strand mediat the target interaction and in case of a perfect match nRISC performs target degradation, which leads to the reformation of free nRISC (f). (g) On the contrary, cleavage impaired nRISC, e.g. caused by double stranded RNA (dsRNA) regions or bulges, results in the accumulation of this particularly loaded RISC in the nucleus, facilitated by its prolonging interaction with the target RNA. Since a concentration increase of nRISC was never detected, it is reasoned that a stable equilibrium between nRISC and cRISC exists that is shifted for a particularly loaded nRISC depending on the target interaction.

5.4 Influence of Chemical Modified siRNAs onto the RNAi Mechanism

5.4.1 FCCS Compatibility of Different Chemical Modifications

The three most commonly used and best characterized RNA-modifications: 2'-O-methyl, 2'-fluoro, and phosphorothioate modifications were already described in section 4.4. In brief, 2'-O-methyl and 2'-fluoro modification are modifications of the ribose, where the hydroxyl group at the second position is replaced with a methylated oxygen or a fluorine, respectively (Fig. 4.2, 3. and 4. column (p. 60)). The phosphorothioate modification is a modification of the phosphate backbone, where an oxygen in the backbone is substituted by a sulfur (Fig. 4.2, 5. column (p. 60)).

To test the compatibility of these chemical modifications with the RISC-incorpo-

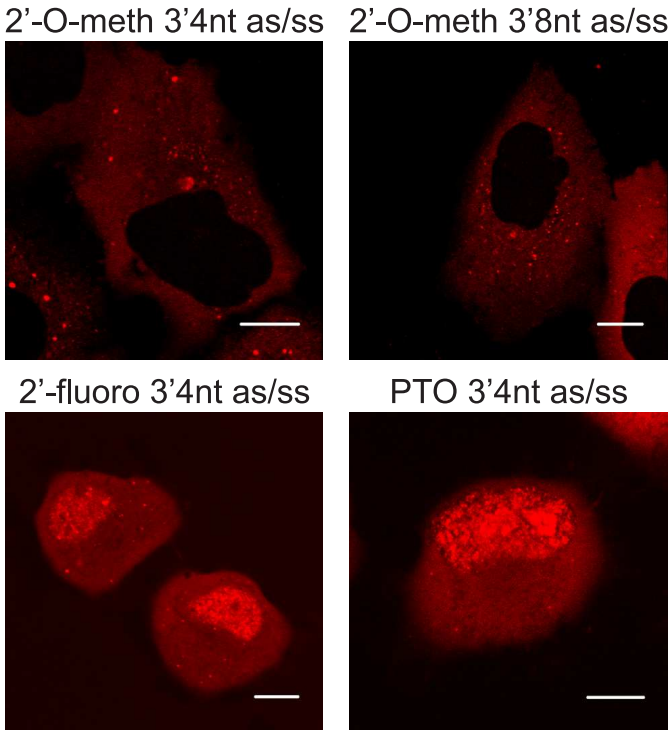

Figure 5.9: Sub-cellular localization of differently modified siRNAs after microinjection. Sub-cellular localization of siRNAs with 2'-O-methyl modification on the first four (upper left panel) and eight (upper right panel) nucleotides counted from the 3' end. The localization of siRNAs with, where the first four nucleotides counted from the 3' end carry either 2'-fluoro- (lower left panel) or phosphorothioate (lower right panel) modifications. Scale bars indicate 10 µm.

ration- and RISC-target-interaction-FCCS-assay, differently modified Cy5-labeled siRNAs were microinjected into ER293 cells, to study their intracellular localization and diffusion *in vivo*. As it was already described in [367], the 2'-fluoro and phosphorothioate modified siRNAs show a preferential nuclear localization illustrated by a strong and punctuate accumulation of these siRNAs in the nucleus, compared to the predominantly cytoplasmic localization of 2'-O-methyl modified and unmodified siRNAs (Fig. 5.9).

In vivo FCCS experiments with 3'-4 nt long phosphorothioate and 2'-fluoro modified siRNAs displayed strong bleaching rates especially in the nucleus, compared to no or only small bleaching for 2'-O-methyl modified siRNAs (data not shown). The strong bleaching of the phosphorothioate and 2'-fluoro modified siRNAs might arise from a decreased mobility of these siRNAs leading to a longer dwell time in the focal volume. The cause for this decreased mobility could be the increased affinity of these modified siRNAs to proteins [394]. Therefore, the strong bleaching made it impossible to obtain quantitative results by FCCS for 2'-fluoro and phosphorothioate modified siRNAs, but the 2'-O-methyl modified siRNAs were suitable for a detailed *in vivo* FCCS analysis to investigate positional and quantity dependent effects on siRNA affinity to RISC, strand separation, asymmetry, guide strand incorporation, stability of the guide RNA-RISC interaction, target RNA recognition and cleavage.

5.4.2 Increased 2'-O-methyl Modifications on the 3'-end Inhibit Strand Separation and Target-RNA Cleavage

siTK3 siRNA was used to study the influence of 2'-O-methyl modifications on the incorporation and strand separation of these siRNAs and the interaction of siTK3-loaded RISC with the target-RNA. siTK3 targets the mRNA of Renilla luciferase

Figure 5.10 *(facing page)*: Silencing, loading, and target interaction of increasingly 3' end modified siRNAs (**a**) Sequence of the used siTK3 with indication of the increasing length of 2'-O-methyl modified parts. (**b**) Silencing activity of indicated amounts of 2'-O-methyl modified siRNAs measured with a Dual-Luciferase Assay. As controls silencing of NegsiRNA and siTK3 is also shown. Data are represented as mean±SD. (**c**) Cross-correlation amplitudes between labeled guide strand and EGFP-Ago2 measured in the cytoplasm (empty bars) and the nucleus (striped bars), 3 h and 12 h after microinjection. (**d**) Cross-correlation amplitudes between labeled passenger strand and EGFP-Ago2 measured in the cytoplasm (empty bars) and the nucleus (striped bars), 3 h and 12 h after microinjection. (**e**) Resulting cross-correlation amplitudes between target-RNA and RISC loaded with indicated modified siRNAs measured in the cytoplasm (empty bars) and the nucleus (striped bars), 1 h to 3 h after microinjection. Data are represented as mean±SEM.

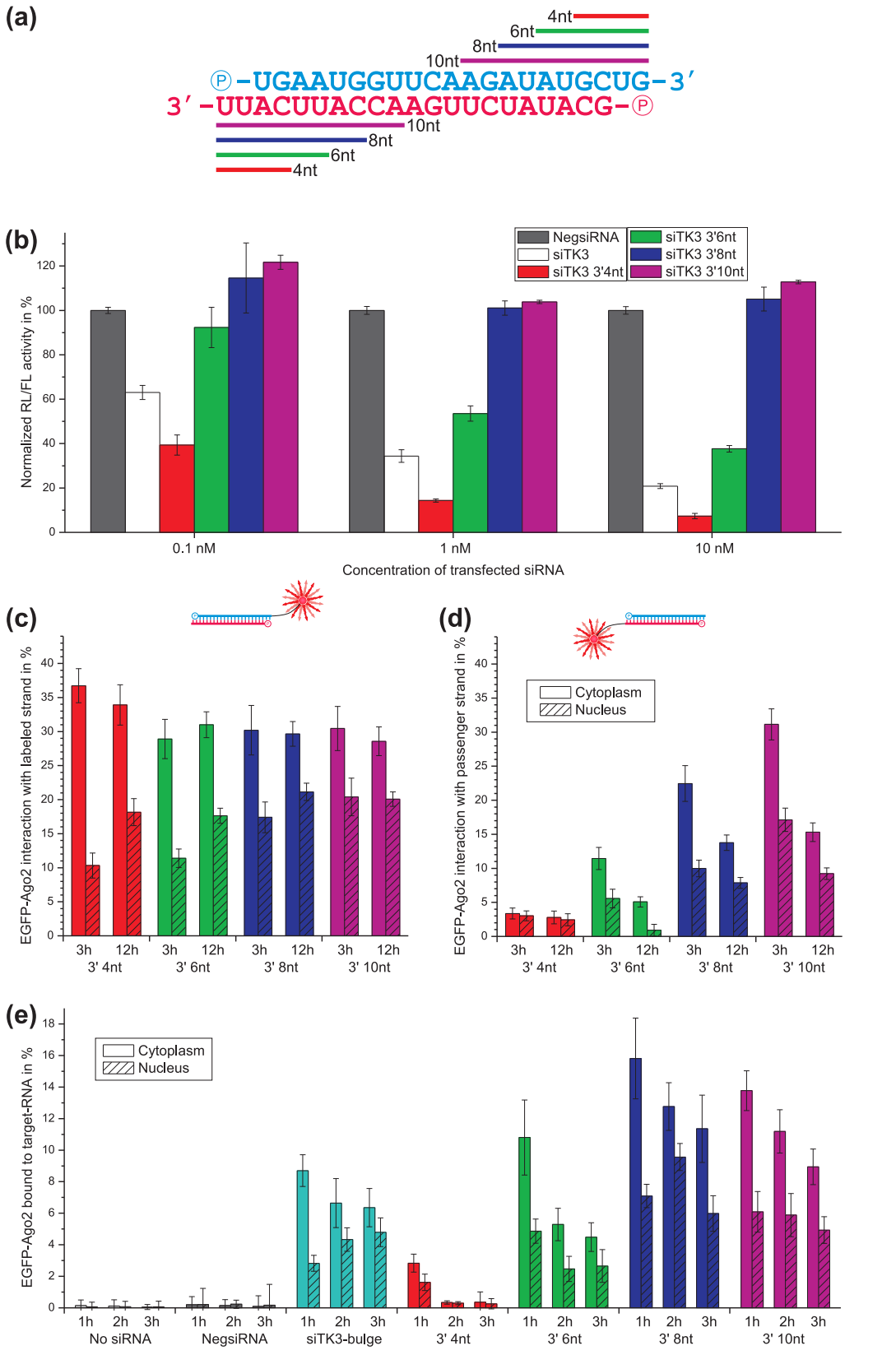
(a)
4nt
6nt
8nt
10nt
Ⓟ–UGAAUGGUUCAAGAUAUGCUG–3′
3′–UUACUUACCAAGUUCUAUACG–Ⓟ
10nt
8nt
6nt
4nt
(b)
NegsiRNA
siTK3
siTK3 3'4nt
siTK3 3'6nt
siTK3 3'8nt
siTK3 3'10nt
Normalized RL/FL activity in %
0.1 nM
1 nM
10 nM
Concentration of transfected siRNA
(c)
EGFP-Ago2 interaction with labeled strand in %
3h 12h
3' 4nt
3' 6nt
3' 8nt
3' 10nt
(d)
Cytoplasm
Nucleus
EGFP-Ago2 interaction with passenger strand in %
(e)
EGFP-Ago2 bound to target-RNA in %
1h 2h 3h
No siRNA
NegsiRNA
siTK3-bulge
3' 4nt
3' 6nt
3' 8nt
3' 10nt

encoded on the plasmid pRL-TK, but does not show any sequence homology with endogenous mRNA transcripts. The siTK3 displays a strictly asymmetric incorporation of the guide strand (Fig. 5.3(c),(e) (p. 71)) and high levels of Renilla luciferase silencing (Fig. 5.10(b)).

To study the positional effects of 2'-O-methyl modifications within small RNAs, siTK3 siRNAs with constantly increasing numbers of 2'-O-methyl modifications on the 3' end were generated (Fig. 5.10(a)). To test the silencing activity of these modified siRNAs a dual-luciferase assay was performed. The introduction of four 2'-O-methyl modified nucleotides at the 3'-end resulted in increased silencing activity compared to unmodified siRNAs. On the other side, the introduction of six 2'-O-methyl modified nucleotides resulted in strongly reduced silencing activity, and silencing was completely abolished with eight and ten 2'-O-methyl modified nucleotides on the 3'-end (Fig. 5.10(b)).

For further characterization of the mechanism of silencing inhibition, the interaction of these differently modified siRNAs with Ago2 was tested *in vivo* by FCCS. Therefore, guide strand labeled siTK3 duplexes were microinjected, and the amount of loaded Ago2 was analyzed by FCCS after 3 and 12 h. These two time points were chosen, because the 3 h value represents the early (still rising RISC-loading level) and 12 h the late RISC-activation phase (already declining RISC-loading level) (Fig. 5.3(e) (p. 71)). Therefore, they are ideally suited to investigate e.g. strand separation or RISC stability as both time points display almost identical loading levels in the cytoplasm.

Under the used experimental conditions, no differences could be detected for the interaction of the guide strand labeled siTK3 duplexes to Ago2 between the silencing active four nucleotide 2'-O-methyl modified duplex and the silencing impaired duplexes containing 6-10 2'-O-methyl modified nucleotides. All labeled guide strands were incorporated equally well with cross-correlation amplitudes of 30-35% (Fig. 5.10(c)).

To investigate the effect of 2'-O-methyl modifications on strand separation and asymmetric incorporation, the aforementioned modified siTK3 duplexes labeled on the passenger strand were microinjected, and the resulting cross-correlation amplitudes were compared to the amplitudes for guide strand labeled duplexes (Fig. 5.10(d)). The silencing active duplex containing four 2'-O-methyl modifications on the 3'-end displayed almost no interaction of RISC with the labeled passenger strand. With increasing amounts of introduced 2'-O-methyl modified nucleotides the interaction of the labeled passenger strand with RISC increases in the cytoplasm as well as in the nucleus. For the completely inhibited duplexes containing eight and ten 2'-O-methyl modified nucleotides almost identical incorporation levels in the cytoplasm after 3 h compared to guide strand labeled duplexes were obtained, whereas after 12 h a clear reduction of RISC passenger strand interaction could be detected. A collection of cross-correlation curves for this data is plotted in Fig. 5.11(a).

This indicates that the silencing inhibition of longer 3' end 2'-O-methyl modified siRNAs is not a result of reduced affinities of these 2'-O-methyl modified siRNAs to the RLC or of a changed asymmetry in the incorporation process, but they clearly show that longer 3' end 2'-O-methyl modification inhibit the strand separation during the activation of RISC. It has been shown that hAgo2 containing RISC cleaves the passenger strand during activation to facilitate strand separation [247, 248], so probably the inhibition of strand separation is an inhibition of the passenger strand cleavage. This is supported by the finding that the level of passenger strand labeled duplex bound to RISC strongly decreases after 12 h compared to 3 h. Which points out that next to the cleavage-mediated passenger

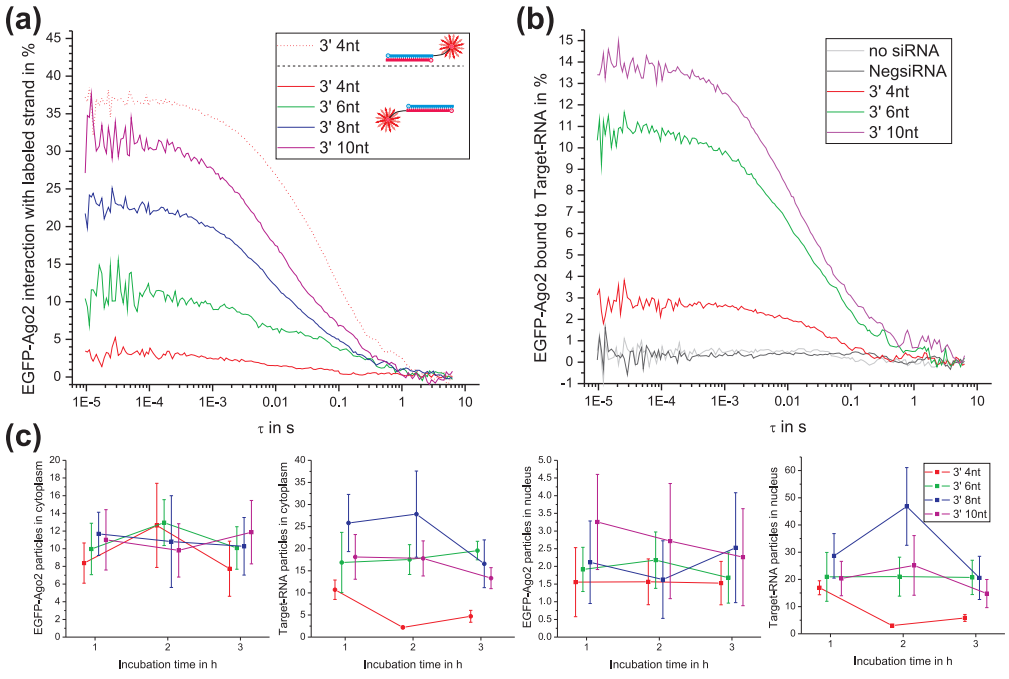

Figure 5.11: Cross-correlation curves and particle numbers (**a**) Normalized cross-correlation curves of EGFP-Ago2 and the Cy5-labeled strand of siTK3 siRNAs with different amount of 2'-O-methyl modified nucleotides measured in the cytoplasm 3 h after microinjection. (**b**) Normalized cross-correlation curves between the Cy5-labeled target-RNA and EGFP-Ago2 loaded with the indicated siRNAs measured in the cytoplasm 1 h after microinjection. (**c**) Particle numbers of EGFP-Ago2 and Cy5-labeled target-RNA in the cytoplasm and nucleus for the target-interaction measurements. The strong decrease for the target-RNA particles after 1 h in the experiment with 3' 4 nt modified siTK3 is probably induced through the strong cleavage reaction of RISC and the following degradation of the target-RNA.

strand release a bypass mechanism exists that also results in strand separation and passenger strand removal. Due to the fact that no reduction of the interaction levels between guide strand-labeled duplexes and RISC could be detected, a release of the duplex during the incorporation period could be excluded. This bypass mechanism is much slower compared to the cleavage-mediated mechanism.

The also increasing interaction levels of RISC with the labeled passenger strand with increasing length of 2'-O-methyl modifications in the nucleus could have several reasons. One reason could be that RISC with bound 2'-O-methyl modified siRNA duplex is imported into the nucleus. The reduction of the nuclear interaction levels after 12 h compared to 3 h can in this case be explained by a shuttling of duplex containing RISC between cytoplasm and nucleus and a working bypass mechanism in the cytoplasm and/or a working bypass mechanism in the nucleus. Another reason for the increased interaction levels in the nucleus could also be the rebinding of labeled passenger strands which were removed from RISC by the bypass mechanism, but were not degraded due to the increased length of 2'-O-methyl modifications and travel as single strands into nucleus.

To elucidate the influence of increasing amounts of 2'-O-methyl modifications on the 3' end onto the interaction of active RISC with its target, the interaction of RISC with target-RNA was studied *in vivo* by FCCS (compare Fig. 5.5 (p. 73)). Therefore, a 50 nucleotide long, single stranded, and fluorescently labeled RNA containing the target sequence for siTK3 and is stabilized by seven 2'-O-methyl modified nucleotides on each end, was microinjected in siRNA transfected 10G cells. For the silencing active siTK3 duplex with four 2'-O-methyl modified nucleotides, interaction levels close to zero were found, indicating the cleavage activity of RISC followed by the release of the cleavage products (Fig. 5.10(e)). For siRNAs with increasing amounts of 2'-O-methyl modified nucleotides, the amounts of RISC bound to target-RNA increased in correlation to the aforementioned silencing activities (Fig. 5.10(b,e)). A collection of cross-correlation curves is displayed in Fig. 5.11(b). As negative controls the amounts of RISC bound to target-RNA in non-transfected cells or transfected with a control siRNA sharing no sequence complementarity with the target-RNA (NegsiRNA) are shown. The values for siTK3-bulge tranfected cells are plotted as positive control (Fig. 5.10(e)). To rule out any concentration mediated effects or changed EGFP-Ago2 expression levels, the average number of particles obtained from the autocorrelation curves are shown in Fig. 5.11(c), clearly demonstrating homogeneous levels for both species over the time of the experiment, except for the target-RNA in case of 4 nt modified siTK3. The strong decrease there after 1 h can be explained by the strong cleavage reaction of RISC for this siRNA and the following degradation of the cleaved target-RNA.

Interestingly, RISC loaded with the guide RNAs containing 8-10 2'-O-methyl modified nucleotides displayed even higher interaction levels with the target-RNA than RISC loaded with a bulge-forming guide strand (Fig. 5.10(e)). These higher

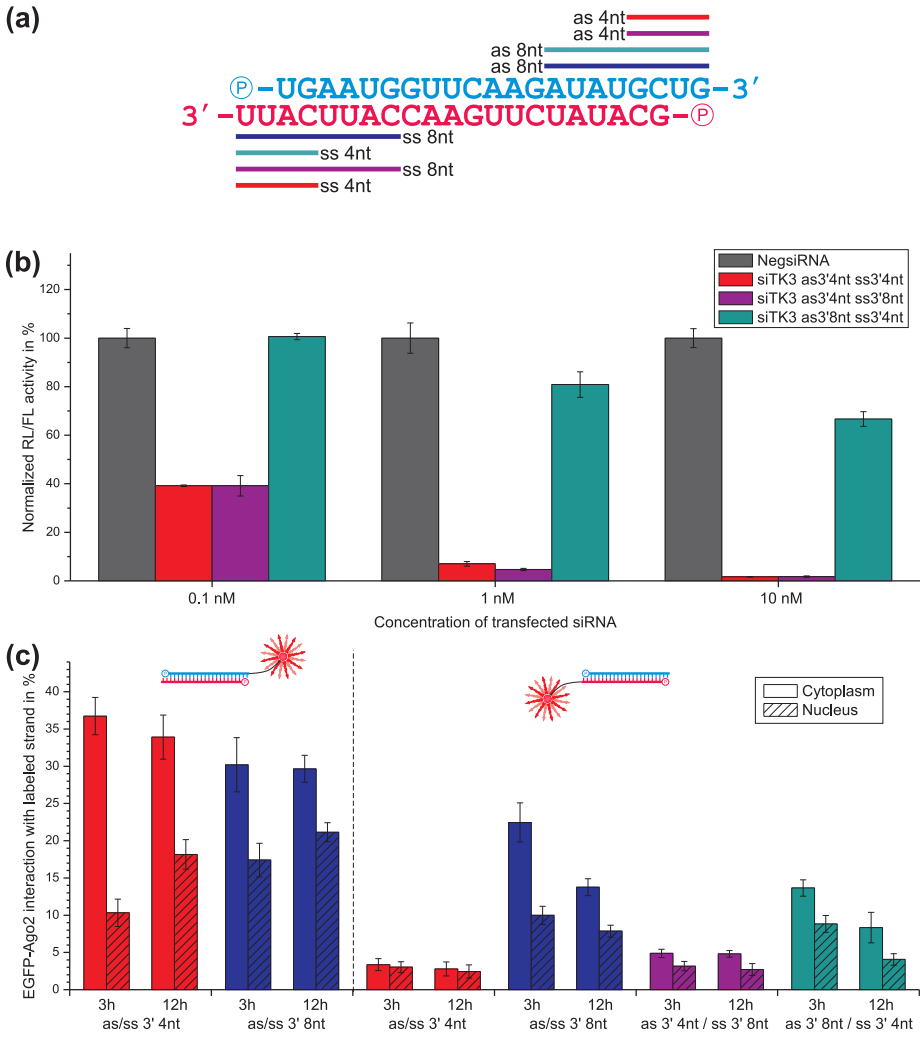

Figure 5.12: Silencing and loading of guide or passenger strand modified siRNAs (**a**) Sequence of the used siTK3 with indication of the 2'-O-methyl modified parts. (**b**) Silencing activity of indicated amounts of partially 2'-O-methyl modified siRNAs measured with a Dual-Luciferase Assay. As controls silencing of NegsiRNA and siTK3 containing 4 modified nucleotides on both strands is also shown. Data are represented as mean±SD. (**c**) Cross-correlation amplitudes between labeled strand and EGFP-Ago2 measured in the cytoplasm (empty bars) and the nucleus (striped bars), 3 h and 12 h after microinjection. The labeled strand is indicated by the cartoon. Data are represented as mean±SEM.

amplitudes might result from a stabilization effect of the 2'-O-methyl modification on the RISC-target interaction caused either by the increased affinity due to the complete hybridization of the guide-target RNA duplex or by the protection of the guide strand against nucleases.

From the measured silencing inhibition of the siRNAs containing eight or ten 2'-O-methyl modified nucleotides (Fig. 5.10(b)) the question arose, if this inhibition is caused by the modification on the guide or passenger strand. Therefore, the silencing activity of only partial modified siRNA duplexes were measured (Fig. 5.12(a)). The siRNA containing eight 2'-O-methyl modified nucleotides on the passenger strand displayed no inhibition of silencing and reached levels comparable to the positive control, whereas the modification on the guide strand resulted in an almost complete loss of the silencing activity (Fig. 5.12(b)).

To investigate the influence of a strand specific 2'-O-methyl modification *in vivo*, siRNAs, that were either modified with eight nucleotide long 2'-O-methyl modifications on the guide or passenger strand only, were microinjected in 10G cells. The passenger strand release was investigate after 3 h and 12 h. In agreement with the silencing experiments, strand separation was mainly inhibited, when the guide strand of the duplex was modified, whereas the modified passenger strand showed only marginal effects (Fig. 5.12(c)).

5.4.3 2'-O-methyl Modifications on the 5'-end Lead to Destabilization of the RISC-Guide RNA Interaction

After characterizing the effect of 2'-O-methyl modifications on the 3'-end, the influence of two 2'-O-methyl modified nucleotides on the 5'-end (Fig. 5.13(a)) was tested. In the silencing readouts a strong decrease of silencing activity of the 5' end modified siRNA was detected (Fig. 5.13(b)). To identify if the inhibition results from the guide or the passenger strand only, duplexes with either guide or passenger strand were also analyzed. The duplex with 5'-end guide strand modification showed the same silencing inhibition as the dual modified siRNA, whereas the modification on the passenger strand had no impact on the silencing activity (Fig. 5.13(b)). To analyze the affinity of the 5'-end modified siRNA to RISC, the guide strand labeled siRNA-duplex was microinjected in 10G cells. After 3 h the same amount of guide strand loaded RISC was found for the 5' end modified siRNA and for the only 3'-end modified one. So the affinity of 5'-end modified duplex to RLC/RISC is not affected. However, after 12 h a strong decrease by one third (34% down to 22%) of guide strand loaded RISC approximately was detected, whereas the levels of only 3'-end modified siRNA remained stable (Fig. 5.13(c)). This result shows that the 5'-end 2'-O-methyl modification destabilizes the interaction of RISC with the modified guide strand. Passenger strand removal was not inhibited, because no increased levels of passenger strand-RISC interaction could be detected. This destabilization might cause the relatively strong silencing inhi-

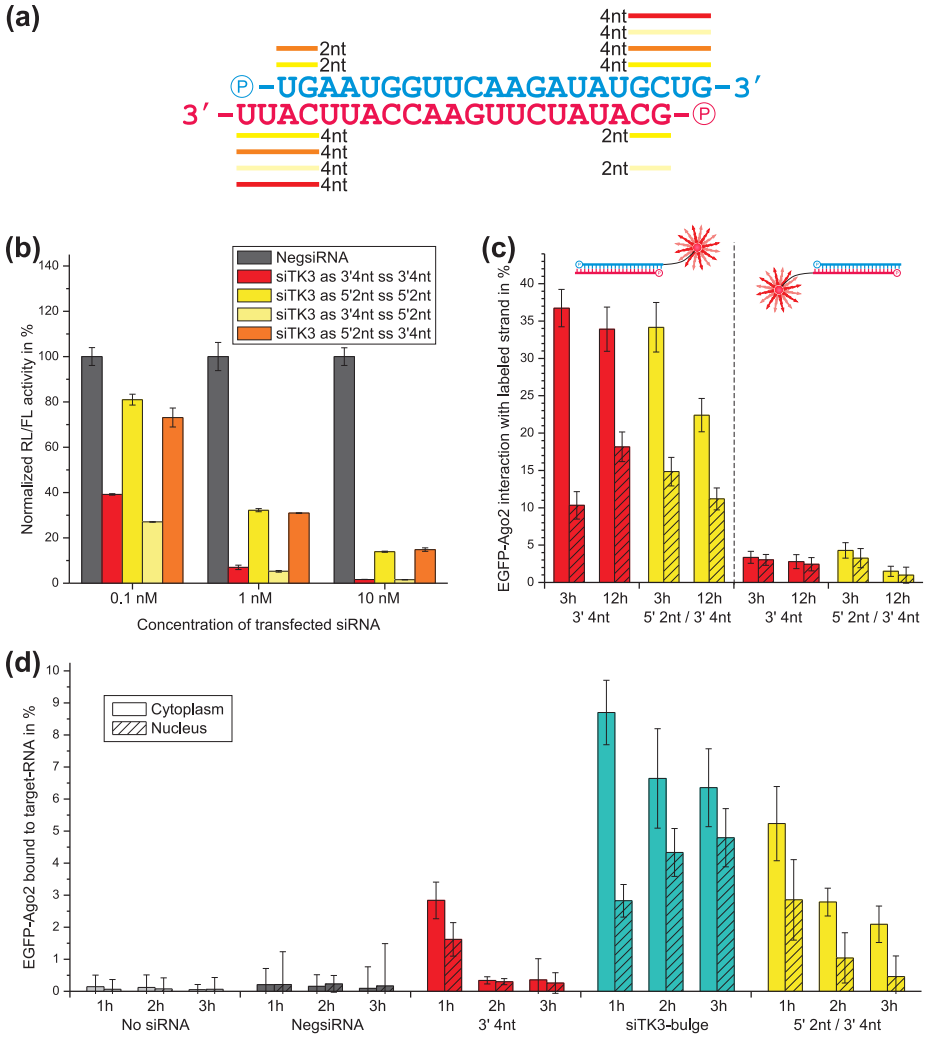

Figure 5.13: Silencing, loading, and target interaction of 5' end modified siRNA (**a**) Sequence of the used siTK3 with indication of the 2'-O-methyl modified parts. (**b**) Silencing activity of indicated amounts of 5' end 2'-O-methyl modified siRNA measured with a Dual-Luciferase Assay. As controls silencing of NegsiRNA and siTK3 is also shown. Data are represented as mean±SD. (**c**) Cross-correlation amplitudes between labeled strand and EGFP-Ago2 measured in the cytoplasm (empty bars) and the nucleus (striped bars), 3 h and 12 h after microinjection. The labeled strand is indicated by the cartoon. (**d**) Resulting cross-correlation amplitudes between target-RNA and RISC loaded with indicated modified siRNAs measured in the cytoplasm (empty bars) and the nucleus (striped bars), 1 h to 3 h after microinjection. Data are represented as mean±SEM.

bition measured in the silencing assay (Fig. 5.13(b)). The asymmetry of 5'-end modified siRNAs incorporation is not affected as passenger strand labeled duplex displayed comparable values to the control duplex (Fig. 5.13(c)).

For the elucidation of the impact of the 5'-end 2'-O-methyl modification on the target interaction the fluorescently labeled target-RNA was microinjected in 10G cells which were transfected with the 5'-end modified siTK3. Clearly an increased interaction between target-RNA and RISC that was loaded with 5'-end modified siTK3 compared to RISC loaded with the negative control (NegsiRNA) or the cleavage active 4 nt 3'-end modified siTK3 (3' 4 nt) (Fig. 5.13(d)) could be measured. The interaction levels were lower as for the siTK3-bulge positive control, but this can result from the destabilized interaction of the 5'-end modified guide strand to RISC. Nevertheless, the 2'-O-methyl modification on the 5'-end has an impact on the stability and cleavage activity of RISC, but does not interfere with the loading machinery and asymmetry of the duplex.

5.4.4 2'-O-methyl Modifications at Cleavage Site Have Only Minor Effects on Silencing Activity and Strand Separation

hAgo2 cleaves the passenger strand and the targeted mRNA between the two nucleotides which pair the 10th and 11th nucleotide of the guide strand, counted from the 5' end [299, 302]. Additionally it has been shown *in vitro* that 2'-O-methyl modifications can inhibit passenger strand cleavage and strand separation at position 9 of the passenger strand [247]. Therefore, the influence of 2'-O-methyl modifications at the cleavage site on RISC activity was studied. A siTK3 siRNA with 2'-O-methyl modifications at positions 9, 10, and 11 starting from the 5' end was created (Fig. 5.14(a)). In the dual luciferase silencing assay only a minor change of silencing activity of less than 8% for the double and the guide modified duplex could be detected (Fig. 5.14(b)). Within the accuracy of our FCCS-assay the internal modification had no effect on the siRNA-affinity to RISC

Figure 5.14 *(facing page)*: Silencing, loading, and target interaction of cleavage site 2'-O-methyl modified siRNAs (**a**) Sequence of the used siTK3 with indication of the 2'-O-methyl modified parts. (**b**) Silencing activity of indicated amounts of cleavage site modified siRNAs measured with a Dual-Luciferase Assay. As controls silencing of NegsiRNA and siTK3 is also shown. Data are represented as mean±SD. (**c**) Cross-correlation amplitudes between labeled strand and EGFP-Ago2 measured in the cytoplasm (empty bars) and the nucleus (striped bars), 3 h and 12 h after microinjection. The labeled strand is indicated by the cartoon. (**d**) Resulting cross-correlation amplitudes between target-RNA and RISC loaded with indicated modified siRNAs measured in the cytoplasm (empty bars) and the nucleus (striped bars), 1 h to 3 h after microinjection. Data are represented as mean±SEM.

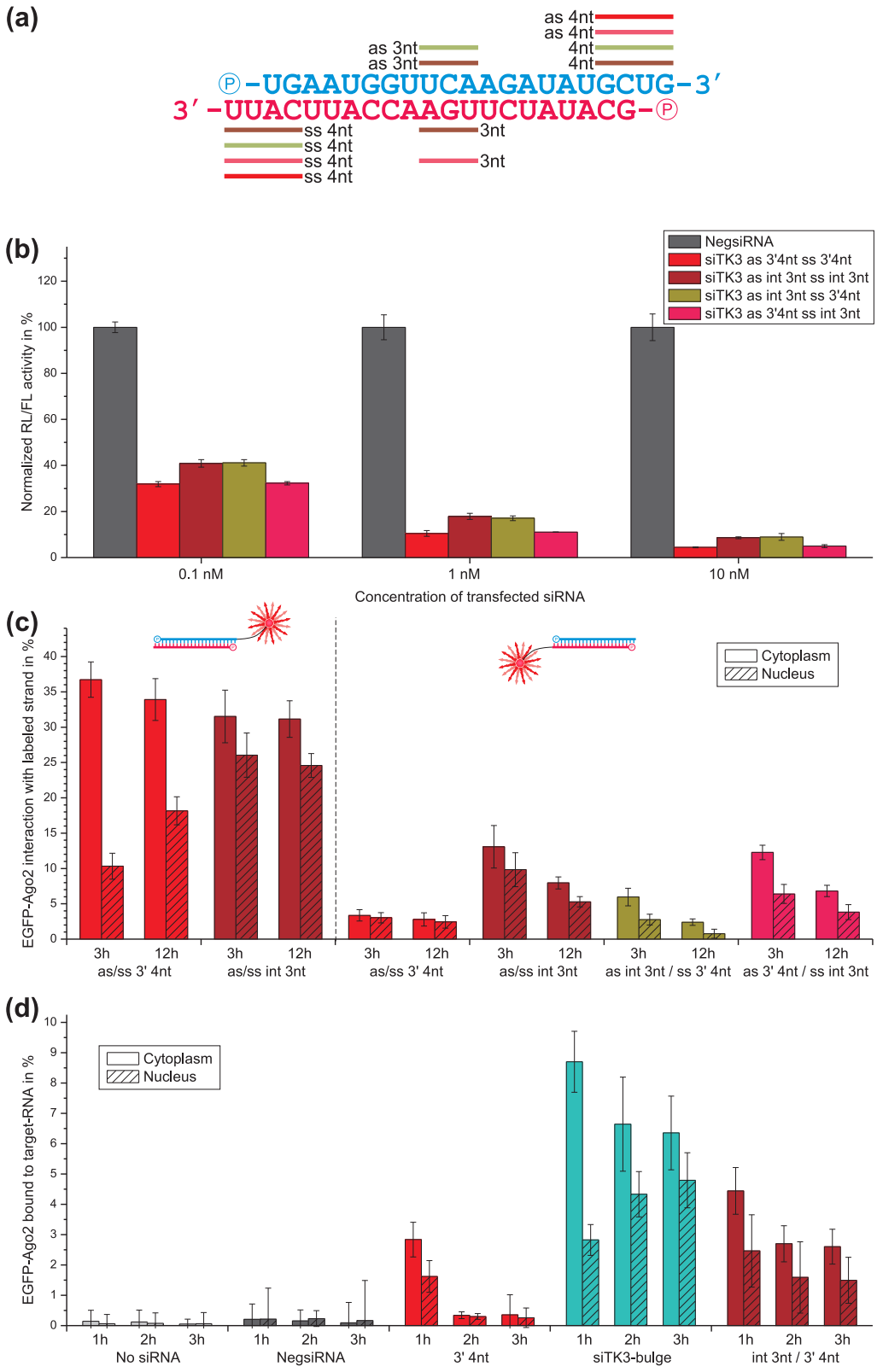
(a)
as 4nt
as 4nt
as 3nt
as 3nt
4nt
4nt
Ⓟ–UGAAUGGUUCAAGAUAUGCUG–3′
3′–UUACUUACCAAGUUCUAUACG–Ⓟ
ss 4nt
ss 4nt
ss 4nt
ss 4nt
3nt
3nt
(b)
NegsiRNA
siTK3 as 3'4nt ss 3'4nt
siTK3 as int 3nt ss int 3nt
siTK3 as int 3nt ss 3'4nt
siTK3 as 3'4nt ss int 3nt
Normalized RL/FL activity in %
0.1 nM
1 nM
10 nM
Concentration of transfected siRNA
(c)
Cytoplasm
Nucleus
EGFP-Ago2 interaction with labeled strand in %
3h 12h 3h 12h 3h 12h 3h 12h 3h 12h 3h 12h
as/ss 3' 4nt
as/ss int 3nt
as/ss 3' 4nt
as/ss int 3nt
as int 3nt / ss 3' 4nt
as 3' 4nt / ss int 3nt
(d)
Cytoplasm
Nucleus
EGFP-Ago2 bound to target-RNA in %
1h 2h 3h
No siRNA
NegsiRNA
3' 4nt
siTK3-bulge
int 3nt / 3' 4nt

and the asymmetric incorporation. However, increased interaction levels of labeled passenger strand with the dual modified, as well as the passenger strand modified, duplex compared to the siTK3-3'4nt duplex were detected (Fig. 5.14(c)). The modification on the guide strand only, had no effect on strand separation.

The interaction levels of RISC loaded with cleavage-site modified siRNA and the target-RNA were slightly increased compared to the cleavage active siTK3-3'4nt and lower in relation to the bulge forming siRNA (Fig. 5.14(d)).

Consistent with the moderate effects measured in the silencing assays the *in vivo* FCCS analysis detected only small inhibitory changes in strand separation and target interaction. Nevertheless, it also demonstrates the high sensitivity of the FCCS assays *in vivo*, as even small changes in silencing activity of less than 8% are clearly visible and allow for the clear detection of the individual inhibited steps.

5.4.5 Correlation Between Silencing Activity and *in vivo* Measured RISC-target-RNA-Interaction

So far, with decreasing silencing activity increased interaction levels between siRNA loaded RISC and target-RNA were detected. Therefore, the fraction of

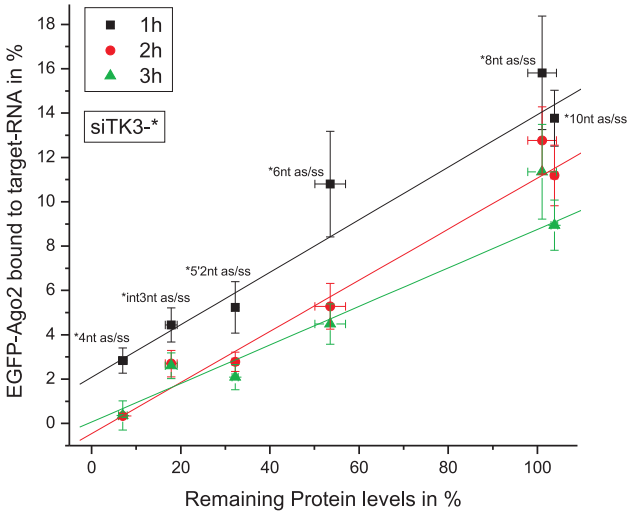

Figure 5.15: Correlation between silencing activity and target interaction. The levels of target-RNA bound to EGFP-Ago2 for different time points after microinjection (1 h: black squares, 2 h: red diamonds, 3 h: green triangles) are plotted against the silencing values obtained for different siRNAs at 1 nM concentration after 48 h.

RISC bound target-RNA vs. the silencing activity for 1, 2, and 3 h was plotted, to see if a correlation exists between silencing activity and target interaction (Fig. 5.15). Interestingly, a linear relationship between the silencing activity and RISC bound target-RNA at different time points was detected. By applying this assay, it is possible to calculate cleavage activities of modified siRNAs by the level of interaction between siRNA loaded RISC with their target-RNA. This plot points out that the internal modification increases the stability of the target-RNA-RISC complex compared to the 3' and 5' end modifications. However, the reduction of the slope might be due to degradation of the target-RNA with increasing incubation times or translocation into P-bodies.

5.5 Discussion

So far, initial steps of RISC formation occurring in the first 1-6 h after siRNA delivery were mainly inaccessible with conventional assays. To better understand the RNAi mechanism and the influence of introduced modifications on siRNAs, new *in vivo* assays are necessary, which are able to analyze RISC formation and target interactions in their initial and late phase. Several important parts of the RNAi mechanism could be analyzed *in vivo*, by the combination of an EGFP-Ago2 reporter cell line, the specific delivery of fluorescent RNAs via microinjection and FCCS. By the use of guide strand-labeled siRNA duplexes, RISC affinity, asymmetric incorporation and activated RISC stability could be studied. Whereas the use of passenger strand-labeled duplexes allowed the investigation of asymmetric incorporation and passenger strand removal. Target interaction and RISC-mediated target-RNA cleavage were studied by the transfection of reporter cells with unlabeled siRNAs, followed by the microinjection of fluorescently labeled target-RNA after an incubation period. This combination of specific RNA delivery with the high sensitive fluorescent technique of correlation spectroscopy, made it possible to study the influence of several differently 2'-O-methyl modified siRNAs onto RISC formation and target interactions *in vivo*.

The individual mechanistic effects of 2'-O-methyl modifications at different positions within siRNAs on RISC assembly and activity could be followed *in vivo*. It could be shown that 2'-O-methyl modifications at different positions within the siRNA lead to several ways of RISC activity inhibition. 2'-O-methyl modification were investigated, because phosphorothioate and 2'-fluoro modifications were incompatible with our *in vivo* FCCS assay due to intense photobleaching resulting from their strong non-specific affinity for cellular proteins and structures. This is consistent with the changed sub-cellular localization of phosphorothioate and 2'-fluoro modified duplexes reported in [367]. Therefore, such modified duplexes or single stranded phosphorothioate or 2'-fluoro modified RNAs cannot be investigated by standard FCS/FCCS *in vivo*. Furthermore, 2'-O-methyl nucleotides are

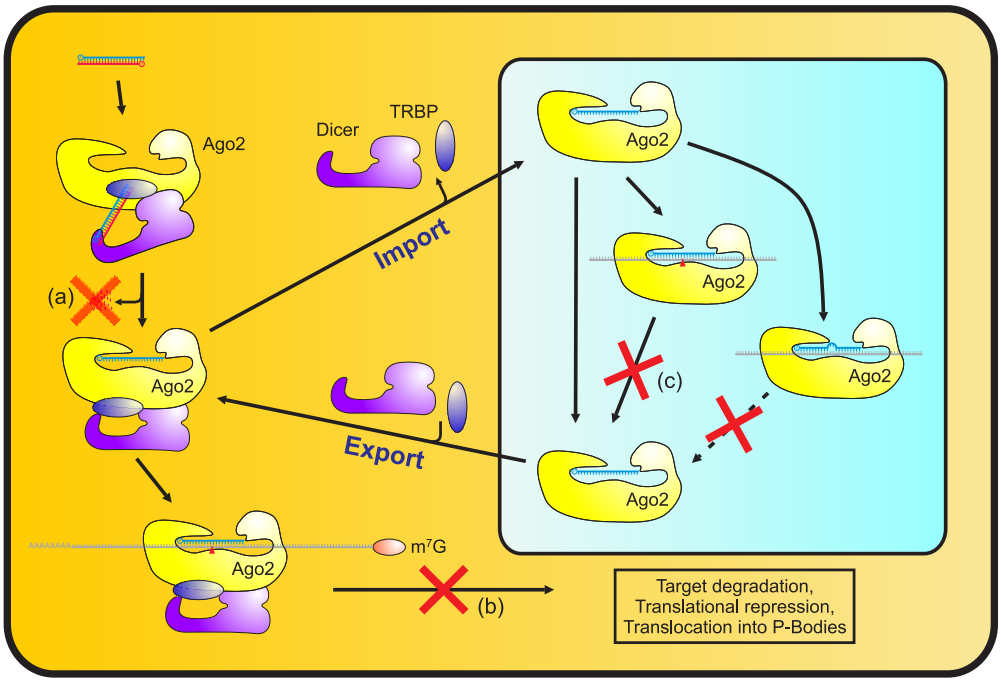

Figure 5.16: Inhibition of RNAi mechanism by 3' end modified siRNAs. (a) Inhibited passenger strand cleavage lead to reduced passenger strand removal. This can be circumvented by a bypass mechanism on longer time scales. Inhibited target-RNA cleavage lead to stable RISC target-RNA interaction in the cytoplasm (b) and nucleus (c).

very interesting siRNA modifications, as this modification represents a naturally occurring modification in transfer and ribosomal RNAs and can be used to specifically increase the lifetime, specificity, and potency of siRNAs, but also to inhibit RNA mediated gene silencing.

Standard dual luciferase assays were used to investigate the effect of increasing amounts of 2'-O-methyl modifications on the 3'-end. In these assays, it was found that four 2'-O-methyl nucleotides lead to increased silencing efficiency after 48 hours, whereas six 2'-O-methyl modifications strongly inhibited, and eight to ten 2'-O-methyl insertions completely abolished gene silencing. This is consistent with previous reports demonstrating the inhibition of fully or highly 2'-O-methyl modified siRNAs [298, 310, 376–379].

For the first time, the mechanism of 2'-O-methyl mediated gene silencing inhibition on the 3'-end could be unraveled. By applying FCCS *in vivo*, it could be shown that neither the affinity nor the asymmetry of guide strand incorporation is affected. By contrast, it could be demonstrated that the removal of the passenger strand is strongly inhibited, a step that is strictly required for RISC activation and maturation (Fig. 5.16(a)). Furthermore, the inhibitory effect on passenger

strand release only occurs when 2'-O-methyl modified nucleotides are present on the guide strand. Although it was demonstrated that mainly the cleavage activity of RISC is affected, which is needed for efficient passenger strand removal, we could detect passenger strand release of up to 50% of bound siRNA after 12 h of siRNA supply. This indicates that a less efficient bypass mechanism exists without passenger strand cleavage leading to guide strand loaded RISC (activated RISC) [248, 253]. This demonstrates the advantage of the FCCS assay that allows the measurement of RISC assembly at early and late stages after siRNA supply.

It could be shown that RISC loaded with the cleavage impaired 2'-O-methyl modified guide strands were still capable of recognizing and binding of their target-RNA. Due to the impaired targetRNA cleavage a stable miRNA-like interaction between RISC and target-RNA is formed (Fig. 5.16(b,c)). Surprisingly, they associate to higher extend with the target-RNA compared to a bulge forming guide strand which also inhibits target-RNA cleavage. Most probably this results from a stabilization effect of the 2'-O-methyl modification on the RISC target interaction caused either by the increased affinity due to the complete hybridization of the guide-target-RNA duplex or by protection of the guide strand against nucleases. Although it has been already shown that 2'-O-methyl modifications inhibits target-RNA cleavage in vitro, at that time it could not be excluded that passenger strand release was also affected or sufficient [298].

The silencing inhibition of siRNAs with 6-10 2'-O-methyl modified nucleotides from the 3'end is in agreement with the results from Wang et al. [291], who showed that hAgo2 mediated cleavage only occurs with guide/target-RNA duplexes larger than 16 nt. Therefore, the 3'-RNA region from 15-21 of the guide strand seems to be important for the transition into or stabilization of the active confirmation which can be inhibited by 2'-O-methyl modified nucleotides.

The insertion of two 2'-O-methyl modified nucleotides on the 5'-end inhibited gene silencing activity if present on the guide strand. It could be demonstrated that 3 h after siRNA supply, resembling the early stages of RISC assembly, neither the affinity nor asymmetry was affected. In contrast to the 3'-end modification, the 5'-end 2'-O-methyl modified nucleotides did not interfere with strand separation. Interestingly, after 12 h a strong decrease in loaded RISC levels was detected, indicating that the two 2'-O-methyl modified nucleotides on the 5'-end somehow destabilize the RISC-guide strand complex. Additionally it was shown that 5'-end modification lead to increased RISC target-RNA interaction levels, pointing out a reduced target-RNA cleavage efficiency.

It seems to be possible that 2'-O-methyl modifications on the 5'-end leads to reduced hAgo2 guide strand stability similar to the destabilization with a guide strand lacking the 5'-phosphate [269]. This would also explain why passenger strand removal is unaffected, whereas target-RNA cleavage seems to be less efficient. Nevertheless, the affect of 2'-O-methyl modified nucleotides on the 5'-end could be sequence dependent as other groups reported also no inhibitory function

of one to two 2'-O-methyl modified nucleotides on the 5'-end [313, 376].

Surprisingly only marginal effects could be detected for 2'-O-methyl modified nucleotides at the cleavage site. While the bulge forming siRNA was cleavage incompetent, for the siRNA containing three 2'-O-methyl modified nucleotides at the position 9, 10, and 11 a reduction of silencing activity of only 8 % for the double and guide modified duplex could be detected in our standard dual luciferase assay. Nevertheless minor reductions in strand separation could be detected by the *in vivo* FCCS loading assay, which is in agreement with a previous report [247] showing passenger strand cleavage inhibition for a passenger strand with a 2'-O-methyl modification on position nine. The fact that only minor inhibition of passenger strand release was measured might be due to the fact that Leuschner et al. [247] used a purified minimal RISC, which almost represents the single hAgo2 protein alone, whereas here FCCS was measured *in vivo* providing optimal siRNA processing conditions. Even the silencing activity was decreased by only 8 % slightly higher levels of RISC target-RNA interaction could be detected, which are indicative for slightly inhibited target-RNA cleavage process.

5.6 Conclusion

The presented novel *in vivo* FCCS assays are very well suited to investigate the RNAi mechanism. The first assay allowed the investigation of the individual steps of RISC assembly, especially the loading of the siRNA duplex, the removal of the passenger strand, and the stability of the guide strand-RISC interaction. To study the very important step of target cleavage, the second assay investigated the interaction of activated RISC with a targeted mRNA mimic. With this assay, a direct correlation between cleavage activity and target interaction could be shown, which can also be used to determine cleavage properties of used guide RNAs, thereby allowing for multi-parameter measurements.

Additionally, the influence of 2'-O-methyl modifications at various positions on RISC assembly and activity was studied. FCCS measurements with modified siRNAs, that inhibit silencing, revealed that the main inhibited mechanism is the cleavage of the targeted RNA. Additionally it was unraveled that the release of the passenger strand is inhibited, mainly due to the cleavage inhibition of the passenger strand. But here strong decrease of the interaction between RISC and the passenger strand was seen with time, pointing to a less efficient bypass mechanism. It could be shown that 2'-O-methyl modified 3'-end siRNAs with up to 8-10 nt can be used to mimic miRNA-like interactions of RISC with its target-RNA, increasing the stability of the RISC-target-RNA-complex. These results can lead to the development of a new type of therapeutic small RNAs, as they allow the application of miRNA-like duplexes with increased affinities to their target-RNA.

6 Conclusion and Outlook

This dissertation focusses on the utilization of fluorescence cross-correlation spectroscopy (FCCS) as sensitive and versatile tool to elucidate the flow profile inside a micropump and to study the RNA interference (RNAi) mechanism *in vivo*.

A micropump using the electrohydrodynamical principle displays a complex flow profile, which is not resolvable by common techniques. Additionally, dielectrophoretic forces act on particles larger than 50 nm to 100 nm, preventing the elucidation of the pure electrohydrodynamic forces. Here, the flow profile of such a pump was mapped by two-focus FCCS (2f-FCCS) using small (20 nm) quantum dots as fluorescent particles. The combination of the flow velocity map, resolved by 2f-FCCS, with the results from the bead imaging allowed the reconstruction of a complex flow pattern, consisting of two vortices of different size and opposite direction of rotation. This flow pattern explained the observed complex particle trajectories in the force field and the accumulation of particles in well-defined regions above the microelectrode array. The high precision of 2f-FCCS in measuring flow velocities with small fluorescent particles made it possible to separate the electrohydrodynamic forces acting on the solvent from the dielectrophoretic forces acting on larger particles. This allowed the elucidation of the correct flow pattern inside the micropump. In the future, an optimization of the complex flow profile, will increase the efficiency of the electrohydrodynamical principle in handling small fluid volumes. For the use as a pump the optimization process should lead to a elimination of the vortices and generate a more laminar flow profile in the active region. The promotion of particle accumulation could also be an aim of optimization. This would allow concentration of particle suspensions. For these possible optimization attempts, 2f-FCCS will be useful techniques to monitor the flow patterns.

In the second part of this thesis, the mechanism of RNAi was studied by dual-color FCCS using two novel *in vivo* FCCS assays. The first assay allowed the investigation of the individual steps of RNA-induced silencing complex (RISC) assembly, especially the loading of the short interfering RNA (siRNA) duplex, the removal of the passenger strand, and the stability of the guide strand-RISC interaction. To study the very important step of target cleavage, the second assay investigated the interaction of activated RISC with a targeted mRNA mimic. Using these assays to study differently 2'-O-methyl modified siRNAs resolved that most of the silencing inhibited siRNAs displayed an inhibited passenger strand removal and an inhibited target-RNA cleavage. It could be shown that the here presented novel *in vivo* FCCS assays are very well suited to elucidate, which single

step of the RNAi machinery assembly and activity is inhibited. This will help to develop modified siRNAs with increased stability and full activity in the future. These assays can also be used to optimize modifications which feature different benefits, like the addition of cholesterol, which increases the cellular uptake of siRNAs. In a more general view, the here used principle of studying the interaction between a labeled protein and labeled DNA or RNA molecules could be used to unravel other biological questions, such as the detailed mechanisms of mRNA splicing, DNA repair enzymes, or the role of double-stranded oligo-nucleotides in auto-immune diseases.

Symbols and Abbreviations

Abbreviations

2f-FCCS	two-focus FCCS
agRNA	antigene RNA
APD	avalanche photodiode
bp	base pair
cw	continuous wave
DNA	deoxyribonucleic acid
dsRBD	dsRNA binding domain
dsRNA	double stranded RNA
EGFP	enhanced GFP
FCCS	fluorescence cross-correlation spectroscopy (mostly dual-color FCCS)
FCS	fluorescence correlation spectroscopy
FBS	fetal bovine serum (fetal calf serum)
GFP	green fluorescent protein
ICS	image correlation spectroscopy
ISC	intersystem crossing
LoC	Lab-on-Chip
LSM	laser scanning microscopy
miRNA	micro RNA
mRNA	messenger RNA
µTAS	micro Total Analysis System
NA	numerical aperture
nt	nucleotide
PAGE	polyacrylamide gel electrophoresis
P-body	processing body
PIE	pulsed interleaved excitation
PTGS	post-transcriptional gene silencing
piRNA	Piwi-interacting RNA
pri-miRNA	primary miRNA
pre-miRNA	precursor miRNA
RICS	raster image correlation spectroscopy
nRISC	nuclear RISC
cRISC	cytoplasmic RISC

RISC	RNA-induced silencing complex
RITS	RNA-induced transcriptional silencing complex
RLC	RISC loading complex
RNA	ribonucleic acid
RNAi	RNA interference
RNase	Ribonuclease
SD	standard deviation
SEM	standard error of mean
siRNA	short interfering RNA
TGS	transcriptional gene silencing
UTR	untranslated region
WGA	wheat germ agglutinin

Symbols and Units

α	angle between the flow velocity and the vector between the two foci
B	uncorrelated background signal
β	relative crosstalk from the 'green' fluorophore into the 'red' channel
$C(\vec{r}, t)$	concentration
D	diffusion coefficient
Da	Dalton ($1\,\mathrm{Da} = 1\,\mathrm{u} = 1.660538782 \cdot 10^{-27}\,\mathrm{kg}$)
δ	fluctuations of
$\vec{E}$	electric field
ε	permittivity
η	molecular brightness
η_m	viscosity of medium
F	fluorescence intensity (usually the measured one)
$\tilde{F}$	emitted fluorescence intensity
f_i	fraction
$\vec{f}_{\mathrm{el}}$	electric force per volume
f_{B}	bleaching fraction
f_{T}	triplet fraction
$G(\tau)$	correlation curve or model function
$\tilde{G}(\tau)$	corrected correlation curve
γ	relative crosstalk from the 'red' fluorophore into the 'green' channel
$I_{\mathrm{ex}}(\vec{r})$	excitation intensity profile
$\vec{j}$	current density
K	equilibrium constants
k	rate constants

k_B	Boltzmann constant
k_{PB}	photobleaching rate
κ	detector efficiency
Λ_i	brightness weighting factor
$\langle N \rangle$	mean particle number
ω_0	lateral radius of the detection volume
p_k	model parameter
φ	quantum yield
$\Phi(\vec{r}, \vec{r}', \tau)$	concentration correlation function
R	distance (between both foci)
R_0	hydrodynamic radius
$\vec{r}$	position
res	residual
ρ	density of mass
ρ_{el}	electric volume charge
S	structure parameter
$S(\vec{r})$	normalized collection efficiency function
σ	conductivity
σ	standard deviation
σ_{ex}	extinction coefficient
τ	lag time
τ_{D}	diffusion time
τ_b	relaxation time
τ_{ch}	charge relaxation time
τ_{T}	triplet relaxation time
T	temperature
T	reaction matrix (constructed from chemical rate coefficients and equilibrium concentrations of the reactants involved)
t	time
V	(integration) volume
V_{eff}	effective volume
$\vec{v}(\vec{r}, t)$	flow velocity
$W(\vec{r})$	molecule detection function (normalized)
w	weight
z_0	half axial extension of the detection volume

Bibliography

[1] Douglas Magde, Elliot Elson and W. W. Webb. *Thermodynamic Fluctuations in a Reacting System - Measurement by Fluorescence Correlation Spectroscopy.* Phys. Rev. Lett. **29**(11), 705–708 (1972).

[2] E.L. Elson and D. Magde. *Fluorescence Correlation Spectroscopy. I. Conceptual Basis and Theory.* Biopolymers **13**, 1–27 (1974).

[3] D. Magde, E. L. Elson and W. W. Webb. *Fluorescence correlation spectroscopy. II. An experimental realization.* Biopolymers **13**(1), 29–61 (1974).

[4] R. Rigler, Ü. Mets, J. Widengren and P. Kask. *Fluorescence correlation spectroscopy with high count rate and low background: analysis of translational diffusion.* Eur. Biophys. J. **22**, 169–175 (1993).

[5] Kirsten Bacia, Sally A. Kim and Petra Schwille. *Fluorescence cross-correlation spectroscopy in living cells.* Nat. Methods **3**(2), 83–89 (2006).

[6] Elke Haustein and Petra Schwille. *Fluorescence Correlation Spectroscopy: Novel Variations of an Established Technique.* Annu. Rev. Biophys. Biomol. Struct. **36**, 151–169 (2007).

[7] E.P. Petrov and P. Schwille. *Standardization and Quality Assurance in Fluorescence Measurements II: Bioanalytical and Biomedical Applications*, volume 6 of *Springer Series on Fluorescence*, chapter State of the Art and Novel Trends in Fluorescence Correlation Spectroscopy, pages 145–197. Springer, Berlin Heidelberg New York, 2008.

[8] J. Rička and T. Binkert. *Direct measurement of a distinct correlation-function by fluorescence cross-correlation.* Phys. Rev. A **39**(5), 2646–2652 (1989).

[9] M. Eigen and R. Rigler. *Sorting single molecules: application to diagnostics and evolutionary biotechnology.* Proc. Natl. Acad. Sci. USA **91**(13), 5740–5747 (1994).

[10] P. Schwille, F. J. Meyer-Almes and R. Rigler. *Dual-Color Fluorescence Cross-Correlation Spectroscopy for Multicomponent Diffusional Analysis in Solution.* Biophys. J. **72**(4), 1878–1886 (1997).

[11] Ling Chin Hwang, Michael Gösch, Theo Lasser and Thorsten Wohland. *Simultaneous Multicolor Fluorescence Cross-Correlation Spectroscopy to Detect Higher Order Molecular Interactions Using Single Wavelength Laser Excitation.* Biophys. J. **91**(2), 715–727 (2006).

[12] Markus Burkhardt, Katrin G Heinze and Petra Schwille. *Four-color fluorescence correlation spectroscopy realized in a grating-based detection platform.* Opt. Lett. **30**(17), 2266–2268 (2005).

[13] Ling Chin Hwang, Marcel Leutenegger, Michael Gösch, Theo Lasser, Per Rigler, Wolfgang Meier and Thorsten Wohland. *Prism-based multicolor fluorescence correlation spectrometer.* Opt. Lett. **31**(9), 1310–1312 (2006).

[14] M. Brinkmeier, K. Dörre, J. Stephan and M. Eigen. *Two-Beam Cross Correlation: A Method To Characterize Transport Phenomena in Micrometer-Sized Structures.* Anal. Chem. **71**(3), 609–616 (1999).

[15] Rodolphe Jaffiol, Yoann Blancquaert, Antoine Delon and Jacques Derouard. *Spatial fluorescence cross-correlation spectroscopy.* Appl. Opt. **45**(6), 1225–1235 (2006).

[16] Thomas Dertinger, Victor Pacheco, Iris von der Hocht, Rudolf Hartmann, Ingo Gregor and Jörg Enderlein. *Two-Focus Fluorescence Correlation Spectroscopy: A New Tool for Accurate and Absolute Diffusion Measurements.* ChemPhysChem **8**(3), 433–443 (2007).

[17] Thomas Dertinger, Anastasia Loman, Benjamin Ewers, Claus B. Müller, Benedikt Krämer and Jörg Enderlein. *The optics and performance of dual-focus fluorescence correlation spectroscopy.* Opt. Express **16**(19), 14353–14368 (2008).

[18] K. M. Berland, P. T. So and E. Gratton. *Two-Photon Fluorescence Correlation Spectroscopy: Method and Application to the Intracellular Environment.* Biophys. J. **68**(2), 694–701 (1995).

[19] P. Schwille, U. Haupts, S. Maiti and W. W. Webb. *Molecular Dynamics in Living Cells Observed by Fluorescence Correlation Spectroscopy with One- and Two-Photon Excitation.* Biophys. J. **77**(4), 2251–2265 (1999).

[20] K.G. Heinze, A. Koltermann and P. Schwille. *Simultaneous two-photon excitation of distinct labels for dual-color fluorescence crosscorrelation analysis.* Proc. Natl. Acad. Sci. USA **97**(19), 10377–10382 (2000).

[21] N. O. Petersen. *Scanning fluorescence correlation spectroscopy I. Theory and simulation of aggregation measurements.* Biophys. J. **49**(4), 809–815 (1986).

[22] Jonas Ries and Petra Schwille. *Studying Slow Membrane Dynamics with Continuous Wave Scanning Fluorescence Correlation Spectroscopy.* Biophys. J. **91**(5), 1915–1924 (2006).

[23] Jonas Ries and Petra Schwille. *New concepts for fluorescence correlation spectroscopy on membranes.* Phys. Chem. Chem. Phys. **10**(24), 3487–3497 (2008).

[24] Jonas Ries, Salvatore Chiantia and Petra Schwille. *Accurate Determination of Membrane Dynamics with Line-Scan FCS.* Biophys J **96**(5), 1999–2008 (2009).

[25] Qiaoqiao Ruan, Melanie A. Cheng, Moshe Levi, Enrico Gratton and William W. Mantulin. *Spatial-Temporal Studies of Membrane Dynamics: Scanning Fluorescence Correlation Spectroscopy (SFCS).* Biophys. J. **87**(2), 1260–1267 (2004).

[26] Joseph P. Skinner, Yan Chen and Joachim D. Müller. *Position-Sensitive Scanning Fluorescence Correlation Spectroscopy.* Biophys. J. **89**(2), 1288–1301 (2005).

[27] Dmitri Satsoura, Brian Leber, David W. Andrews and Cécile Fradin. *Circumvention of Fluorophore Photobleaching in Fluorescence Fluctuation Experiments: a Beam Scanning Approach.* ChemPhysChem **8**(6), 834–848 (2007).

[28] Zdenek Petrásek, Carsten Hoege, Alireza Mashaghi, Thomas Ohrt, Anthony A. Hyman and Petra Schwille. *Characterization of Protein Dynamics in Asymmetric Cell Division by Scanning Fluorescence Correlation Spectroscopy.* Biophys. J. **95**(11), 5476–5486 (2008).

[29] Nancy L. Thompson and Bridgett L. Steele. *Total internal reflection with fluorescence correlation spectroscopy.* Nat. Protoc. **2**(4), 878–890 (2007).

[30] Nancy L. Thompson, Xiang Wang and Punya Navaratnarajah. *Total internal reflection with fluorescence correlation spectroscopy: Applications to substrate-supported planar membranes.* J. Struct. Biol. (2009).

[31] N. L. Thompson. *Surface Binding Rates of Nonfluorescent Molecules May Be Obtained by Total Internal Reflection with Fluorescence Correlation Spectroscopy.* Biophys. J. **38**(3), 327–329 (1982).

[32] N. L. Thompson and D. Axelrod. *Immunoglobulin Surface-Binding Kinetics Studied by Total Internal Reflection with Fluorescence Correlation Spectroscopy.* Biophys. J. **43**(1), 103–114 (1983).

[33] T. E. Starr and N. L. Thompson. *Total Internal Reflection with Fluorescence Correlation Spectroscopy: Combined Surface Reaction and Solution Diffusion.* Biophys. J. **80**(3), 1575–1584 (2001).

[34] T.E. Starr and N.L. Thompson. *Local Diffusion and Concentration of IgG near Planar Membranes: Measurement by Total Internal Reflection with Fluorescence Correlation Spectroscopy.* J. Phys. Chem. B **106**(9), 2365–2371 (2002).

[35] Alena M. Lieto, Randall C. Cush and Nancy L. Thompson. *Ligand-Receptor Kinetics Measured by Total Internal Reflection with Fluorescence Correlation Spectroscopy.* Biophys. J. **85**(5), 3294–3302 (2003).

[36] A.L. Stout and D. Axelrod. *Evanescent field excitation of fluorescence by epi-illumination microscopy.* Appl. Optics **28**(24), 5237–5242 (1989).

[37] Kai Hassler, Tiemo Anhut, Rudolf Rigler, Michael Gösch and Theo Lasser. *High Count Rates with Total Internal Reflection Fluorescence Correlation Spectroscopy.* Biophys. J. **88**(1), L01–L03 (2005).

[38] K. Hassler, M. Leutenegger, P. Rigler, R. Rao, R. Rigler, M. Gosch and T. Lasser. *Total internal reflection fluorescence correlation spectroscopy (TIR-FCS) with low background and high count-rate per molecule.* Optics Express **13**(19), 7415–7423 (2005).

[39] Marcel Leutenegger, Hans Blom, Jerker Widengren, Christian Eggeling, Michael Gösch, Rainer A. Leitgeb and Theo Lasser. *Dual-color total internal reflection fluorescence cross-correlation spectroscopy.* J. Biomed. Opt. **11**(4), 040502 (2006).

[40] C. Zander, M. Sauer, K. H. Drexhage, D. S. Ko, A. Schulz, J. Wolfrum, L. Brand, C. Eggeling and C. A. M. Seidel. *Detection and characterization of single molecules in aqueous solution.* Appl. Phys. B **63**(5), 517–523 (1996).

[41] L. Brand, C. Eggeling, C. Zander, K. H. Drexhage and C. A. M. Seidel. *Single-Molecule Identification of Coumarin-120 by Time-Resolved Fluorescence Detection: Comparison of One- and Two-Photon Excitation in Solution.* J. Phys. Chem. A **101**(24), 4313–4321 (1997).

[42] D. C. Lamb, A. Schenk, C. Röcker, C. Scalfi-Happ and G. U. Nienhaus. *Sensitivity Enhancement in Fluorescence Correlation Spectroscopy of Multiple Species Using Time-Gated Detection.* Biophys. J. **79**(2), 1129–1138 (2000).

[43] C. Eggeling, S. Berger, L. Brand, J. R. Fries, J. Schaffer, A. Volkmer and C. A. Seidel. *Data registration and selective single-molecule analysis using multi-parameter fluorescence detection.* J. Biotechnol. **86**(3), 163–180 (2001).

[44] D. C. Lamb, B. K. Müller and C. Bräuchle. *Enhancing the Sensitivity of Fluorescence Correlation Spectroscopy by Using Time-Correlated Single Photon Counting.* Curr. Pharm. Biotechnol. **6**(5), 405–414 (2005).

[45] S. Felekyan, R. Kuhnemuth, V. Kudryavtsev, C. Sandhagen, W. Becker and C. A. M. Seidel. *Full correlation from picoseconds to seconds by time-resolved and time-correlated single photon detection.* Rev. Sci. Instrum. **76**(8), 083104 (2005).

[46] Wajih Al-Soufi, Belén Reija, Mercedes Novo, Suren Felekyan, Ralf Kühnemuth and Claus A. M. Seidel. *Fluorescence Correlation Spectroscopy, a Tool to Investigate Supramolecular Dynamics: Inclusion Complexes of Pyronines with Cyclodextrin.* J. Am. Chem. Soc. **127**(24), 8775–8784 (2005).

[47] M. Bohmer, M. Wahl, H. J. Rahn, R. Erdmann and J. Enderlein. *Time-resolved fluorescence correlation spectroscopy.* Chem. Phys. Lett. **353**(5-6), 439–445 (2002).

[48] Y. Chen, J. D. Müller, P. T. So and E. Gratton. *The Photon Counting Histogram in Fluorescence Fluctuation Spectroscopy.* Biophys. J. **77**(1), 553–567 (1999).

[49] J. D. Müller, Y. Chen and E. Gratton. *Resolving Heterogeneity on the Single Molecular Level with the Photon-Counting Histogram.* Biophys. J. **78**(1), 474–486 (2000).

[50] P. Kask, K. Palo, D. Ullmann and K. Gall. *Fluorescence-intensity distribution analysis and its application in biomolecular detection technology.* Proc. Natl. Acad. Sci. USA **96**(24), 13756–13761 (1999).

[51] P. Kask, K. Palo, N. Fay, L. Brand, U. Mets, D. Ullmann, J. Jungmann, J. Pschorr and K. Gall. *Two-dimensional fluorescence intensity distribution analysis: theory and applications.* Biophys J **78**(4), 1703–1713 (2000).

[52] K. Palo, U. Mets, S. Jäger, P. Kask and K. Gall. *Fluorescence Intensity Multiple Distributions Analysis: Concurrent Determination of Diffusion Times and Molecular Brightness.* Biophys. J. **79**(6), 2858–2866 (2000).

[53] Yan Chen, Mohac Tekmen, Lindsey Hillesheim, Joseph Skinner, Bin Wu and Joachim D. Müller. *Dual-Color Photon-Counting Histogram.* Biophys. J. **88**(3), 2177–2192 (2005).

[54] N. O. Petersen, P. L. Höddelius, P. W. Wiseman, O. Seger and K. E. Magnusson. *Quantitation of membrane receptor distributions by image correlation spectroscopy: concept and application.* Biophys. J. **65**(3), 1135–1146 (1993).

[55] P. W. Wiseman and N. O. Petersen. *Image Correlation Spectroscopy. II. Optimization for Ultrasensitive Detection of Preexisting Platelet-Derived Growth Factor-β Receptor Oligomers on Intact Cells.* Biophys. J. **76**(2), 963–977 (1999).

[56] P. W. Wiseman, J. A. Squier, M. H. Ellisman and K. R. Wilson. *Two-photon image correlation spectroscopy and image cross-correlation spectroscopy.* J. Microsc. **200**(Pt 1), 14–25 (2000).

[57] Benedict Hebert, Santiago Costantino and Paul W. Wiseman. *Spatiotemporal Image Correlation Spectroscopy (STICS) Theory, Verification, and Application to Protein Velocity Mapping in Living CHO Cells.* Biophys. J. **88**(5), 3601–3614 (2005).

[58] Paul W. Wiseman, Claire M. Brown, Donna J. Webb, Benedict Hebert, Natalie L. Johnson, Jeff A. Squier, Mark H. Ellisman and A. F. Horwitz. *Spatial mapping of integrin interactions and dynamics during cell migration by Image Correlation Microscopy.* J. Cell Sci. **117**(Pt 23), 5521–5534 (2004).

[59] Michelle A. Digman, Claire M. Brown, Parijat Sengupta, Paul W. Wiseman, Alan R. Horwitz and Enrico Gratton. *Measuring Fast Dynamics in Solutions and Cells with a Laser Scanning Microscope.* Biophys. J. **89**(2), 1317–1327 (2005).

[60] *Organic Semiconductor World.* www.orgworld.de, 2009.

[61] *Olympus Microscopy Resource Center: Jablonski Energy Diagram.* http://www.olympusmicro.com/primer/java/jablonski/jabintro/index.html, 2009.

[62] *Structural formular of Alexa Fluor 488 carboxylic acid, succinimidyl ester (A20000, Invitrogen).* http://www.invitrogen.com/site/us/en/home/support/Product-Technical-Resources/Product-Structures.-20000.html, 2009.

[63] *Structural formular of Cy5.* http://en.wikipedia.org/wiki/Cyanine, 2009.

[64] *GFP crystal structure.* http://en.wikipedia.org/wiki/Green_fluorescent_protein, 2009.

[65] O. Shimomura, F. H. Johnson and Y. Saiga. *Extraction, Purification and Properties of Aequorin, a Bioluminescent Protein from the Luminous Hydromedusan, Aequorea.* J. Cell. Comp. Physiol. **59**(3), 223–239 (1962).

[66] D. C. Prasher, V. K. Eckenrode, W. W. Ward, F. G. Prendergast and M. J. Cormier. *Primary structure of the Aequorea victoria green-fluorescent protein.* Gene **111**(2), 229–233 (1992).

[67] M. Chalfie, Y. Tu, G. Euskirchen, W.W. Ward and D.C. Prasher. *Green Flourescent Protein as a Marker for Gene Expression.* Science **263**(5148), 802–805 (1994).

[68] M. Ormö, A. B. Cubitt, K. Kallio, L. A. Gross, R. Y. Tsien and S. J. Remington. *Crystal structure of the Aequorea victoria green fluorescent protein.* Science **273**(5280), 1392–1395 (1996).

[69] F. Yang, L. G. Moss and G. N. Phillips. *The molecular structure of green fluorescent protein.* Nature Biotechnology **14**(10), 1246–1251 (1996).

[70] R.Y. Tsien. *The green fluorescent protein.* Annu Rev Biochem **67**, 509–544 (1998).

[71] M. V. Matz, A. F. Fradkov, Y. A. Labas, A. P. Savitsky, A. G. Zaraisky, M. L. Markelov and S. A. Lukyanov. *Fluorescent proteins from nonbioluminescent Anthozoa species.* Nat. Biotechnol. **17**(10), 969–973 (1999).

[72] G. S. Baird, D. A. Zacharias and R. Y. Tsien. *Biochemistry, mutagenesis, and oligomerization of DsRed, a red fluorescent protein from coral.* Proc. Natl. Acad. Sci. USA **97**(22), 11984–11989 (2000).

[73] Robert E. Campbell, Oded Tour, Amy E. Palmer, Paul A. Steinbach, Geoffrey S. Baird, David A. Zacharias and Roger Y. Tsien. *A monomeric red fluorescent protein.* Proc. Natl. Acad. Sci. USA **99**(12), 7877–7882 (2002).

[74] Nathan C. Shaner, Robert E. Campbell, Paul A. Steinbach, Ben N. G. Giepmans, Amy E. Palmer and Roger Y. Tsien. *Improved monomeric red, orange and yellow fluorescent proteins derived from Discosoma sp. red fluorescent protein.* Nat. Biotechnol. **22**(12), 1567–1572 (2004).

[75] Nathan C. Shaner, Paul A. Steinbach and Roger Y. Tsien. *A guide to choosing fluorescent proteins.* Nat. Methods **2**(12), 905–909 (2005).

[76] Ekaterina M. Merzlyak, Joachim Goedhart, Dmitry Shcherbo, Mariya E. Bulina, Aleksandr S. Shcheglov, Arkady F. Fradkov, Anna Gaintzeva, Konstantin A. Lukyanov, Sergey Lukyanov, Theodorus W. J. Gadella and Dmitriy M. Chudakov. *Bright monomeric red fluorescent protein with an extended fluorescence lifetime.* Nat. Methods **4**(7), 555–557 (2007).

[77] Nathan C. Shaner, Michael Z. Lin, Michael R. McKeown, Paul A. Steinbach, Kristin L. Hazelwood, Michael W. Davidson and Roger Y. Tsien. *Improving the photostability of bright monomeric orange and red fluorescent proteins.* Nat. Methods **5**(6), 545–551 (2008).

[78] Takako Kogure, Satoshi Karasawa, Toshio Araki, Kenta Saito, Masataka Kinjo and Atsushi Miyawaki. *A fluorescent variant of a protein from the stony coral Montipora facilitates dual-color single-laser fluorescence cross-correlation spectroscopy.* Nat. Biotechnol. **24**(5), 577–581 (2006).

[79] Ryoko Ando, Hiroshi Hama, Miki Yamamoto-Hino, Hideaki Mizuno and Atsushi Miyawaki. *An optical marker based on the UV-induced green-to-red photoconversion of a fluorescent protein.* Proc. Natl. Acad. Sci. USA **99**(20), 12651–12656 (2002).

[80] P. S. Dittrich, S. P. Schäfer and P. Schwille. *Characterization of the Photoconversion on Reaction of the Fluorescent Protein Kaede on the Single-Molecule Level.* Biophys. J. **89**(5), 3446–3455 (2005).

[81] Ryoko Ando, Hideaki Mizuno and Atsushi Miyawaki. *Regulated Fast Nucleocytoplasmic Shuttling Observed by Reversible Protein Highlighting.* Science **306**(5700), 1370–1373 (2004).

[82] Peter Dedecker, Jun-ichi Hotta, Ryoko Ando, Atsushi Miyawaki, Yves Engelborghs and Johan Hofkens. *Fast and Reversible Photoswitching of the Fluorescent Protein Dronpa as Evidenced by Fluorescence Correlation Spectroscopy.* Biophys. J. **91**(5), L45–L47 (2006).

[83] U. Haupts, S. Maiti, P. Schwille and W. W. Webb. *Dynamics of fluorescence fluctuations in green fluorescent protein observed by fluorescence correlation spectroscopy.* Proc. Natl. Acad. Sci. USA **95**(23), 13573–13578 (1998).

[84] J. Widengren, U. Mets and R. Rigler. *Photodynamic properties of green fluorescent proteins investigated by fluorescence correlation spectroscopy.* Chem. Phys. **250**(2), 171–186 (1999).

[85] M. F. Garcia-Parajo, G. M. Segers-Nolten, J. A. Veerman, J. Greve and N. F. van Hulst. *Real-time light-driven dynamics of the fluorescence emission in single green fluorescent protein molecules.* Proc. Natl. Acad. Sci. USA **97**(13), 7237–7242 (2000).

[86] P. Schwille, S. Kummer, A.A. Heikal, W.E. Moerner and W.W. Webb. *Fluorescence correlation spectroscopy reveals fast optical excitation-driven intramolecular dynamics of yellow fluorescent proteins.* Proc. Natl. Acad. Sci. USA **97**(1), 151–156 (2000).

[87] Andreas Schenk, Sergey Ivanchenko, Carlheinz Röcker, Jörg Wiedenmann and G. Ulrich Nienhaus. *Photodynamics of Red Fluorescent Proteins Studied by Fluorescence Correlation Spectroscopy.* Biophys. J. **86**(1 Pt 1), 384–394 (2004).

[88] C. Bosisio, V. Quercioli, M. Collini, L. D'Alfonso, G. Baldini, S. Bettati, B. Campanini, S. Raboni and G. Chirico. *Protonation and Conformational Dynamics of GFP Mutants by Two-Photon Excitation Fluorescence Correlation Spectroscopy.* J. Phys. Chem. B **112**(29), 8806–8814 (2008).

[89] M. Bruchez, M. Moronne, P. Gin, S. Weiss and A. P. Alivisatos. *Semiconductor Nanocrystals as Fluorescent Biological Labels.* Science **281**(5385), 2013–2016 (1998).

[90] W. C. Chan and S. Nie. *Quantum Dot Bioconjugates for Ultrasensitive Nonisotopic Detection.* Science **281**(5385), 2016–2018 (1998).

[91] X. Michalet, F.F. Pinaud, L.A. Bentolila, J.M. Tsay, S. Doose, J.J. Li, G. Sundaresan, A.M. Wu, S.S. Gambhir and S. Weiss. *Quantum Dots for Live Cells, in Vivo Imaging, and Diagnostics.* Science **307**(5709), 538–544 (2005).

[92] Sören Doose, James M. Tsay, Fabien Pinaud and Shimon Weiss. *Comparison of Photophysical and Colloidal Properties of Biocompatible Semiconductor Nanocrystals Using Fluorescence Correlation Spectroscopy.* Anal. Chem. **77**(7), 2235–2242 (2005).

[93] Jie Yao, Daniel R. Larson, Harshad D. Vishwasrao, Warren R. Zipfel and Watt W. Webb. *Blinking and nonradiant dark fraction of water-soluble quantum dots in aqueous solution.* Proc. Natl. Acad. Sci. USA **102**(40), 14284–14289 (2005).

[94] J. A. Rochira, M. V. Gudheti, T. J. Gould, R. R. Laughlin, J. L. Nadeau and S. T. Hess. *Fluorescence Intermittency Limits Brightness in CdSe/ZnS Nanoparticles Quantified by Fluorescence Correlation Spectroscopy.* J. Phys. Chem. C **111**(4), 1695–1708 (2007).

[95] Alexia I. Bachir, David L. Kolin, Katrin G. Heinze, Benedict Hebert and Paul W. Wiseman. *A guide to accurate measurement of diffusion using fluorescence correlation techniques with blinking quantum dot nanoparticle labels.* J. Chem. Phys. **128**(22), 225105 (2008).

[96] Daniel R. Larson, Warren R. Zipfel, Rebecca M. Williams, Stephen W. Clark, Marcel P. Bruchez, Frank W. Wise and Watt W. Webb. *Water-Soluble Quantum Dots for Multiphoton Fluorescence Imaging in Vivo.* Science **300**(5624), 1434–1436 (2003).

[97] Tim Liedl, Simon Keller, Friedrich C. Simmel, Joachim O. Rädler and Wolfgang J. Parak. *Fluorescent Nanocrystals as Colloidal Probes in Complex Fluids Measured by Fluorescence Correlation Spectroscopy.* Small **1**(10), 997–1003 (2005).

[98] J. L. Swift, R. Heuff and D. T. Cramb. *A Two-Photon Excitation Fluorescence Cross-Correlation Assay for a Model Ligand-Receptor Binding System Using Quantum Dots.* Biophys. J. **90**(4), 1396–1410 (2006).

[99] Romey F. Heuff, Jody L. Swift and David T. Cramb. *Fluorescence correlation spectroscopy using quantum dots: advances, challenges and opportunities.* Phys. Chem. Chem. Phys. **9**(16), 1870–1880 (2007).

[100] T. J. Gould, J. Bewersdorf and S. T. Hess. *A Quantitative Comparison of the Photophysical Properties of Selected Quantum Dots and Organic Fluorophores.* Z. Phys. Chem. **222**(5-6), 833–849 (2008).

[101] Titus Lucretius Carus (translated by William Ellery Leonard). *Of The Nature of Things.* http://www.gutenberg.org/dirs/7/8/785/785-h/785-h.htm, 2009.

[102] *Brownian Motion.* http://en.wikipedia.org/wiki/Brownian_motion, 2009.

[103] Elke Haustein. *Fluorescence fluctuation spectroscopy on freely diffusing and spatially confined single molecules.* PhD thesis, TU Dresden, 2005.

[104] Jonas Ries. *Advanced Fluorescence Correlation Techniques to Study Membrane Dynamics.* PhD thesis, TU Dresden, 2008.

[105] J. Widengren, U. Mets and R. Rigler. *Fluorescence Correlation Spectroscopy of Triplet States in Solution: A Theoretical and Experimental Study.* J. Phys. Chem. **99**(36), 13368–13379 (1995).

[106] Lloyd M. Davis and Guoqing Shen. *Accounting for Triplet and Saturation Effects in FCS Measurements.* Curr. Pharm. Biotechnol. **7**(4), 287–301 (2006).

[107] Markus Burkhardt. *Two-Focus FCCS curve measured with EMCCD-FCS.* personal communication, 2009.

[108] Jörg Enderlein, Ingo Gregor, Digambara Patra, Thomas Dertinger and U. Benjamin Kaupp. *Performance of Fluorescence Correlation Spectroscopy for Measuring Diffusion and Concentration.* ChemPhysChem **6**(11), 2324–2336 (2005).

[109] Stanley M. Sorscher and Melvin P. Klein. *Profile of a focussed collimated laser beam near the focal minimum characterized by fluorescence correlation spectroscopy.* Rev. Sci. Instrum. **51**(1), 98–102 (1980).

[110] A. Benda, M. Benes, V. Marecek, A. Lhotsky, W. T. Hermens and M. Hof. *How To Determine Diffusion Coefficients in Planar Phospholipid Systems by Confocal Fluorescence Correlation Spectroscopy.* Langmuir **19**(10), 4120–4126 (2003).

[111] R. Dorn, S. Quabis and G. Leuchs. *The focus of light-linear polarization breaks the rotational symmetry of the focal spot.* J. Mod. Opt. **50**(12), 1917–1926 (2003).

[112] Jörg Enderlein, Ingo Gregor, Digambara Patra and Jörg Fitter. *Art and Artefacts of Fluorescence Correlation Spectroscopy.* Curr. Pharm. Biotechnol. **5**(2), 155–161 (2004).

[113] Krishnananda Chattopadhyay, Saveez Saffarian, Elliot L. Elson and Carl Frieden. *Measuring Unfolding of Proteins in the Presence of Denaturant Using Fluorescence Correlation Spectroscopy.* Biophys. J. **88**(2), 1413–1422 (2005).

[114] Goro Nishimura and Masataka Kinjo. *Systematic Error in Fluorescence Correlation Measurements Identified by a Simple Saturation Model of Fluorescence.* Anal. Chem. **76**(7), 1963–1970 (2004).

[115] Ingo Gregor, Digambara Patra and Jörg Enderlein. *Optical Saturation in Fluorescence Correlation Spectroscopy under Continuous-Wave and Pulsed Excitation.* ChemPhysChem **6**(1), 164–170 (2005).

[116] P. S. Dittrich and P. Schwille. *Photobleaching and stabilization of fluorophores used for single-molecule analysis with one- and two-photon excitation.* Appl. Phys. B **73**(8), 829–837 (2001).

[117] Jerker Widengren and Rudolf Rigler. *Mechanisms of photobleaching investigated by fluorescence correlation spectroscopy.* Bioimaging **4**(3), 149 (1996).

[118] C. Eggeling, J. Widengren, R. Rigler and C. A. M. Seidel. *Photobleaching of Fluorescent Dyes under Conditions Used for Single-Molecule Detection: Evidence of Two-Step Photolysis.* Anal. Chem. **70**(13), 2651–2659 (1998).

[119] Christian Eggeling, Andreas Volkmer and Claus A. M. Seidel. *Molecular photobleaching kinetics of Rhodamine 6G by one- and two-photon induced confocal fluorescence microscopy.* ChemPhysChem **6**(5), 791–804 (2005).

[120] A. Delon, Y. Usson, J. Derouard, T. Biben and C. Souchier. *Photobleaching, Mobility, and Compartmentalisation: Inferences in Fluorescence Correlation Spectroscopy.* J. Fluoresc. **14**(3), 255–267 (2004).

[121] Ming Zhao, Lei Jin, Bo Chen, Yao Ding, Hui Ma and Dieyan Chen. *Afterpulsing and its correction in fluorescence correlation spectroscopy experiments.* Appl. Opt. **42**(19), 4031–4036 (2003).

[122] A. Gennerich and D. Schild. *Fluorescence Correlation Spectroscopy in Small Cytosolic Compartments Depends Critically on the Diffusion Model Used.* Biophys. J. **79**(6), 3294–3306 (2000).

[123] A. Gennerich and D. Schild. *Anisotropic Diffusion in Mitral Cell Dendrites Revealed by Fluorescence Correlation Spectroscopy.* Biophys. J. **83**(1), 510–522 (2002).

[124] M. Wachsmuth, W. Waldeck and J. Langowski. *Anomalous Diffusion of Fluorescent Probes Inside Living Cell Nuclei Investigated by Spatially-resolved Fluorescence Correlation Spectroscopy.* J. Mol. Biol. **298**(4), 677–689 (2000).

[125] Matthias Weiss, Markus Elsner, Fredrik Kartberg and Tommy Nilsson. *Anomalous Subdiffusion Is a Measure for Cytoplasmic Crowding in Living Cells.* Biophys. J. **87**(5), 3518–3524 (2004).

[126] Gernot Guigas, Claudia Kalla and Matthias Weiss. *Probing the Nanoscale Viscoelasticity of Intracellular Fluids in Living Cells.* Biophys. J. **93**(1), 316–323 (2007).

[127] Gernot Guigas, Claudia Kalla and Matthias Weiss. *The degree of macromolecular crowding in the cytoplasm and nucleoplasm of mammalian cells is conserved.* FEBS Lett. **581**(26), 5094–5098 (2007).

[128] Gernot Guigas and Matthias Weiss. *Sampling the Cell with Anomalous Diffusion - The Discovery of Slowness.* Biophys. J. **94**(1), 90–94 (2008).

[129] Ariel Lubelski and Joseph Klafter. *Fluorescence Correlation Spectroscopy: The Case of Subdiffusion.* Biophys. J. **96**(6), 2055–2063 (2009).

[130] Benoit B. Mandelbrot and John W. van Ness. *Fractional Brownian Motion, Fractional Noises and Applications.* SIAM Review **10**(4), 422–437 (1968).

[131] Jedrzej Szymański, Adam Patkowski, Jacek Gapiński, Agnieszka Wilk and Robert Hołyst. *Movement of Proteins in an Environment Crowded by Surfactant Micelles: Anomalous versus Normal Diffusion.* J. Phys. Chem. B **110**(14), 7367–7373 (2006).

[132] Barbara K. Müller, Evgeny Zaychikov, Christoph Bräuchle and Don C. Lamb. *Pulsed Interleaved Excitation.* Biophys. J. **89**(5), 3508–3522 (2005).

[133] Elmar Thews, Margarita Gerken, Reiner Eckert, Johannes Zäpfel, Carsten Tietz and Jörg Wrachtrup. *Cross Talk Free Fluorescence Cross Correlation Spectroscopy in Live Cells.* Biophys. J. **89**(3), 2069–2076 (2005).

[134] Kirsten Bacia. *Dynamic Processes in Membranes Studied by Fluorescence Correlation Spectroscopy.* PhD thesis, TU Dresden, 2005.

[135] T. Wohland, R. Rigler and H. Vogel. *The Standard Deviation in Fluorescence Correlation Spectroscopy.* Biophys. J. **80**(6), 2987–2999 (2001).

[136] P. S. Dittrich and A. Manz. *Lab-on-a-chip: microfluidics in drug discovery.* Nat. Rev. Drug. Discov. **5**(3), 210–218 (2006).

[137] D. J. Laser and J. G. Santiago. *A review of micropumps.* J. Micromech. Microeng. **14**(6), R35–R64 (2004).

[138] R. Hagedorn, G. Fuhr, T. Müller and J. Gimsa. *Traveling-wave dielectrophoresis of microparticles.* Electrophoresis **13**(1-2), 49–54 (1992).

[139] M. Felten, P. Geggier, M. Jager and C. Duschl. *Controlling electrohydrodynamic pumping in microchannels through defined temperature fields.* Phys. Fluids **18**(5), 051707 (2006).

[140] D. Magde, W. W. Webb and E. L. Elson. *Fluorescence Correlation Spectroscopy .3. Uniform Translation And Laminar-Flow.* Biopolymers **17**(2), 361–376 (1978).

[141] M. Gösch, H. Blom, J. Holm, T. Heino and R. Rigler. *Hydrodynamic Flow Profiling in Microchannel Structures by Single Molecule Fluorescence Correlation Spectroscopy.* Anal. Chem. **72**(14), 3260–3265 (2000).

[142] Kalyan K. Kuricheti, Volker Buschmann and Kenneth D. Weston. *Application of Fluorescence Correlation Spectroscopy for Velocity Imaging in Microfluidic Devices.* Appl. Spectrosc. **58**(10), 1180–1186 (2004).

[143] Paul C. Brister, Kalyan K. Kuricheti, Volker Buschmann and Kenneth D. Weston. *Fluorescence correlation spectroscopy for flow rate imaging and monitoring–optimization, limitations and artifacts.* Lab Chip **5**(7), 785–791 (2005).

[144] D. Lumma, A. Best, A. Gansen, F. Feuillebois, J. O. Radler and O. I. Vinogradova. *Flow profile near a wall measured by double-focus fluorescence cross-correlation.* Phys. Rev. E **67**(5), 056313 (2003).

[145] Jaemyeong Jung and Alan Van Orden. *Folding and Unfolding Kinetics of DNA Hairpins in Flowing Solution by Multiparameter Fluorescence Correlation Spectroscopy.* J. Phys. Chem. B **109**(8), 3648–3657 (2005).

[146] Jaemyeong Jung and Alan Van Orden. *A Three-State Mechanism for DNA Hairpin Folding Characterized by Multiparameter Fluorescence Fluctuation Spectroscopy.* J. Am. Chem. Soc. **128**(4), 1240–1249 (2006).

[147] P. S. Dittrich and P. Schwille. *Spatial Two-Photon Fluorescence Cross-Correlation Spectroscopy for Controlling Molecular Transport in Microfluidic Structures.* Anal. Chem. **74**(17), 4472–4479 (2002).

[148] Maika Felten. *Traveling electromagnetic waves at high frequencies: A versatile method for liquid transport in microfluidic systems.* PhD thesis, Humboldt-Universität zu Berlin, 2007.

[149] N. Raju and E. Meiburg. *Dynamics of small, spherical particles in vortical and stagnation point flow fields.* Phys. Fluids **9**(2), 299–314 (1997).

[150] R. Chein and J. N. Chung. *Effects of vortex pairing on particle dispersion in turbulent shear flows.* Int. J. Multiphase Flow **13**(6), 785–802 (1987).

[151] J. E. Martin and E. Meiburg. *The accumulation and dispersion of heavy-particles in forced 2-dimensional mixing layers. I. The fundamental and subharmonic cases.* Phys. Fluids **6**(3), 1116–1132 (1994).

[152] B. J. Lazaro and J. C. Lasheras. *Particle dispersion in the developing free shear-layer. 1. Unforced flow.* J.Fluid Mech. **235**, 143–178 (1992).

[153] B. J. Lazaro and J. C. Lasheras. *Particle dispersion in the developing free shear-layer. 2. Forced flow.* J. Fluid Mech. **235**, 179–221 (1992).

[154] Xiaotao Pan, Hanry Yu, Xianke Shi, Vladimir Korzh and Thorsten Wohland. *Characterization of flow direction in microchannels and zebrafish blood vessels by scanning fluorescence correlation spectroscopy.* J. Biomed. Opt. **12**(1), 014034 (2007).

[155] A. R. van der Krol, L. A. Mur, M. Beld, J. N. Mol and A. R. Stuitje. *Flavonoid Genes in Petunia: Addition of a Limited Number of Gene Copies May Lead to a Suppression of Gene Expression.* Plant Cell **2**(4), 291–299 (1990).

[156] C. Napoli, C. Lemieux and R. Jorgensen. *Introduction of a Chimeric Chalcone Synthase Gene into Petunia Results in Reversible Co-Suppression of Homologous Genes in trans.* Plant Cell **2**(4), 279–289 (1990).

[157] S. Guo and K. J. Kemphues. *par-1, a gene required for establishing polarity in C. elegans embryos, encodes a putative Ser/Thr kinase that is asymmetrically distributed.* Cell **81**(4), 611–620 (1995).

[158] A. Fire, S. Q. Xu, M. K. Montgomery, S. A. Kostas, S. E. Driver and C. C. Mello. *Potent and specific genetic interference by double-stranded RNA in Caenorhabditis elegans.* Nature **391**(6669), 806–811 (1998).

[159] J. R. Kennerdell and R. W. Carthew. *Use of dsRNA-Mediated Genetic Interference to Demonstrate that frizzled and frizzled 2 Act in the Wingless Pathway.* Cell **95**(7), 1017–1026 (1998).

[160] A. Wargelius, S. Ellingsen and A. Fjose. *Double-Stranded RNA Induces Specific Developmental Defects in Zebrafish Embryos.* Biochem. Biophys. Res. Commun. **263**(1), 156–161 (1999).

[161] Y. X. Li, M. J. Farrell, R. Liu, N. Mohanty and M. L. Kirby. *Double-Stranded RNA Injection Produces Null Phenotypes in Zebrafish.* Dev. Biol. **217**(2), 394–405 (2000).

[162] P. Svoboda, P. Stein, H. Hayashi and R. M. Schultz. *Selective reduction of dormant maternal mRNAs in mouse oocytes by RNA interference.* Development **127**(19), 4147–4156 (2000).

[163] F. Wianny and M. Zernicka-Goetz. *Specific interference with gene function by double-stranded RNA in early mouse development.* Nat. Cell Biol. **2**(2), 70–75 (2000).

[164] A. J. Hamilton and D. C. Baulcombe. *A Species of Small Antisense RNA in Posttranscriptional Gene Silencing in Plants.* Science **286**(5441), 950–952 (1999).

[165] P. D. Zamore, T. Tuschl, P. A. Sharp and D. P. Bartel. *RNAi: Double-Stranded RNA Directs the ATP-Dependent Cleavage of mRNA at 21 to 23 Nucleotide Intervals.* Cell **101**(1), 25–33 (2000).

[166] S. M. Elbashir, W. Lendeckel and T. Tuschl. *RNA interference is mediated by 21- and 22-nucleotide RNAs.* Genes Dev. **15**(2), 188–200 (2001).

[167] S. M. Elbashir, J. Harborth, W. Lendeckel, A. Yalcin, K. Weber and T. Tuschl. *Duplexes of 21-nucleotide RNAs mediate RNA interference in cultured mammalian cells.* Nature **411**(6836), 494–498 (2001).

[168] R. C. Lee, R. L. Feinbaum and V. Ambros. *The C. elegans heterochronic gene lin-4 encodes small RNAs with antisense complementarity to lin-14.* Cell **75**(5), 843–854 (1993).

[169] M. Lagos-Quintana, R. Rauhut, W. Lendeckel and T. Tuschl. *Identification of Novel Genes Coding for Small Expressed RNAs.* Science **294**(5543), 853–858 (2001).

[170] N. C. Lau, L. P. Lim, E. G. Weinstein and D. P. Bartel. *An Abundant Class of Tiny RNAs with Probable Regulatory Roles in Caenorhabditis elegans.* Science **294**(5543), 858–862 (2001).

[171] R. C. Lee and V. Ambros. *An Extensive Class of Small RNAs in Caenorhabditis elegans.* Science **294**(5543), 862–864 (2001).

[172] Isaac Bentwich, Amir Avniel, Yael Karov, Ranit Aharonov, Shlomit Gilad, Omer Barad, Adi Barzilai, Paz Einat, Uri Einav, Eti Meiri, Eilon Sharon, Yael Spector and Zvi Bentwich. *Identification of hundreds of conserved and nonconserved human microRNAs.* Nat. Genet. **37**(7), 766–770 (2005).

[173] Benjamin P. Lewis, Christopher B. Burge and David P. Bartel. *Conserved Seed Pairing, Often Flanked by Adenosines, Indicates that Thousands of Human Genes are MicroRNA Targets.* Cell **120**(1), 15–20 (2005).

[174] Xiaohui Xie, Jun Lu, E. J. Kulbokas, Todd R. Golub, Vamsi Mootha, Kerstin Lindblad-Toh, Eric S. Lander and Manolis Kellis. *Systematic discovery of regulatory motifs in human promoters and 3' UTRs by comparison of several mammals.* Nature **434**(7031), 338–345 (2005).

[175] Robin C. Friedman, Kyle Kai-How Farh, Christopher B. Burge and David P. Bartel. *Most mammalian mRNAs are conserved targets of microRNAs.* Genome Res. **19**(1), 92–105 (2009).

[176] Haidi Zhang, Fabrice A. Kolb, Lukasz Jaskiewicz, Eric Westhof and Witold Filipowicz. *Single Processing Center Models for Human Dicer and Bacterial RNase III.* Cell **118**(1), 57–68 (2004).

[177] I. J. MacRae, K. H. Zhou, F. Li, A. Repic, A. N. Brooks, W. Z. Cande, P. D. Adams and J. A. Doudna. *Structural Basis for Double-Stranded RNA Processing by Dicer.* Science **311**(5758), 195–198 (2006).

[178] Yu-Ren Yuan, Yi Pei, Jin-Biao Ma, Vitaly Kuryavyi, Maria Zhadina, Gunter Meister, Hong-Ying Chen, Zbigniew Dauter, Thomas Tuschl and Dinshaw J. Patel. *Crystal Structure of A. aeolicus Argonaute, a Site-Specific DNA-Guided Endoribonuclease, Provides Insights into RISC-Mediated mRNA Cleavage.* Mol. Cell **19**(3), 405–419 (2005).

[179] Megha Ghildiyal and Phillip D. Zamore. *Small silencing RNAs: an expanding universe.* Nat. Rev. Genet. **10**(2), 94–108 (2009).

[180] Sébastien Pfeffer, Mihaela Zavolan, Friedrich A. Grässer, Minchen Chien, James J. Russo, Jingyue Ju, Bino John, Anton J. Enright, Debora Marks, Chris Sander and Thomas Tuschl. *Identification of Virus-Encoded MicroRNAs.* Science **304**(5671), 734–736 (2004).

[181] Erno Wienholds, Wigard P. Kloosterman, Eric Miska, Ezequiel Alvarez-Saavedra, Eugene Berezikov, Ewart de Bruijn, H. Robert Horvitz, Sakari Kauppinen and Ronald H. A. Plasterk. *MicroRNA Expression in Zebrafish Embryonic Development.* Science **309**(5732), 310–311 (2005).

[182] Oliver H. Tam, Alexei A. Aravin, Paula Stein, Angelique Girard, Elizabeth P. Murchison, Sihem Cheloufi, Emily Hodges, Martin Anger, Ravi Sachidanandam, Richard M. Schultz and Gregory J. Hannon. *Pseudogene-derived small interfering RNAs regulate gene expression in mouse oocytes.* Nature **453**(7194), 534–538 (2008).

[183] Toshiaki Watanabe, Yasushi Totoki, Atsushi Toyoda, Masahiro Kaneda, Satomi Kuramochi-Miyagawa, Yayoi Obata, Hatsune Chiba, Yuji Kohara, Tomohiro Kono, Toru Nakano, M. Azim Surani, Yoshiyuki Sakaki and Hiroyuki Sasaki. *Endogenous siRNAs from naturally formed dsRNAs regulate transcripts in mouse oocytes.* Nature **453**(7194), 539–543 (2008).

[184] Joshua E. Babiarz, J. Graham Ruby, Yangming Wang, David P. Bartel and Robert Blelloch. *Mouse ES cells express endogenous shRNAs, siRNAs, and other Microprocessor-independent, Dicer-dependent small RNAs.* Genes Dev. **22**(20), 2773–2785 (2008).

[185] Wei-Jen Chung, Katsutomo Okamura, Raquel Martin and Eric C. Lai. *Endogenous RNA Interference Provides a Somatic Defense against Drosophila Transposons.* Curr. Biol. **18**(11), 795–802 (2008).

[186] Benjamin Czech, Colin D. Malone, Rui Zhou, Alexander Stark, Catherine Schlingeheyde, Monica Dus, Norbert Perrimon, Manolis Kellis, James A. Wohlschlegel, Ravi Sachidanandam, Gregory J. Hannon and Julius Brennecke. *An endogenous small interfering RNA pathway in Drosophila.* Nature **453**(7196), 798–802 (2008).

[187] Megha Ghildiyal, Hervé Seitz, Michael D. Horwich, Chengjian Li, Tingting Du, Soohyun Lee, Jia Xu, Ellen L W Kittler, Maria L. Zapp, Zhiping Weng and Phillip D. Zamore. *Endogenous siRNAs Derived from Transposons and mRNAs in Drosophila Somatic Cells.* Science **320**(5879), 1077–1081 (2008).

[188] Yoshinori Kawamura, Kuniaki Saito, Taishin Kin, Yukiteru Ono, Kiyoshi Asai, Takafumi Sunohara, Tomoko N. Okada, Mikiko C. Siomi and Haruhiko Siomi. *Drosophila endogenous small RNAs bind to Argonaute 2 in somatic cells.* Nature **453**(7196), 793–797 (2008).

[189] Katsutomo Okamura, Wei-Jen Chung, J. Graham Ruby, Huili Guo, David P. Bartel and Eric C. Lai. *The Drosophila hairpin RNA pathway generates endogenous short interfering RNAs.* Nature **453**(7196), 803–806 (2008).

[190] Hongwei Li, Wan Xiang Li and Shou Wei Ding. *Induction and Suppression of RNA Silencing by an Animal Virus.* Science **296**(5571), 1319–1321 (2002).

[191] Xiao-Hong Wang, Roghiyh Aliyari, Wan-Xiang Li, Hong-Wei Li, Kevin Kim, Richard Carthew, Peter Atkinson and Shou-Wei Ding. *RNA Interference Directs Innate Immunity Against Viruses in Adult Drosophila.* Science **312**(5772), 452–454 (2006).

[192] Robert A. Zambon, Vikram N. Vakharia and Louisa P. Wu. *RNAi is an antiviral immune response against a dsRNA virus in Drosophila melanogaster.* Cell. Microbiol. **8**(5), 880–889 (2006).

[193] John Bracht, Shaun Hunter, Rachel Eachus, Phillip Weeks and Amy E. Pasquinelli. *Trans-splicing and polyadenylation of let-7 microRNA primary transcripts.* RNA **10**(10), 1586–1594 (2004).

[194] Xuezhong Cai, Curt H. Hagedorn and Bryan R. Cullen. *Human microRNAs are processed from capped, polyadenylated transcripts that can also function as mRNAs.* RNA **10**(12), 1957–1966 (2004).

[195] Yoontae Lee, Minju Kim, Jinju Han, Kyu-Hyun Yeom, Sanghyuk Lee, Sung Hee Baek and V. Narry Kim. *MicroRNA genes are transcribed by RNA polymerase II.* EMBO J. **23**(20), 4051–4060 (2004).

[196] Chang-Gong Liu, George Adrian Calin, Brian Meloon, Nir Gamliel, Cinzia Sevignani, Manuela Ferracin, Calin Dan Dumitru, Masayoshi Shimizu, Simona Zupo, Mariella Dono, Hansjuerg Alder, Florencia Bullrich, Massimo Negrini and Carlo M. Croce. *An oligonucleotide microchip for genome-wide microRNA profiling in human and mouse tissues.* Proc. Natl. Acad. Sci. USA **101**(26), 9740–9744 (2004).

[197] Tomas Babak, Wen Zhang, Quaid Morris, Benjamin J. Blencowe and Timothy R. Hughes. *Probing microRNAs with microarrays: Tissue specificity and functional inference.* RNA **10**(11), 1813–1819 (2004).

[198] Omer Barad, Eti Meiri, Amir Avniel, Ranit Aharonov, Adi Barzilai, Isaac Bentwich, Uri Einav, Shlomit Gilad, Patrick Hurban, Yael Karov, Edward K. Lobenhofer, Eilon Sharon, Yoel M. Shiboleth, Marat Shtutman, Zvi Bentwich and Paz Einat. *MicroRNA expression detected by oligonucleotide microarrays: System establishment and expression profiling in human tissues.* Genome Res. **14**(12), 2486–2494 (2004).

[199] Glen M. Borchert, William Lanier and Beverly L. Davidson. *RNA polymerase III transcribes human microRNAs.* Nat. Struct. Mol. Biol. **13**(12), 1097–1101 (2006).

[200] Yan Zeng, Eric J. Wagner and Bryan R. Cullen. *Both Natural and Designed Micro RNAs Can Inhibit the Expression of Cognate mRNAs When Expressed in Human Cells.* Mol. Cell **9**(6), 1327–1333 (2002).

[201] Eugene Berezikov, Victor Guryev, José van de Belt, Erno Wienholds, Ronald H. A. Plasterk and Edwin Cuppen. *Phylogenetic Shadowing and Computational Identification of Human microRNA Genes.* Cell **120**(1), 21–24 (2005).

[202] Yan Zeng, Rui Yi and Bryan R. Cullen. *Recognition and cleavage of primary microRNA precursors by the nuclear processing enzyme Drosha.* EMBO J. **24**(1), 138–148 (2005).

[203] Yoontae Lee, Kipyoung Jeon, Jun-Tae Lee, Sunyoung Kim and V. Narry Kim. *MicroRNA maturation: stepwise processing and subcellular localization.* EMBO J. **21**(17), 4663–4670 (2002).

[204] Yoontae Lee, Chiyoung Ahn, Jinju Han, Hyounjeong Choi, Jaekwang Kim, Jeongbin Yim, Junho Lee, Patrick Provost, Olof Rådmark, Sunyoung Kim and V. Narry Kim. *The nuclear RNase III Drosha initiates microRNA processing.* Nature **425**(6956), 415–419 (2003).

[205] Ahmet M. Denli, Bastiaan B. J. Tops, Ronald H. A. Plasterk, René F. Ketting and Gregory J. Hannon. *Processing of primary microRNAs by the Microprocessor complex.* Nature **432**(7014), 231–235 (2004).

[206] Richard I. Gregory, Kai-Ping Yan, Govindasamy Amuthan, Thimmaiah Chendrimada, Behzad Doratotaj, Neil Cooch and Ramin Shiekhattar. *The Microprocessor complex mediates the genesis of microRNAs.* Nature **432**(7014), 235–240 (2004).

[207] Jinju Han, Yoontae Lee, Kyu-Hyun Yeom, Young-Kook Kim, Hua Jin and V. Narry Kim. *The Drosha-DGCR8 complex in primary microRNA processing.* Genes Dev. **18**(24), 3016–3027 (2004).

[208] Markus Landthaler, Abdullah Yalcin and Thomas Tuschl. *The Human DiGeorge Syndrome Critical Region Gene 8 and Its D. melanogaster Homolog Are Required for miRNA Biogenesis.* Curr. Biol. **14**(23), 2162–2167 (2004).

[209] Sun Young Sohn, Won Jin Bae, Jeong Joo Kim, Kyu-Hyeon Yeom, V. Narry Kim and Yunje Cho. *Crystal structure of human DGCR8 core.* Nat. Struct. Mol. Biol. **14**(9), 847–853 (2007).

[210] Jinju Han, Yoontae Lee, Kyu-Hyeon Yeom, Jin-Wu Nam, Inha Heo, Je-Keun Rhee, Sun Young Sohn, Yunje Cho, Byoung-Tak Zhang and V. Narry Kim. *Molecular Basis for the Recognition of Primary microRNAs by the Drosha-DGCR8 Complex.* Cell **125**(5), 887–901 (2006).

[211] William Ritchie, Matthieu Legendre and Daniel Gautheret. *RNA stem–loops: To be or not to be cleaved by RNAse III.* RNA **13**(4), 457–462 (2007).

[212] Dipali G. Sashital and Jennifer A. Doudna. *Structural insights into RNA interference.* Curr. Opin. Struct. Biol. **20**(1), 90–97 (2010).

[213] Katsutomo Okamura, Joshua W. Hagen, Hong Duan, David M. Tyler and Eric C. Lai. *The Mirtron Pathway Generates microRNA-Class Regulatory RNAs in Drosophila.* Cell **130**(1), 89–100 (2007).

[214] J. Graham Ruby, Calvin H. Jan and David P. Bartel. *Intronic microRNA precursors that bypass Drosha processing.* Nature **448**(7149), 83–86 (2007).

[215] Eugene Berezikov, Wei-Jen Chung, Jason Willis, Edwin Cuppen and Eric C. Lai. *Mammalian Mirtron Genes.* Mol. Cell **28**(2), 328–336 (2007).

[216] Rui Yi, Yi Qin, Ian G. Macara and Bryan R. Cullen. *Exportin-5 mediates the nuclear export of pre-microRNAs and short hairpin RNAs.* Genes Dev. **17**(24), 3011–3016 (2003).

[217] Markus T. Bohnsack, Kevin Czaplinski and Dirk Gorlich. *Exportin 5 is a RanGTP-dependent dsRNA-binding protein that mediates nuclear export of pre-miRNAs.* RNA **10**(2), 185–191 (2004).

[218] Elsebet Lund, Stephan Güttinger, Angelo Calado, James E. Dahlberg and Ulrike Kutay. *Nuclear Export of MicroRNA Precursors.* Science **303**(5654), 95–98 (2004).

[219] Yan Zeng and Bryan R. Cullen. *Structural requirements for pre-microRNA binding and nuclear export by Exportin 5.* Nucleic Acids Res. **32**(16), 4776–4785 (2004).

[220] E. Bernstein, A. A. Caudy, S. M. Hammond and G. J. Hannon. *Role for a bidentate ribonuclease in the initiation step of RNA interference.* Nature **409**(6818), 363–366 (2001).

[221] Haidi Zhang, Fabrice A. Kolb, Vincent Brondani, Eric Billy and Witold Filipowicz. *Human Dicer preferentially cleaves dsRNAs at their termini without a requirement for ATP.* EMBO J. **21**(21), 5875–5885 (2002).

[222] Patrick Provost, David Dishart, Johanne Doucet, David Frendewey, Bengt Samuelsson and Olof Rådmark. *Ribonuclease activity and RNA binding of recombinant human Dicer.* EMBO J. **21**(21), 5864–5874 (2002).

[223] Ji-Joon Song, Jidong Liu, Niraj H. Tolia, Jonathan Schneiderman, Stephanie K. Smith, Robert A. Martienssen, Gregory J. Hannon and Leemor Joshua-Tor. *The crystal structure of the Argonaute2 PAZ domain reveals an RNA binding motif in RNAi effector complexes.* Nat. Struct. Biol. **10**(12), 1026–1032 (2003).

[224] Andreas Lingel, Bernd Simon, Elisa Izaurralde and Michael Sattler. *Structure and nucleic-acid binding of the Drosophila Argonaute 2 PAZ domain.* Nature **426**(6965), 465–469 (2003).

[225] Kelley S. Yan, Sherry Yan, Amjad Farooq, Arnold Han, Lei Zeng and Ming-Ming Zhou. *Structure and conserved RNA binding of the PAZ domain.* Nature **426**(6965), 468–474 (2003).

[226] Andreas Lingel, Bernd Simon, Elisa Izaurralde and Michael Sattler. *Nucleic acid 3'-end recognition by the Argonaute2 PAZ domain.* Nat. Struct. Mol. Biol. **11**(6), 576–577 (2004).

[227] Jin-Biao Ma, Keqiong Ye and Dinshaw J. Patel. *Structural basis for overhang-specific small interfering RNA recognition by the PAZ domain.* Nature **429**(6989), 318–322 (2004).

[228] Ian J. MacRae, Kaihong Zhou and Jennifer A. Doudna. *Structural determinants of RNA recognition and cleavage by Dicer.* Nat. Struct. Mol. Biol. **14**(10), 934–940 (2007).

[229] Thimmaiah P. Chendrimada, Richard I. Gregory, Easwari Kumaraswamy, Jessica Norman, Neil Cooch, Kazuko Nishikura and Ramin Shiekhattar. *TRBP recruits the Dicer complex to Ago2 for microRNA processing and gene silencing.* Nature **436**(7051), 740–744 (2005).

[230] Yoontae Lee, Inha Hur, Seong-Yeon Park, Young-Kook Kim, Mi Ra Suh and V. Narry Kim. *The role of PACT in the RNA silencing pathway.* EMBO J. **25**(3), 522–532 (2006).

[231] Astrid D. Haase, Lukasz Jaskiewicz, Haidi Zhang, Sébastien Lainé, Ragna Sack, Anne Gatignol and Witold Filipowicz. *TRBP, a regulator of cellular PKR and HIV-1 virus expression, interacts with Dicer and functions in RNA silencing.* EMBO Rep. **6**(10), 961–967 (2005).

[232] Kin Hang Kok, Ming-Him James Ng, Yick-Pang Ching and Dong-Yan Jin. *Human TRBP and PACT Directly Interact with Each Other and Associate with Dicer to Facilitate the Production of Small Interfering RNA.* J. Biol. Chem. **282**(24), 17649–17657 (2007).

[233] Enbo Ma, Ian J. MacRae, Jack F. Kirsch and Jennifer A. Doudna. *Autoinhibition of Human Dicer by Its Internal Helicase Domain.* J. Mol. Biol. **380**(1), 237–243 (2008).

[234] Gunter Meister, Markus Landthaler, Lasse Peters, Po Yu Chen, Henning Urlaub, Reinhard Lührmann and Thomas Tuschl. *Identification of Novel Argonaute-Associated Proteins.* Curr. Biol. **15**(23), 2149–2155 (2005).

[235] Richard I. Gregory, Thimmaiah P. Chendrimada, Neil Cooch and Ramin Shiekhattar. *Human RISC Couples MicroRNA Biogenesis and Posttranscriptional Gene Silencing.* Cell **123**(4), 631–640 (2005).

[236] Elisavet Maniataki and Zissimos Mourelatos. *A human, ATP-independent, RISC assembly machine fueled by pre-miRNA.* Genes Dev. **19**(24), 2979–2990 (2005).

[237] Feng Jiang, Xuecheng Ye, Xiang Liu, Lauren Fincher, Dennis McKearin and Qinghua Liu. *Dicer-1 and R3D1-L catalyze microRNA maturation in Drosophila.* Genes Dev. **19**(14), 1674–1679 (2005).

[238] Klaus Förstemann, Yukihide Tomari, Tingting Du, Vasily V. Vagin, Ahmet M. Denli, Diana P. Bratu, Carla Klattenhoff, William E. Theurkauf and Phillip D. Zamore. *Normal microRNA Maturation and Germ-Line Stem Cell Maintenance Requires Loquacious, a Double-Stranded RNA-Binding Domain Protein.* PLoS Biol. **3**(7), e236 (2005).

[239] Kuniaki Saito, Akira Ishizuka, Haruhiko Siomi and Mikiko C. Siomi. *Processing of Pre-microRNAs by the Dicer-1-Loquacious Complex in Drosophila Cells.* PLoS Biol. **3**(7), e235 (2005).

[240] Rui Zhou, Benjamin Czech, Julius Brennecke, Ravi Sachidanandam, James A. Wohlschlegel, Norbert Perrimon and Gregory J. Hannon. *Processing of Drosophila endo-siRNAs depends on a specific Loquacious isoform.* RNA **15**(10), 1886–1895 (2009).

[241] Xiang Liu, Joseph K Park, Feng Jiang, Ying Liu, Dennis McKearin and Qinghua Liu. *Dicer-1, but not Loquacious, is critical for assembly of miRNA-induced silencing complexes.* RNA **13**(12), 2324–2329 (2007).

[242] João Trindade Marques, Kevin Kim, Pei-Hsuan Wu, Trevis M. Alleyne, Nadereh Jafari and Richard W. Carthew. *Loqs and R2D2 act sequentially in the siRNA pathway in Drosophila.* Nat. Struct. Mol. Biol. **17**(1), 24–30 (2010).

[243] Qinghua Liu, Tim A. Rand, Savitha Kalidas, Fenghe Du, Hyun-Eui Kim, Dean P. Smith and Xiaodong Wang. *R2D2, a Bridge Between the Initiation and Effector Steps of the Drosophila RNAi Pathway.* Science **301**(5641), 1921–1925 (2003).

[244] Young Sik Lee, Kenji Nakahara, John W. Pham, Kevin Kim, Zhengying He, Erik J. Sontheimer and Richard W. Carthew. *Distinct Roles for Drosophila Dicer-1 and Dicer-2 in the siRNA/miRNA Silencing Pathways.* Cell **117**(1), 69–81 (2004).

[245] Dianne S. Schwarz, György Hutvágner, Tingting Du, Zuoshang Xu, Neil Aronin and Phillip D. Zamore. *Asymmetry in the Assembly of the RNAi Enzyme Complex.* Cell **115**(2), 199–208 (2003).

[246] Anastasia Khvorova, Angela Reynolds and Sumedha D. Jayasena. *Functional siRNAs and miRNAs Exhibit Strand Bias.* Cell **115**(2), 209–216 (2003).

[247] Philipp J. F. Leuschner, Stefan L. Ameres, Stephanie Kueng and Javier Martinez. *Cleavage of the siRNA passenger strand during RISC assembly in human cells.* EMBO Rep. **7**(3), 314–320 (2006).

[248] Christian Matranga, Yukihide Tomari, Chanseok Shin, David P. Bartel and Phillip D. Zamore. *Passenger-Strand Cleavage Facilitates Assembly of siRNA into Ago2-Containing RNAi Enzyme Complexes.* Cell **123**(4), 607–620 (2005).

[249] Keita Miyoshi, Hiroko Tsukumo, Tomoko Nagami, Haruhiko Siomi and Mikiko C. Siomi. *Slicer function of Drosophila Argonautes and its involvement in RISC formation.* Genes Dev. **19**(23), 2837–2848 (2005).

[250] Tim A. Rand, Sean Petersen, Fenghe Du and Xiaodong Wang. *Argonaute2 Cleaves the Anti-Guide Strand of siRNA During RISC Activation.* Cell **123**(4), 621–629 (2005).

[251] Ying Liu, Xuecheng Ye, Feng Jiang, Chunyang Liang, Dongmei Chen, Junmin Peng, Lisa N. Kinch, Nick V. Grishin and Qinghua Liu. *C3PO, an Endoribonuclease That Promotes RNAi by Facilitating RISC Activation.* Science **325**(5941), 750–753 (2009).

[252] Mayuko Yoda, Tomoko Kawamata, Zain Paroo, Xuecheng Ye, Shintaro Iwasaki, Qinghua Liu and Yukihide Tomari. *ATP-dependent human RISC assembly pathways.* Nat. Struct. Mol. Biol. **17**(1), 17–23 (2010).

[253] G. Brett Robb and Tariq M. Rana. *RNA Helicase A Interacts with RISC in Human Cells and Functions in RISC Loading.* Mol. Cell **26**(4), 523–537 (2007).

[254] Klaus Förstemann, Michael D. Horwich, Liangmeng Wee, Yukihide Tomari and Phillip D. Zamore. *Drosophila microRNAs Are Sorted into Functionally Distinct Argonaute Complexes after Production by Dicer-1.* Cell **130**(2), 287–297 (2007).

[255] Katsutomo Okamura, Akira Ishizuka, Haruhiko Siomi and Mikiko C. Siomi. *Distinct roles for Argonaute proteins in small RNA-directed RNA cleavage pathways.* Genes Dev. **18**(14), 1655–1666 (2004).

[256] Yukihide Tomari, Tingting Du and Phillip D. Zamore. *Sorting of Drosophila Small Silencing RNAs.* Cell **130**(2), 299–308 (2007).

[257] Tomoko Kawamata, Hervé Seitz and Yukihide Tomari. *Structural determinants of miRNAs for RISC loading and slicer-independent unwinding.* Nat. Struct. Mol. Biol. **16**(9), 953–960 (2009).

[258] Yukihide Tomari, Christian Matranga, Benjamin Haley, Natalia Martinez and Phillip D. Zamore. *A Protein Sensor for siRNA Asymmetry.* Science **306**(5700), 1377–1380 (2004).

[259] Yukihide Tomari, Tingting Du, Benjamin Haley, Dianne S. Schwarz, Ryan Bennett, Heather A. Cook, Birgit S. Koppetsch, William E. Theurkauf and Phillip D. Zamore. *RISC Assembly Defects in the Drosophila RNAi Mutant armitage.* Cell **116**(6), 831–841 (2004).

[260] John W. Pham, Janice L. Pellino, Young Sik Lee, Richard W. Carthew and Erik J. Sontheimer. *A Dicer-2-Dependent 80s Complex Cleaves Targeted mRNAs during RNAi in Drosophila.* Cell **117**(1), 83–94 (2004).

[261] Yukihide Tomari and Phillip D. Zamore. *Perspective: machines for RNAi.* Genes Dev. **19**(5), 517–529 (2005).

[262] John W. Pham and Erik J. Sontheimer. *Molecular Requirements for RNA-induced Silencing Complex Assembly in the Drosophila RNA Interference Pathway.* J. Biol. Chem. **280**(47), 39278–39283 (2005).

[263] Xiang Liu, Feng Jiang, Savitha Kalidas, Dean Smith and Qinghua Liu. *Dicer-2 and R2D2 coordinately bind siRNA to promote assembly of the siRISC complexes.* RNA **12**(8), 1514–1520 (2006).

[264] Takashi Sasaki, Aiko Shiohama, Shinsei Minoshima and Nobuyoshi Shimizu. *Identification of eight members of the Argonaute family in the human genome.* Genomics **82**(3), 323–330 (2003).

[265] Jidong Liu, Michelle A. Carmell, Fabiola V. Rivas, Carolyn G. Marsden, J. Michael Thomson, Ji-Joon Song, Scott M. Hammond, Leemor Joshua-Tor and Gregory J. Hannon. *Argonaute2 is the Catalytic Engine of Mammalian RNAi.* Science **305**(5689), 1437–1441 (2004).

[266] Gunter Meister, Markus Landthaler, Agnieszka Patkaniowska, Yair Dorsett, Grace Teng and Thomas Tuschl. *Human Argonaute2 Mediates RNA Cleavage Targeted by miRNAs and siRNAs.* Mol. Cell **15**(2), 185–197 (2004).

[267] Markus Landthaler, Dimos Gaidatzis, Andrea Rothballer, Po Yu Chen, Steven Joseph Soll, Lana Dinic, Tolulope Ojo, Markus Hafner, Mihaela Zavolan and Thomas Tuschl. *Molecular characterization of human Argonaute-containing ribonucleoprotein complexes and their bound target mRNAs.* RNA **14**(12), 2580–2596 (2008).

[268] Ian J. MacRae, Enbo Ma, Min Zhou, Carol V. Robinson and Jennifer A. Doudna. *In vitro reconstitution of the human RISC-loading complex.* Proc. Natl. Acad. Sci. USA **105**(2), 512–517 (2008).

[269] Fabiola V. Rivas, Niraj H. Tolia, Ji-Joon Song, Juan P. Aragon, Jidong Liu, Gregory J. Hannon and Leemor Joshua-Tor. *Purified Argonaute2 and an siRNA form recombinant human RISC.* Nat. Struct. Mol. Biol. **12**(4), 340–349 (2005).

[270] Yu-Ren Yuan, Yi Pei, Hong-Ying Chen, Thomas Tuschl and Dinshaw J. Patel. *A Potential Protein-RNA Recognition Event along the RISC-Loading Pathway from the Structure of A. aeolicus Argonaute with Externally Bound siRNA.* Structure **14**(10), 1557–1565 (2006).

[271] Yanli Wang, Gang Sheng, Stefan Juranek, Thomas Tuschl and Dinshaw J. Patel. *Structure of the guide-strand-containing argonaute silencing complex.* Nature **456**(7219), 209–213 (2008).

[272] James S. Parker, S. Mark Roe and David Barford. *Crystal structure of a PIWI protein suggests mechanisms for siRNA recognition and slicer activity.* EMBO J. **23**(24), 4727–4737 (2004).

[273] James S. Parker, S. Mark Roe and David Barford. *Structural insights into mRNA recognition from a PIWI domain-siRNA guide complex.* Nature **434**(7033), 663–666 (2005).

[274] Jin-Biao Ma, Yu-Ren Yuan, Gunter Meister, Yi Pei, Thomas Tuschl and Dinshaw J. Patel. *Structural basis for 5'-end-specific recognition of guide RNA by the A. fulgidus Piwi protein.* Nature **434**(7033), 666–670 (2005).

[275] Julia Höck, Lasse Weinmann, Christine Ender, Sabine Rüdel, Elisabeth Kremmer, Monika Raabe, Henning Urlaub and Gunter Meister. *Proteomic and functional analysis of Argonaute-containing mRNA-protein complexes in human cells.* EMBO Rep. **8**(11), 1052–1060 (2007).

[276] S. M. Hammond, A. A. Caudy and G. J. Hannon. *Post-transcriptional gene silencing by double-stranded RNA.* Nat. Rev. Genet. **2**(2), 110–119 (2001).

[277] Javier Martinez, Agnieszka Patkaniowska, Henning Urlaub, Reinhard Lührmann and Thomas Tuschl. *Single-Stranded Antisense siRNAs Guide Target RNA Cleavage in RNAi.* Cell **110**(5), 563–574 (2002).

[278] György Hutvágner and Phillip D. Zamore. *A microRNA in a Multiple-Turnover RNAi Enzyme Complex.* Science **297**(5589), 2056–2060 (2002).

[279] S. M. Hammond, E. Bernstein, D. Beach and G. J. Hannon. *An RNA-directed nuclease mediates post-transcriptional gene silencing in Drosophila cells.* Nature **404**(6775), 293–296 (2000).

[280] Marc-André Langlois, Christelle Boniface, Gang Wang, Jessica Alluin, Paul M Salvaterra, Jack Puymirat, John J. Rossi and Nan Sook Lee. *Cytoplasmic and Nuclear Retained DMPK mRNAs Are Targets for RNA Interference in Myotonic Dystrophy Cells.* J. Biol. Chem. **280**(17), 16949–16954 (2005).

[281] G. Brett Robb, Kirk M. Brown, Jaspreet Khurana and Tariq M. Rana. *Specific and potent RNAi in the nucleus of human cells.* Nat. Struct. Mol. Biol. **12**(2), 133–137 (2005).

[282] George L. Sen, Tom S. Wehrman and Helen M. Blau. *mRNA translation is not a prerequisite for small interfering RNA-mediated mRNA cleavage.* Differentiation **73**(6), 287–293 (2005).

[283] Shuo Gu and John J. Rossi. *Uncoupling of RNAi from active translation in mammalian cells.* RNA **11**(1), 38–44 (2005).

[284] Stefan Ludwig Ameres, Javier Martinez and Renée Schroeder. *Molecular Basis for Target RNA Recognition and Cleavage by Human RISC.* Cell **130**(1), 101–112 (2007).

[285] A. Nykänen, B. Haley and P. D. Zamore. *ATP Requirements and Small Interfering RNA Structure in the RNA Interference Pathway.* Cell **107**(3), 309–321 (2001).

[286] John G. Doench and Phillip A. Sharp. *Specificity of microRNA target selection in translational repression.* Genes Dev. **18**(5), 504–511 (2004).

[287] Wigard P. Kloosterman, Erno Wienholds, René F. Ketting and Ronald H. A. Plasterk. *Substrate requirements for let-7 function in the developing zebrafish embryo.* Nucleic Acids Res. **32**(21), 6284–6291 (2004).

[288] Witold Filipowicz. *RNAi: The nuts and bolts of the RISC machine.* Cell **122**(1), 17–20 (2005).

[289] Umar Jan Rashid, Dirk Paterok, Alexander Koglin, Holger Gohlke, Jacob Piehler and Julian C.-H. Chen. *Structure of Aquifex aeolicus Argonaute Highlights Conformational Flexibility of the PAZ Domain as a Potential Regulator of RNA-induced Silencing Complex Function.* J. Biol. Chem. **282**(18), 13824–13832 (2007).

[290] Yanli Wang, Stefan Juranek, Haitao Li, Gang Sheng, Thomas Tuschl and Dinshaw J. Patel. *Structure of an argonaute silencing complex with a seed-containing guide DNA and target RNA duplex.* Nature **456**(7224), 921–926 (2008).

[291] Yanli Wang, Stefan Juranek, Haitao Li, Gang Sheng, Greg S. Wardle, Thomas Tuschl and Dinshaw J. Patel. *Nucleation, propagation and cleavage of target RNAs in Ago silencing complexes.* Nature **461**(7265), 754–761 (2009).

[292] Kathy Q. Luo and Donald C. Chang. *The gene-silencing efficiency of siRNA is strongly dependent on the local structure of mRNA at the targeted region.* Biochem. Biophys. Res. Commun. **318**(1), 303–310 (2004).

[293] Kirk M. Brown, Chia-Ying Chu and Tariq M. Rana. *Target accessibility dictates the potency of human RISC.* Nat. Struct. Mol. Biol. **12**(5), 469–470 (2005).

[294] Bret S. E. Heale, Harris S. Soifer, Chauncey Bowers and John J. Rossi. *siRNA target site secondary structure predictions using local stable substructures.* Nucleic Acids Res. **33**(3), e30 (2005).

[295] Steffen Schubert, Arnold Grünweller, Volker A. Erdmann and Jens Kurreck. *Local RNA Target Structure Influences siRNA Efficacy: Systematic Analysis of Intentionally Designed Binding Regions.* J. Mol. Biol. **348**(4), 883–893 (2005).

[296] Tim A. Rand, Krzysztof Ginalski, Nick V. Grishin and Xiaodong Wang. *Biochemical identification of Argonaute 2 as the sole protein required for RNA-induced silencing complex activity.* Proc. Natl. Acad. Sci. USA **101**(40), 14385–14389 (2004).

[297] Yan Zeng, Rui Yi and Bryan R. Cullen. *MicroRNAs and small interfering RNAs can inhibit mRNA expression by similar mechanisms.* Proc. Natl. Acad. Sci. USA **100**(17), 9779–9784 (2003).

[298] Ya-Lin Chiu and Tariq M. Rana. *siRNA function in RNAi: A chemical modification analysis.* RNA **9**(9), 1034–1048 (2003).

[299] Benjamin Haley and Phillip D. Zamore. *Kinetic analysis of the RNAi enzyme complex.* Nat. Struct. Mol. Biol. **11**(7), 599–606 (2004).

[300] Soraya Yekta, I-Hung Shih and David P. Bartel. *MicroRNA-Directed Cleavage of HOXB8 mRNA.* Science **304**(5670), 594–596 (2004).

[301] Erica Davis, Florian Caiment, Xavier Tordoir, Jérôme Cavaillé, Anne Ferguson-Smith, Noelle Cockett, Michel Georges and Carole Charlier. *RNAi-Mediated Allelic trans-Interaction at the Imprinted Rtl1/Peg11 Locus.* Curr. Biol. **15**(8), 743–749 (2005).

[302] S. M. Elbashir, J. Martinez, A. Patkaniowska, W. Lendeckel and T. Tuschl. *Functional anatomy of siRNAs for mediating efficient RNAi in Drosophila melanogaster embryo lysate.* EMBO J. **20**(23), 6877–6888 (2001).

[303] Ji-Joon Song, Stephanie K. Smith, Gregory J. Hannon and Leemor Joshua-Tor. *Crystal Structure of Argonaute and Its Implications for RISC Slicer Activity.* Science **305**(5689), 1434–1437 (2004).

[304] Javier Martinez and Thomas Tuschl. *RISC is a 5' phosphomonoester-producing RNA endonuclease.* Genes Dev. **18**(9), 975–980 (2004).

[305] Dianne S. Schwarz, Yukihide Tomari and Phillip D. Zamore. *The RNA-Induced Silencing Complex is a Mg2+-Dependent Endonuclease.* Curr. Biol. **14**(9), 787–791 (2004).

[306] Marcin Nowotny, Sergei A. Gaidamakov, Robert J. Crouch and Wei Yang. *Crystal Structures of RNase H Bound to an RNA/DNA Hybrid: Substrate Specificity and Metal-Dependent Catalysis.* Cell **121**(7), 1005–1016 (2005).

[307] Tamas I. Orban and Elisa Izaurralde. *Decay of mRNAs targeted by RISC requires XRN1, the Ski complex, and the exosome.* RNA **11**(4), 459–469 (2005).

[308] Jan Rehwinkel, Isabelle Behm-Ansmant, David Gatfield and Elisa Izaurralde. *A crucial role for GW182 and the DCP1:DCP2 decapping complex in miRNA-mediated gene silencing.* RNA **11**(11), 1640–1647 (2005).

[309] Torgeir Holen, Mohammed Amarzguioui, Merete T Wiiger, Eshrat Babaie and Hans Prydz. *Positional effects of short interfering RNAs targeting the human coagulation trigger Tissue Factor.* Nucleic Acids Res. **30**(8), 1757–1766 (2002).

[310] Frank Czauderna, Melanie Fechtner, Sibylle Dames, Hüseyin Aygün, Anke Klippel, Gijsbertus J. Pronk, Klaus Giese and Jörg Kaufmann. *Structural variations and stabilising modifications of synthetic siRNAs in mammalian cells.* Nucleic Acids Res. **31**(11), 2705–2716 (2003).

[311] Aimee L. Jackson, Steven R. Bartz, Janell Schelter, Sumire V. Kobayashi, Julja Burchard, Mao Mao, Bin Li, Guy Cavet and Peter S. Linsley. *Expression profiling reveals off-target gene regulation by RNAi.* Nat. Biotechnol. **21**(6), 635–637 (2003).

[312] Xiaoyu Lin, Xiaoan Ruan, Mark G. Anderson, Jeffrey A. McDowell, Paul E. Kroeger, Stephen W. Fesik and Yu Shen. *siRNA-mediated off-target gene silencing triggered by a 7 nt complementation.* Nucleic Acids Res. **33**(14), 4527–4535 (2005).

[313] Aimee L. Jackson, Julja Burchard, Janell Schelter, B. Nelson Chau, Michele Cleary, Lee Lim and Peter S. Linsley. *Widespread siRNA off-target transcript silencing mediated by seed region sequence complementarity.* RNA **12**(7), 1179–1187 (2006).

[314] Amanda Birmingham, Emily M. Anderson, Angela Reynolds, Diane Ilsley-Tyree, Devin Leake, Yuriy Fedorov, Scott Baskerville, Elena Maksimova, Kathryn Robinson, Jon Karpilow, William S. Marshall and Anastasia Khvorova. *3' UTR seed matches, but not overall identity, are associated with RNAi off-targets.* Nat. Methods **3**(3), 199–204 (2006).

[315] David P. Bartel. *MicroRNAs: Genomics, Biogenesis, Mechanism, and Function.* Cell **116**(2), 281–297 (2004).

[316] Witold Filipowicz, Suvendra N Bhattacharyya and Nahum Sonenberg. *Mechanisms of post-transcriptional regulation by microRNAs: are the answers in sight?* Nat. Rev. Genet. **9**(2), 102–114 (2008).

[317] David P. Bartel. *MicroRNAs: Target Recognition and Regulatory Functions.* Cell **136**(2), 215–233 (2009).

[318] Zissimos Mourelatos, Josée Dostie, Sergey Paushkin, Anup Sharma, Bernard Charroux, Linda Abel, Juri Rappsilber, Matthias Mann and Gideon Dreyfuss. *miRNPs: a novel class of ribonucleoproteins containing numerous microRNAs.* Genes Dev. **16**(6), 720–728 (2002).

[319] Ramesh S. Pillai, Caroline G. Artus and Witold Filipowicz. *Tethering of human Ago proteins to mRNA mimics the miRNA-mediated repression of protein synthesis.* RNA **10**(10), 1518–1525 (2004).

[320] Isabelle Behm-Ansmant, Jan Rehwinkel, Tobias Doerks, Alexander Stark, Peer Bork and Elisa Izaurralde. *mRNA degradation by miRNAs and GW182 requires both CCR4:NOT deadenylase and DCP1:DCP2 decapping complexes.* Genes Dev. **20**(14), 1885–1898 (2006).

[321] Susanne Till, Erwan Lejeune, Rolf Thermann, Miriam Bortfeld, Michael Hothorn, Daniel Enderle, Constanze Heinrich, Matthias W. Hentze and Andreas G. Ladurner. *A conserved motif in Argonaute-interacting proteins mediates functional interactions through the Argonaute PIWI domain.* Nat. Struct. Mol. Biol. **14**(10), 897–903 (2007).

[322] Jidong Liu, Fabiola V. Rivas, James Wohlschlegel, John R. Yates, Roy Parker and Gregory J. Hannon. *A role for the P-body component GW182 in microRNA function.* Nat. Cell Biol. **7**(12), 1261–1266 (2005).

[323] Ana Eulalio, Eric Huntzinger and Elisa Izaurralde. *GW182 interaction with Argonaute is essential for miRNA-mediated translational repression and mRNA decay.* Nat. Struct. Mol. Biol. **15**(4), 346–353 (2008).

[324] Shintaro Iwasaki, Tomoko Kawamata and Yukihide Tomari. *Drosophila Argonaute1 and Argonaute2 Employ Distinct Mechanisms for Translational Repression.* Mol. Cell **34**(1), 58–67 (2009).

[325] John G. Doench, Christian P. Petersen and Phillip A. Sharp. *siRNAs can function as miRNAs.* Genes Dev. **17**(4), 438–442 (2003).

[326] E. G. Moss, R. C. Lee and V. Ambros. *The cold shock domain protein LIN-28 controls developmental timing in C. elegans and is regulated by the lin-4 RNA.* Cell **88**(5), 637–646 (1997).

[327] B. J. Reinhart, F. J. Slack, M. Basson, A. E. Pasquinelli, J. C. Bettinger, A. E. Rougvie, H. R. Horvitz and G. Ruvkun. *The 21-nucleotide let-7 RNA regulates developmental timing in Caenorhabditis elegans.* Nature **403**(6772), 901–906 (2000).

[328] A. Grishok, A. E. Pasquinelli, D. Conte, N. Li, S. Parrish, I. Ha, D. L. Baillie, A. Fire, G. Ruvkun and C. C. Mello. *Genes and Mechanisms Related to RNA Interference Regulate Expression of the Small Temporal RNAs that Control C. elegans Developmental Timing.* Cell **106**(1), 23–34 (2001).

[329] Michaela Beitzinger, Lasse Peters, Jia Yun Zhu, Elisabeth Kremmer and Gunter Meister. *Identification of Human microRNA Targets From Isolated Argonaute Protein Complexes.* RNA Biol. **4**(2), 76–84 (2007).

[330] George Easow, Aurelio A. Teleman and Stephen M. Cohen. *Isolation of microRNA targets by miRNP immunopurification.* RNA **13**(8), 1198–1204 (2007).

[331] Fedor V. Karginov, Cecilia Conaco, Zhenyu Xuan, Bryan H Schmidt, Joel S. Parker, Gail Mandel and Gregory J. Hannon. *A biochemical approach to identifying microRNA targets.* Proc. Natl. Acad. Sci. USA **104**(49), 19291–19296 (2007).

[332] Ana Eulalio, Isabelle Behm-Ansmant, Daniel Schweizer and Elisa Izaurralde. *P-Body Formation Is a Consequence, Not the Cause, of RNA-Mediated Gene Silencing.* Mol. Cell. Biol. **27**(11), 3970–3981 (2007).

[333] Daehyun Baek, Judit Villén, Chanseok Shin, Fernando D Camargo, Steven P. Gygi and David P. Bartel. *The impact of microRNAs on protein output.* Nature **455**(7209), 64–71 (2008).

[334] Matthias Selbach, Björn Schwanhäusser, Nadine Thierfelder, Zhuo Fang, Raya Khanin and Nikolaus Rajewsky. *Widespread changes in protein synthesis induced by microRNAs.* Nature **455**(7209), 58–63 (2008).

[335] Ana Eulalio, Eric Huntzinger, Tadashi Nishihara, Jan Rehwinkel, Maria Fauser and Elisa Izaurralde. *Deadenylation is a widespread effect of miRNA regulation.* RNA **15**(1), 21–32 (2009).

[336] Ligang Wu, Jihua Fan and Joel G. Belasco. *MicroRNAs direct rapid deadenylation of mRNA.* Proc. Natl. Acad. Sci. USA **103**(11), 4034–4039 (2006).

[337] Ana Eulalio, Jan Rehwinkel, Mona Stricker, Eric Huntzinger, Schu-Fee Yang, Tobias Doerks, Silke Dorner, Peer Bork, Michael Boutros and Elisa Izaurralde. *Target-specific requirements for enhancers of decapping in miRNA-mediated gene silencing.* Genes Dev. **21**(20), 2558–2570 (2007).

[338] Yi Wen Kong, Ian G. Cannell, Cornelia H. de Moor, Kirsti Hill, Paul G. Garside, Tiffany L. Hamilton, Hedda A. Meijer, Helen C. Dobbyn, Mark Stoneley, Keith A. Spriggs, Anne E. Willis and Martin Bushell. *The mechanism of micro-RNA-mediated translation repression is determined by the promoter of the target gene.* Proc. Natl. Acad. Sci. USA **105**(26), 8866–8871 (2008).

[339] P. H. Olsen and V. Ambros. *The lin-4 Regulatory RNA Controls Developmental Timing in Caenorhabditis elegans by Blocking LIN-14 Protein Synthesis after the Initiation of Translation.* Dev. Biol. **216**(2), 671–680 (1999).

[340] Kathy Seggerson, Lingjuan Tang and Eric G. Moss. *Two Genetic Circuits Repress the Caenorhabditis elegans Heterochronic Gene lin-28 after Translation Initiation.* Dev. Biol. **243**(2), 215–225 (2002).

[341] Patricia A. Maroney, Yang Yu, Jesse Fisher and Timothy W. Nilsen. *Evidence that microRNAs are associated with translating messenger RNAs in human cells.* Nat. Struct. Mol. Biol. **13**(12), 1102–1107 (2006).

[342] Stephanie Nottrott, Martin J. Simard and Joel D. Richter. *Human let-7a miRNA blocks protein production on actively translating polyribosomes.* Nat. Struct. Mol. Biol. **13**(12), 1108–1114 (2006).

[343] Xavier C. Ding and Helge Grosshans. *Repression of C. elegans microRNA targets at the initiation level of translation requires GW182 proteins.* EMBO J. **28**(3), 213–222 (2009).

[344] Marianthi Kiriakidou, Grace S. Tan, Styliani Lamprinaki, Mariangels De Planell-Saguer, Peter T. Nelson and Zissimos Mourelatos. *An mRNA m7G Cap Binding-like Motif within Human Ago2 Represses Translation.* Cell **129**(6), 1141–1151 (2007).

[345] Géraldine Mathonnet, Marc R.Fabian, Yuri V. Svitkin, Armen Parsyan, Laurent Huck, Takayuki Murata, Stefano Biffo, William C. Merrick, Edward Darzynkiewicz, Ramesh S. Pillai, Witold Filipowicz, Thomas F. Duchaine and Nahum Sonenberg. *MicroRNA Inhibition of Translation Initiation in Vitro by Targeting the Cap-Binding Complex eIF4F.* Science **317**(5845), 1764–1767 (2007).

[346] Rolf Thermann and Matthias W. Hentze. *Drosophila miR2 induces pseudo-polysomes and inhibits translation initiation.* Nature **447**(7146), 875–878 (2007).

[347] Motoaki Wakiyama, Koji Takimoto, Osamu Ohara and Shigeyuki Yokoyama. *Let-7 microRNA-mediated mRNA deadenylation and translational repression in a mammalian cell-free system.* Genes Dev. **21**(15), 1857–1862 (2007).

[348] Ramesh S. Pillai, Suvendra N. Bhattacharyya, Caroline G. Artus, Tabea Zoller, Nicolas Cougot, Eugenia Basyuk, Edouard Bertrand and Witold Filipowicz. *Inhibition of Translational Initiation by Let-7 MicroRNA in Human Cells.* Science **309**(5740), 1573–1576 (2005).

[349] Suvendra N. Bhattacharyya, Regula Habermacher, Ursula Martine, Ellen I. Closs and Witold Filipowicz. *Relief of microRNA-Mediated Translational Repression in Human Cells Subjected to Stress.* Cell **125**(6), 1111–1124 (2006).

[350] Ujwal Sheth and Roy Parker. *Decapping and Decay of Messenger RNA Occur in Cytoplasmic Processing Bodies.* Science **300**(5620), 805–808 (2003).

[351] Roy Parker and Haiwei Song. *The enzymes and control of eukaryotic mRNA turnover.* Nat. Struct. Mol. Biol. **11**(2), 121–127 (2004).

[352] Nicolas Cougot, Sylvie Babajko and Bertrand Séraphin. *Cytoplasmic foci are sites of mRNA decay in human cells.* J. Cell Biol. **165**(1), 31–40 (2004).

[353] Jidong Liu, Marco Antonio Valencia-Sanchez, Gregory J. Hannon and Roy Parker. *MicroRNA-dependent localization of targeted mRNAs to mammalian P-bodies.* Nat. Cell Biol. **7**(7), 719–723 (2005).

[354] Asuka Azuma-Mukai, Hideo Oguri, Toutai Mituyama, Zhi Rong Qian, Kiyoshi Asai, Haruhiko Siomi and Mikiko C. Siomi. *Characterization of endogenous human Argonautes and their miRNA partners in RNA silencing.* Proc. Natl. Acad. Sci. USA **105**(23), 7964–7969 (2008).

[355] Andrew Jakymiw, Shangli Lian, Theophany Eystathioy, Songqing Li, Minoru Satoh, John C. Hamel, Marvin J. Fritzler and Edward K. L. Chan. *Disruption of GW bodies impairs mammalian RNA interference.* Nat. Cell Biol. **7**(12), 1267–1274 (2005).

[356] Shveta Bagga, John Bracht, Shaun Hunter, Katlin Massirer, Janette Holtz, Rachel Eachus and Amy E. Pasquinelli. *Regulation by let-7 and lin-4 miRNAs Results in Target mRNA Degradation.* Cell **122**(4), 553–563 (2005).

[357] Muriel Brengues, Daniela Teixeira and Roy Parker. *Movement of Eukaryotic mRNAs Between Polysomes and Cytoplasmic Processing Bodies.* Science **310**(5747), 486–489 (2005).

[358] Marjori A. Matzke and James A. Birchler. *RNAi-mediated pathways in the nucleus.* Nat. Rev. Genet. **6**(1), 24–35 (2005).

[359] Danesh Moazed. *Small RNAs in transcriptional gene silencing and genome defence.* Nature **457**(7228), 413–420 (2009).

[360] Jiang Han, Daniel Kim and Kevin V. Morris. *Promoter-associated RNA is required for RNA-directed transcriptional gene silencing in human cells.* Proc. Natl. Acad. Sci. USA **104**(30), 12422–12427 (2007).

[361] Susana Gonzalez, David G. Pisano and Manuel Serrano. *Mechanistic principles of chromatin remodeling guided by siRNAs and miRNAs.* Cell Cycle **7**(16), 2601–2608 (2008).

[362] Daniel H. Kim, Pål Saetrom, Ola Snøve and John J. Rossi. *MicroRNA-directed transcriptional gene silencing in mammalian cells.* Proc. Natl. Acad. Sci. USA **105**(42), 16230–16235 (2008).

[363] Bethany A. Janowski, Kenneth E. Huffman, Jacob C. Schwartz, Rosalyn Ram, Robert Nordsell, David S. Shames, John D. Minna and David R. Corey. *Involvement of AGO1 and AGO2 in mammalian transcriptional silencing.* Nat. Struct. Mol. Biol. **13**(9), 787–792 (2006).

[364] Daniel H. Kim, Louisa M. Villeneuve, Kevin V. Morris and John J. Rossi. *Argonaute-1 directs siRNA-mediated transcriptional gene silencing in human cells.* Nat. Struct. Mol. Biol. **13**(9), 793–797 (2006).

[365] Marc S. Weinberg, Louisa M. Villeneuve, Ali Ehsani, Mohammed Amarzguioui, Lars Aagaard, Zhao-Xia Chen, Arthur D. Riggs, John J. Rossi and Kevin V. Morris. *The antisense strand of small interfering RNAs directs histone methylation and transcriptional gene silencing in human cells.* RNA **12**(2), 256–262 (2006).

[366] Kevin V. Morris, Simon W.-L. Chan, Steven E. Jacobsen and David J. Looney. *Small interfering RNA-Induced Transcriptional Gene Silencing in Human Cells.* Science **305**(5688), 1289–1292 (2004).

[367] T. Ohrt and P. Schwille. *siRNA Modifications and Sub-Cellular Localization: A Question of Intracellular Transport?* Curr. Pharm. Des. **14**(34), 3674–3685 (2008).

[368] Thomas Ohrt. *Elucidating the intracellular mechanisms of RNA interference by single molecule fluorescence microscopy and spectroscopy.* PhD thesis, TU Dresden, 2007.

[369] Mark A. Behlke. *Chemical Modification of siRNAs for In Vivo Use.* Oligonucleotides **18**(4), 305–319 (2008).

[370] Jonathan K. Watts, Glen F. Deleavey and Masad J. Damha. *Chemically modified siRNA: tools and applications.* Drug. Discov. Today **13**(19-20), 842–855 (2008).

[371] Kumiko Ui-Tei, Yuki Naito, Shuhei Zenno, Kenji Nishi, Kenji Yamato, Fumitaka Takahashi, Aya Juni and Kaoru Saigo. *Functional dissection of siRNA sequence by systematic DNA substitution: modified siRNA with a DNA seed arm is a powerful tool for mammalian gene silencing with significantly reduced off-target effect.* Nucleic Acids Res. **36**(7), 2136–2151 (2008).

[372] Michael D. Horwich, Chengjian Li, Christian Matranga, Vasily Vagin, Gwen Farley, Peng Wang and Phillip D. Zamore. *The Drosophila RNA Methyltransferase, DmHen1, Modifies Germline piRNAs and Single-Stranded siRNAs in RISC.* Curr. Biol. **17**(14), 1265–1272 (2007).

[373] Yohei Kirino and Zissimos Mourelatos. *The mouse homolog of HEN1 is a potential methylase for Piwi-interacting RNAs.* RNA **13**(9), 1397–1401 (2007).

[374] Tomoya Ohara, Yuriko Sakaguchi, Takeo Suzuki, Hiroki Ueda, Kenjyo Miyauchi and Tsutomu Suzuki. *The 3' termini of mouse Piwi-interacting RNAs are 2'-O-methylated.* Nat. Struct. Mol. Biol. **14**(4), 349–350 (2007).

[375] Kuniaki Saito, Yuriko Sakaguchi, Takeo Suzuki, Tsutomu Suzuki, Haruhiko Siomi and Mikiko C. Siomi. *Pimet, the Drosophila homolog of HEN1, mediates 2'-O-methylation of Piwi- interacting RNAs at their 3' ends.* Genes Dev. **21**(13), 1603–1608 (2007).

[376] Mohammed Amarzguioui, Torgeir Holen, Eshrat Babaie and Hans Prydz. *Tolerance for mutations and chemical modifications in a siRNA.* Nucleic Acids Res. **31**(2), 589–595 (2003).

[377] Thazha P. Prakash, Charles R. Allerson, Prasad Dande, Timothy A. Vickers, Namir Sioufi, Russell Jarres, Brenda F. Baker, Eric E. Swayze, Richard H. Griffey and Balkrishen Bhat. *Positional Effect of Chemical Modifications on Short Interference RNA Activity in Mammalian Cells.* J. Med. Chem. **48**(13), 4247–4253 (2005).

[378] Sorim Choung, Young Joo Kim, Seonhoe Kim, Han-Oh Park and Young-Chul Choi. *Chemical modification of siRNAs to improve serum stability without loss of efficacy.* Biochem. Biophys. Res. Commun. **342**(3), 919–927 (2006).

[379] Bryan A. Kraynack and Brenda F. Baker. *Small interfering RNAs containing full 2'-O-methylribonucleotide-modified sense strands display Argonaute2/eIF2C2-dependent activity.* RNA **12**(1), 163–176 (2006).

[380] Charles R. Allerson, Namir Sioufi, Russell Jarres, Thazha P. Prakash, Nishant Naik, Andres Berdeja, Lisa Wanders, Richard H. Griffey, Eric E. Swayze and Balkrishen Bhat. *Fully 2'-modified oligonucleotide duplexes with improved in vitro potency and stability compared to unmodified small interfering RNA.* J. Med. Chem. **48**(4), 901–904 (2005).

[381] György Hutvágner, Martin J. Simard, Craig C. Mello and Phillip D. Zamore. *Sequence-Specific Inhibition of Small RNA Function.* PLoS Biol. **2**(4), e98 (2004).

[382] Gunter Meister, Markus Landthaler, Yair Dorsett and Thomas Tuschl. *Sequence-specific inhibition of microRNA- and siRNA-induced RNA silencing.* RNA **10**(3), 544–550 (2004).

[383] Aimee L. Jackson, Julja Burchard, Devin Leake, Angela Reynolds, Janell Schelter, Jie Guo, Jason M. Johnson, Lee Lim, Jon Karpilow, Kim Nichols, William Marshall, Anastasia Khvorova and Peter S. Linsley. *Position-specific chemical modification of siRNAs reduces öff-targetttranscript silencing.* RNA **12**(7), 1197–1205 (2006).

[384] Po Yu Chen, Lasse Weinmann, Dimos Gaidatzis, Yi Pei, Mihaela Zavolan, Thomas Tuschl and Gunter Meister. *Strand-specific 5'-O-methylation of siRNA duplexes controls guide strand selection and targeting specificity.* RNA **14**(2), 263–274 (2008).

[385] Dwaine A. Braasch, Susan Jensen, Yinghui Liu, Kiran Kaur, Khalil Arar, Michael A. White and David R. Corey. *RNA Interference in Mammalian Cells by Chemically-Modified RNA.* Biochemistry **42**(26), 7967–7975 (2003).

[386] Jens Harborth, Sayda M. Elbashir, Kim Vandenburgh, Heiko Manninga, Stephen A. Scaringe, Klaus Weber and Thomas Tuschl. *Sequence, Chemical, and Structural Variation of Small Interfering RNAs and Short Hairpin RNAs and the Effect on Mammalian Gene Silencing.* Antisense Nucleic Acid Drug Dev. **13**(2), 83–105 (2003).

[387] Juliana M. Layzer, Anton P. McCaffrey, Alice K. Tanner, Zan Huang, Mark A. Kay and Bruce A. Sullenger. *In vivo activity of nuclease-resistant siRNAs.* RNA **10**(5), 766–771 (2004).

[388] Christina Lorenz, Philipp Hadwiger, Matthias John, Hans-Peter Vornlocher and Carlo Unverzagt. *Steroid and lipid conjugates of siRNAs to enhance cellular uptake and gene silencing in liver cells.* Bioorg. Med. Chem. Lett. **14**(19), 4975–4977 (2004).

[389] Thomas Ohrt, Dennis Merkle, Karin Birkenfeld, Christophe J. Echeverri and Petra Schwille. *In situ fluorescence analysis demonstrates active siRNA exclusion from the nucleus by Exportin 5.* Nucleic Acids Res. **34**(5), 1369–1380 (2006).

[390] Daniel H. Kim and John J. Rossi. *Strategies for silencing human disease using RNA interference.* Nat. Rev. Genet. **8**(3), 173–184 (2007).

[391] Antonin de Fougerolles, Hans-Peter Vornlocher, John Maraganore and Judy Lieberman. *Interfering with disease: a progress report on siRNA-based therapeutics.* Nat. Rev. Drug. Discov. **6**(6), 443–453 (2007).

[392] Daniela Castanotto and John J. Rossi. *The promises and pitfalls of RNA-interference-based therapeutics.* Nature **457**(7228), 426–433 (2009).

[393] Thomas Ohrt, Jörg Mütze, Wolfgang Staroske, Lasse Weinmann, Julia Höck, Karin Crell, Gunter Meister and Petra Schwille. *Fluorescence correlation spectroscopy and fluorescence cross-correlation spectroscopy reveal the cytoplasmic origination of loaded nuclear RISC in vivo in human cells.* Nucleic Acids Res. **36**(20), 6439–6449 (2008).

[394] A. M. Krieg and C. A. Stein. *Phosphorothioate Oligodeoxynucleotides: Antisense or Anti-Protein?* Antisense Res. Dev. **5**(4), 241 (1995).

Acknowledgements

The work described in this thesis was performed in the research group of Prof. Dr. Petra Schwille at the Institute of Biophysics of the Dresden University of Technology (TUD).

I am grateful to all people who contributed to this work presented here. Specifically, I would like to thank:

Prof. Dr. Petra Schwille for the great opportunity to work in her lab. While encouraging me to work independently, she was always open to discuss any questions and problems. I am very grateful for her support, the great working environment she created in her lab and the opportunity to present my results on conferences.

Prof Dr. Jörg Enderlein for kindly agreeing to review this thesis.

Dr. Thomas Ohrt vor all his experience in RNA interference, for is help with all the biochemistry work in this project and for his patient proofreading of the RNAi chapters of this thesis.

Jörg Mütze for the good collaboration in the RNAi project and the proofreading of my thesis.

Dr. Maika Felten and her supervisor Dr. Claus Duschl for their collaboration in the micropump project.

Dr. Zdenek Petrasek for many discussions, for all the helpful answers to my FCS questions and for proofreading of this thesis.

Dr. Thomas Weidemann and Dr. Remigiusz Worch for all your patience with my biological questions and the helpful discussions.

Dr. Jonas Ries for his help with Matlab.

Prof. Dr. Torsten Fritz for proofreading the FCS chapter of this thesis.

Karin Crell for culturing the cells and Claudia Schwäger for handling all the bureaucracy.

All the member of the Schwille group, especially my room mates Jörg Mütze, Jakob Schweizer, and Markus Burkhardt for many fruitful discussions and the familiar atmosphere.

My family for all the appreciation and support, while I was working on this thesis.

Erklärung (Declaration)

Hiermit versichere ich, dass ich die vorliegende Arbeit ohne unzulässige Hilfe Dritter und ohne Benutzung anderer als der angegebenen Hilfsmittel angefertigt habe; die aus fremden Quellen direkt oder indirekt übernommenen Gedanken sind als solche kenntlich gemacht. Die Arbeit wurde bisher weder im Inland noch im Ausland in gleicher oder ähnlicher Form einer anderen Prüfungsbehörde vorgelegt.

Diese Arbeit wurde von November 2003 bis Juni 2010 unter Betreuung von Prof. Dr. Schwille an der Technischen Universität Dresden angefertigt.

Wolfgang Staroske Dresden, 30. Juni 2010

I herewith declare that I have produced this thesis without the prohibited assistance of third parties and without making use of aids other than those specified; notions taken over directly or indirectly from other sources have been identified as such. This thesis has not been previously presented in identical or similar form to any other German or foreign examination board.

The thesis work was conducted between November 2003 and June 2010 under the supervision of Prof. Dr. Petra Schwille at the Dresden University of Technology.